March 2015

ON THE ORDERING, MICROSTRUCTURE AND HOLE TRANSPORT CORRELATIONS IN SEMI-CRYSTALLINE POLY(3-HEXYLTHIOPHENE)

Xiaobo Shen
University of Massachusetts - Amherst

Recommended Citation

ON THE ORDERING, MICROSTRUCTURE AND HOLE TRANSPORT CORRELATIONS IN SEMI-CRYSTALLINE POLY(3-HEXYLTHIOPHENE)

A Dissertation Presented

by

XIAOBO SHEN

Submitted to the Graduate School of the
University of Massachusetts Amherst in partial fulfillment
of the requirements for the degree of

DOCTOR OF PHILOSOPHY

February 2015

Polymer Science and Engineering

ON THE ORDERING, MICROSTRUCTURE AND HOLE TRANSPORT CORRELATIONS IN SEMI-CRYSTALLINE POLY(3-HEXYLTHIOPHENE)

A Dissertation Presented

by

XIAOBO SHEN

Approved as to style and content by:

_____
Thomas P. Russell, Chair

_____
Ryan C. Hayward, Member

_____
Dhandapani Venkataraman, Member

_____
David A. Hoagland, Department Head
Polymer Science and Engineering

To my parents, Chengbei and Grace

v

projects. I greatly appreciate the time they have spent on the time-of-flight and NMR measurements, the frequent discussions, and the manuscript preparations. I thank my class of 2009 fellows: Maria, Irem, Polina, Yujie, Jinhye, Omkar, Andrew, Sahas, Varun, Katie and Cathy, my other PSE friends: Dayong, Jun, Yongping, Li, Peiwen, Minchao, Jeff and Xiangji for their great help and support in my research as well as in my personal life. I am also grateful to the staff members at UMass: Sandi, Laurie, Lisa, Maria, Jessica, Lou, Alex, Dale and Sekar, who have provided assistances for my work. Dr. David Waldman is acknowledged for his kind help in my job hunting. I am thankful to the US Department of Energy and the Energy Frontier Research Center at UMass for proving the funding to support my research. I feel blessed to have met and known many other friends outside of PSE. Special thanks go to Sheng, Jing, Jeff, Yue, Ying, Professor Ken Nakajima, Xiaobin, Hao and Lixue. I sincerely thank Brian Cromer and the medical team at Cooley Dickinson Hospital for their help in saving my life from a cardiac arrest incident in 2011.

I dedicate this thesis to my parents, Xiaoping Shen and Meibao Shao, who have been placing my education and well-being above anything else in their lives. I am especially grateful to my wife, Chengbei Li, for her love, encouragement and support during the past 4 years. Special acknowledgement goes to my little daughter, Grace Shen, for bringing so much joy into my life.

ABSTRACT

ON THE ORDERING, MICROSTRUCTURE AND HOLE TRANSPORT
CORRELATIONS IN SEMI-CRYSTALLINE POLY(3-HEXYLTHIOPHENE)

FEBRUARY 2015

XIAOBO SHEN, B.S., ZHEJIANG UNIVERSITY

M.S., UNIVERSITY OF MASSACHUSETTS AMHERST

Ph.D., UNIVERSITY OF MASSACHUSETTS AMHERST

Directed by: Professor Thomas P. Russell

This dissertation focuses on describing the research work done on poly(3-hexylthiophene) (P3HT), which represents one of the most important p-type semi-conducting polymers widely used in the field of organic optoelectronics. P3HT is also identified as a typical semi-crystalline material comprising different phases that would yield distinct impacts on its properties when integrated as an active component in optoelectronic devices. In particular, as the material finds great use as a hole-conductor, the objective of the dissertation is to develop a fundamental and quantitative understanding of the relationship between the semi-crystalline morphology and hole transport properties in P3HT.

The first section provides a general introduction of the material P3HT and its role as the hole conducting material in various devices including organic photovoltaic solar cells, organic field effect transistors (OFET) and time-of-flight (TOF) devices. Characteristics of the OFET and TOF measurements are discussed. In parallel, structural characterizations of P3HT involving various methods are also described, followed by the introduction of current research progress in the field, and the motivations of the research presented in this dissertation.

Three projects are detailed following the introduction section. In the first project, a correlation between the hole transport and corresponding structural properties of the bulk regioregular poly(3-hexylthiophene) (rr-P3HT) is studied as a function of temperature by the time-of-flight (TOF) and wide angle X-ray diffraction (WAXD) techniques. Combining the measured transport characteristics and structural evolutions, two temperature regions with distinct transport mechanisms are identified. At $T<120^{o}C$, the transport-related structural changes are negligible, and the hole transport is limited by the amorphous phase and can be thermally activated. At $T>120^{o}C$, a microscopic thermal expansion along the π-π stacking direction within the nanocrystals and a macroscopic deterioration in the ordering both contribute to the decrease in the hole mobility at high temperatures.

As demonstrated in the first project, the semi-crystalline morphology at different length scales plays a crucial role in dictating the hole transport properties in P3HT. The second project is aimed to gain a quantitative understanding of the ordered structures of P3HT at different length scales. Specifically, by utilizing a combination of wide angle X-ray diffraction (WAXD), density and ^{13}C solid-state nuclear magnetic resonance (NMR) measurements, the absolute degrees of crystallinity in different P3HTs are determined and compared. The results suggest that, in addition to the two-phase picture pervading in the literatures, a 10wt% local short-range ordering in the amorphous phase should be included, which may greatly influence the resulting macroscopic hole transport characteristics in P3HT-based optoelectronic devices.

As an extension of the first and second projects, the third project presents a detailed investigation of the effect of ordering and microstructures on the hole transport

properties involving P3HT with different molecular characteristics. Interestingly, two important features are universally resolved in different materials: (i) a significant increase of the hole mobility measured by TOF at low temperatures in physically aged samples; (ii) an abrupt jump in the hole mobility at high temperatures. Taking advantage of the sensitivity of ^{13}C solid-state NMR to local structures, the low temperature aging effects and high temperature mobility jump are attributed to the growth of the local ordered phase in the non-crystalline region during physical aging and an improvement of the π-π stacking within the crystalline phase, respectively.

Based on the research results summarized in the three projects, the last chapter provides insights on the possible routes to further the understanding of structure-property relationships not only in the P3HT but also in other classes of semi-conducting polymers of similar semi-crystalline nature. The new understanding and strategies developed on the model P3HT materials in this dissertation are expected to shed light on improving the future design and processing of new types of high-performance semi-conducting polymers.

TABLE OF CONTENTS

LIST OF TABLES

LIST OF FIGURES

xiv

xvi

CHAPTER 1

INTRODUCTION TO THE ORDERING, MICROSTRUCTURE AND HOLE

TRANSPORT IN SEMI-CRYSTALLINE P3HT

1.1 Introduction to Organic Photovoltaics and Regioregular P3HT

In the past two decades, tremendous efforts have been invested in nearly every possible aspect of the development of organic photovoltaics (OPVs) ranging from advanced molecular design and synthesis, manipulation of the active layer morphology to device engineering.[1–6] Consequently, encouraging results have led to a recent power conversion efficiency (PCE) surpassing 10% barrier,[7] pushing the system closer to the boundary of commercialization. Yet, further improvements would rely on a more thorough examination and understanding of the aforementioned factors, for instance, active layer morphology. It is well known that in typical bulk heterojunction (BHJ) OPVs as shown in Figure 1.1(a),[8] where a thin film (e.g. 100~200nm in thickness) consisting of polymeric electron donor (e.g. rr-P3HT) and small molecule electron acceptor (e.g. [6,6]-phenyl-C61-butyric-acid-methyl-ester (PCBM)) is solution processed, the morphology is of critical importance to the charge separation, transport, collection processes and therefore, the ultimate PCE.[1–3] The exciton or the bound electron-hole pair has a limited diffusion length of ~10nm, however, the dissociation of the bound-pair only occurs at the donor-acceptor interface, where an energy level offset effectively pulls electron and hole apart. Once dissociated, the positive and negative charge carriers need to be transported to the respective electrodes through the donor and acceptor domains and subsequently, collected by the electrodes to form a closed circuit. As a result, a desirable morphology would require a phase separation with sufficient interfacial area, a length scale that is

commensurate with the exciton diffusion length, and bicontinuous transporting pathways for electrons and holes to reach respective electrodes. The degree of phase separation, the miscibility of the two components and the distribution of the components within the active layer profoundly influence the charge separation and transport; while, microscopically, the crystal structure and orientation within the crystalline domain, the degree of crystallinity, etc. play a crucial role in determining charge transport. It is worth noting that all the above morphological parameters are, in general, closely related to the processing conditions, such as the choice of casting solvent,[9] annealing conditions[10] and the use of additives.[11]

Among numerous polymeric semiconductors, semi-crystalline rr-P3HT has stood out as a prototypical p-type material owing to its ease of solution processing, good stability, well-studied structural properties and good performance in organic field-effect transistors (OFET) and OPV devices, therefore, providing an excellent model for the study of charge transport, in particular, hole transport. The chemical structure of P3HT is shown in Figure 1.1(b). Like all semi-crystalline polymers, rr-P3HT consists of an ordered crystalline phase, with stacks of crystalline lamellae, and a disordered amorphous phase, with non-crystallizable chains.[12] On one hand, the degree of crystallinity in rr-P3HT - a critical parameter that quantifies the relative amount of crystalline and amorphous phases in the material - complicates the characteristics of the pathways through which the holes travel within the active layer, since the crystalline phase serves as transporting highways and the amorphous phase as charge traps.[13] On the other hand, within rr-P3HT crystalline phase, the different directions, namely, alkyl chain stacking direction a, π-π stacking direction b and backbone direction c, are found to favor hole

transport differently, thus imparting another degree of anisotropy/complexity in the charge transport processes.[14]
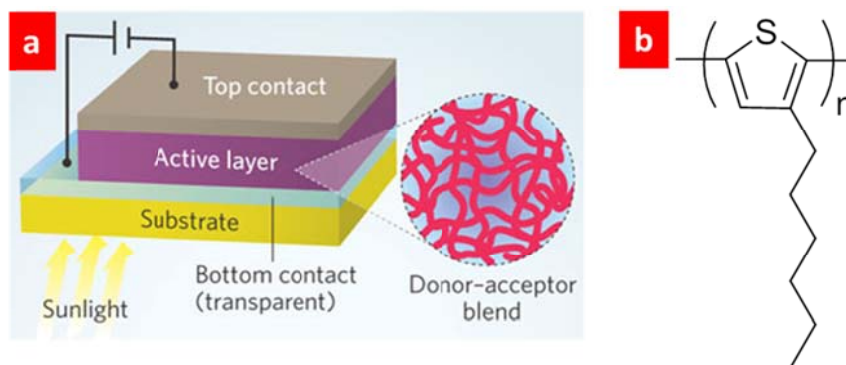
Figure 1.1: (a) Typical device configuration of a bulk-heterojunction organic photovoltaic cell;[8] (b) Chemical structure of P3HT.

1.2 Probing the Hole Transport and Morphology in rr-P3HT

The hole-transporting properties in rr-P3HT is widely characterized by several distinct and complementary techniques including organic field effect transistor (OFET),[8,15–18] time-of-flight (TOF) technique[13,19,20] and pulse-radiolysis time-resolved microwave conductivity (PR-TRMC).[21] The PR-TRMC, as demonstrated by Neher et al.,[21] is particularly useful for probing the mobility on a local scale, that is, the charge transport within single crystalline grains of the materials. In other words, the mobility probed by PR-TRMC, in comparison to TOF and OFET, is less affected by the presence of grain boundaries or charge carrier trapping on longer time scales. While both TOF and OFET measure the charge carrier mobility on a macroscopic level with the consideration of intra- and inter-grain, they differ considerably in terms of measurement configuration and sampling information as shown in Figure 1.2. In OFET measurement, the charge carriers, concentrating in the semiconductor/insulator interface as a result of the applied gate voltage, flow in the substrate plane under the bias between the source and drain

electrodes. Interestingly, it was reported that only the first two polymer molecular layers at the semiconductor/insulator interface dominate the charge transport, underscoring the significance of interfacial interaction and polymer chain orientation at the interface.[22] In stark contrast, in TOF measurement, a rather thick film (on the order of μm) of semiconducting polymer is sandwiched in between two electrodes and the charge carriers, holes in this case, are generated by a laser excitation and transported from top Al electrode to bottom ITO electrode by an external electric field. Consequently, the photocurrent response is recorded from which a characteristic transit time, τ_{tr}, is determined and therefore, the charge carrier mobility can be calculated by Equation 1-1, where L and V are film thickness and applied voltage, respectively. Noticeably, the holes travel through the thick polymer film in the transverse direction, indicating that the resulting mobility carries information about the "bulk" morphology of the polymer film. Therefore, OFET mobility is particularly sensitive to the polymer morphology at the buried interface, highlighting the importance of interfacial interactions;[23] whereas the TOF technique probes charge carrier transport in a bulk sense and is useful to elucidate the intrinsic charge transport characteristics in semi-crystalline rr-P3HT.[13,24]

One of the most commonly used tools to characterize the microstructures of semi-crystalline polymers, in the form of either bulk or thin film, is wide angle X-ray diffraction (WAXD) which can be done in either transmission or grazing incidence geometry, respectively.[5,25] Complementary to real-space techniques such as transmission electron microscopy (TEM), scanning force microscopy (SFM), etc., WAXD, as a reciprocal space technique, yields important information concerning the crystalline phase such as the crystal size and d-spacing, the degree of crystallinity as well as the crystal

orientation. Shown in Figure 1.3 is a typical geometry of grazing incidence X-ray diffraction (GIXD) measurement on a thin film rr-P3HT sample and the 2-D diffraction pattern along with the illustrative crystal orientation.[25] It is well known that GIXD provides excellent statistics for thin film samples with thickness in nanometer scale, thus serving as a potent tool for characterizing the thin films used in OFET measurement.[23] The WAXD in the transmission geometry, on the other hand, directly tracks the structural changes in a bulk polymer sample, allowing a good representation of the change in the TOF sample due to its "bulk" nature as described above.[13]
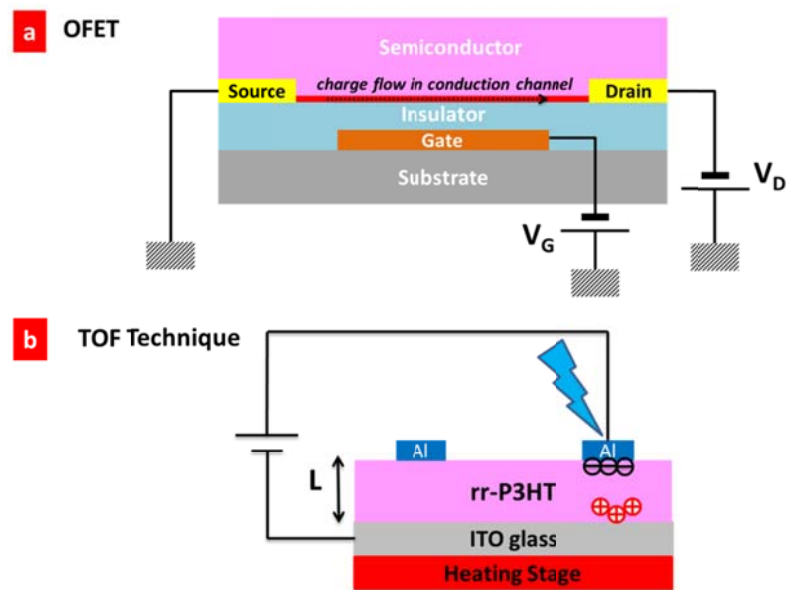
Figure 1.2: Configuration comparison between (a) organic field effect transistor and (b) Time-of-Flight technique.

$$\mu = L^2/(\tau_{tr} \times V) \hspace{3cm} \text{Eq. 1-1}$$
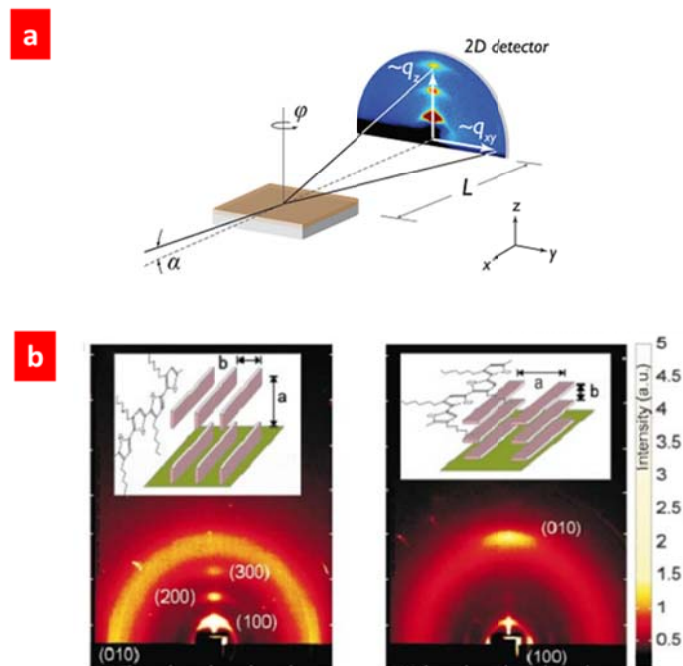
Figure 1.3: (a) Setup schematics of grazing incidence X-ray scattering with a 2-D image plate;[25] (b) GIXD patterns showing preferential edge-on (left) and face-on (right) orientations of rr-P3HT crystal lamellae with respect to the substrate. The insets show the schematics of the corresponding orientations of crystal planes.[15]

1.3 Measuring the Degree of Crystallinity in rr-P3HT

From the morphological perspective, one of the most important structural factors for P3HT is the degree of crystallinity, which is shown to have broad and great influence on the absorption, extent of miscibility or phase separation with n-type [6,6]-phenyl-C61-butyric-acid-methyl-ester (PCBM) in OPV active layer, and charge transport properties, thus the ultimate device performance. Despite the material has been intensively researched in the past two decades or so, a general agreement on the degree of crystallinity of P3HT has yet to be reached, due in one part to the unexpectedly observed disordering inside the crystals with highly anisotropic packing architecture,[26,27] and in another part to the difficulty in appropriately treating and comparing the data obtained

from various physical methods involving inherently different limitations and assumptions.

Conventionally, the degree of crystallinity in a semi-crystalline polymer has been experimentally determined by several physical methods including wide angle X-ray diffraction (WAXD), density measurement, differential scanning calorimetry (DSC), nuclear magnetic resonance (NMR), and infrared spectroscopy. It is noteworthy that, due to the unique nature and assumptions involved, each approach has distinct advantages and disadvantages which, in turn, normally lead to disparate values of the degree of crystallinity for the same sample. For thin film samples which are directly relevant to the optoelectronic devices, the multiple uncertainties originating from the presence of surfaces and interfaces inevitably add complexity to the quantification, resulting in, rather than absolute numbers, mostly indirect comparisons as measured by grazing-incidence X-ray diffraction (GIXD) and optical absorption techniques.[21,25] As far as GIXD is concerned, it is suggested by Toney et al. that a pole figure must be obtained for an accurate comparison of the relative degree of crystallinity, where the distribution of crystallites having every possible orientation with respect to the underlying substrate normal is well accounted for.[25] On the other hand, the optical absorption coefficient of rr-P3HT in the low photon energy region, which features the π-π^* transition, is shown to be proportional to the area under the X-ray diffraction peak, hence, the degree of crystallinity.[21,28,29] It is therefore proposed that the degree of crystallinity can be conveniently compared in terms of the optical absorption. However, it can be deduced that a quantitative determination of the degree of crystallinity in samples involving thin films is hindered by multiple complexities.

7

As for bulk samples, in most cases, the aforementioned physical measurements are all suitable and the analytical methods are well documented.[30] In a differential scanning calorimetry (DSC) measurement, for instance, the mass fraction degree of crystallinity for a semi-crystalline polymer is simply given by Equation 1-2, where ΔH_m and ΔH_m^{∞} are the heat of fusion for the sample and a perfectly crystallized sample with 100% crystallinity, respectively. In actual practice, since it is not trivial to prepare a polymer sample with a crystallinity of 100% due to the ubiquitous chain packing defects during crystallization, the determination of ΔH_m^{∞} requires elaborative extrapolation with oligomeric samples of known crystallinity.

$$x_c = \frac{\Delta H_m}{\Delta H_m^{\infty}}$$
Eq. 1-2

Owing to the fact that ordered crystals have a higher density than the disorganized amorphous region, a density-based method is readily developed which yields both the volume and mass fractional degrees of crystallinity in the polymer sample by Equations 1-3 and 1-4, respectively. In the context of density method, knowledge of the density of a completely crystalline material (ρ_c) and completely amorphous material (ρ_a) is necessary. Typically, the ρ_c is calculated based on the knowledge of crystal unit cell parameters while the ρ_a is either experimentally measured if a completely amorphous state can be prepared upon rapid quench or calculated by extrapolation methods. It should be noted that the validity of the density method relies on the assumptions that ρ_a is independent of the size of the amorphous phase and its orientation as well as that no voids exist in the specimen to be measured.

$$\phi_c = \frac{\rho - \rho_a}{\rho_c - \rho_a}$$
Eq. 1-3

$$x_c = \frac{\rho_c}{\rho}\left(\frac{\rho - \rho_a}{\rho_c - \rho_a}\right)$$

<div align="right">Eq. 1-4</div>

Another widely used and well-established method is wide angle X-ray diffraction (WAXD), which is most sensitive to the electron density difference present in the crystalline and amorphous phases. In a WAXD measurement, the crystallites yield sharp diffraction reflections and, instead, the amorphous materials give rise to diffuse halos, and consequently, the degree of crystallinity can be determined by assessing the relative contribution of each component in the measured intensity. However, the challenge is that the contribution of X-ray absorption, incoherent scattering, etc. to the diffusive background should be appropriately corrected and that a reliable boundary separating the diffraction peaks and the underlying amorphous background should be drawn properly. Ruland thoroughly demonstrated a proper treatment of the scattering background arising from incoherent scattering, lattice imperfections, thermal vibrations and determined the degree of crystallinity of polypropylene by WAXD.[31] Concerning the boundary between crystalline and amorphous phases in the diffraction, the amorphous halos from a fully disordered sample could be taken to represent of the amorphous phase in the semi-crystalline sample and therefore, provide assistance in the separation.

1.4 Correlating the Semi-Crystalline Morphology with the Hole Transport Properties in rr-P3HT

1.4.1 Correlation Based on rr-P3HT OFET Devices

As stated in 1.2, achieving desirable orientations of polymer chains at the dielectric interface is of critical importance for enhancing the hole transport along the conduction channel in OFET devices. Taking rr-P3HT as an example, chains within the nanocrystals mostly adopt three distinct orientations with respect to the underlying

substrate, namely edge-on, face-on and vertical, respectively.[32] As suggested by both experimental[33–35] and theoretical results,[14] the hole mobility exhibits highly anisotropic characteristics along different axes in rr-P3HT with the polythiophene backbone direction (c-axis) providing the most efficient pathways for intramolecular hole transport. Along π-π stacking direction (b-axis), the second most efficient route for holes, the intermolecular hole transport between the adjacent chains is greatly promoted; while, due to the presence of insulating alkyl chain along the edge-on direction (a-axis), the hole mobility is largely limited. Based on the hole mobility measured in OFET devices comprising rr-P3HT films with different regioregularities, Sirringhaus et al. reported a large hole mobility anisotropy of more than 100-fold, which was attributed to the markedly different chain orientations within the crystalline domains.[15] In particular, the dominant edge-on orientation was shown to result in the hole mobility as high as 0.1 $cm^2V^{-1}s^{-1}$ owing to the in-plane intermolecular π-π stacking which highly delocalizes the holes between adjacent chains. Consequently, the chain orientation within the crystalline domain was proposed to limit the charge transport properties. The charge transport anisotropy associated with the rr-P3HT chain orientation is further supported by an investigation on the effect of surface treatment on OFET performance by Kline et al. where the self-assembled monolayers (SAMs) were varied from hexamethyldisilizane (HDMS) to octadecyltrichlorosilate (OTS).[23] Using X-ray diffraction rocking curves allows a direct examination of chain orientation at the critical buried interface between rr-P3HT and the dielectric where the flow of charge carriers occurs. Thus, a correlation between the hole mobility and rr-P3HT crystal orientation is established where the 100-fold increase in hole mobility observed in low and medium molecular weight rr-P3HT on OTS-treated silicon oxide substrate

compared to HDMS-treated one is attributed to the highly oriented rr-P3HT crystals at the buried interface with preferential in-plane π-π stacking and more importantly, the less misoriented grain boundaries between the crystal lamellae as schematically shown in Figure 1.4.
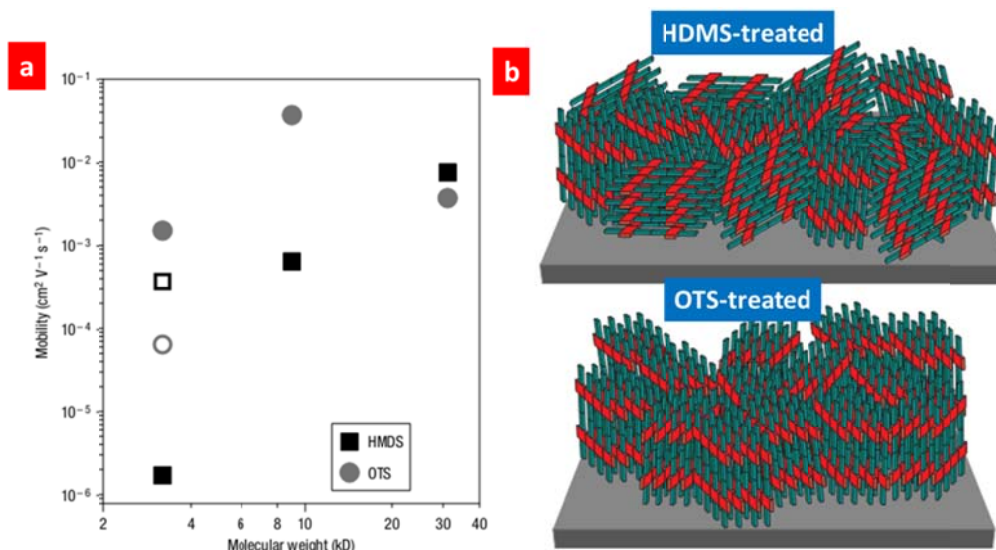
Figure 1.4: (a) Effect of molecular weight and surface treatment on the hole mobility of rr-P3HT based OFET;[23] (b) Schematics illustrating the small molecular weight rr-P3HT crystal chain packing at the buried interface with HDMS- and OTS-treated substrates. The crystals are more oriented on OTS-treated interface and have better-aligned grain boundaries.[23]

In addition to the chain packing and orientations in semi-crystalline rr-P3HT, morphological factors such as grain boundaries or the degree of crystallinity,[18,35] chain conformations,[36] coplanarity and resulting electronic structures,[16] presence of crossing points or tie chains,[14,33–35] are most frequently discussed and, hence, are linked to both intermolecular/intergranular and intramolecular/intragranular hole transport properties in rr-P3HT. A general understanding is that the macroscopic hole transport properties are complicated by the semi-crystalline nature of rr-P3HT as crystalline and amorphous phases coexist with finite size, indicating holes must travel through both phases and are

limited differently depending on the material properties (e.g. molecular weights, regioregularities, etc.) and the corresponding morphologies. To evaluate the contribution from each phase in rr-P3HT, Pingel et al. measured the hole mobility of rr-P3HT with different molecular weights at a local and macroscopic scale by PR-TRMC and OFET, respectively.[21] As shown in Figure 1.5, it is interesting to note that while the OFET hole mobility increases with the molecular weight, the intra-granular hole mobility is weakly dependent on the molecular weight of the material and remains on the order of 10^{-2} cm^{2}v^{-1}s^{-1}, suggesting that the variations in macroscopic hole transport that are commonly reported with different rr-P3HT molecular weights are likely related to the amorphous phase surrounding the crystalline phase. Following further temperature-dependent OFET hole mobility and absorption measurements, it is concluded that the long tie chains spanning neighboring crystalline domains in high molecular weight sample effectively transport the holes by bypassing the amorphous phase and are responsible for the enhanced hole mobility at high temperatures; whereas, the increasing amounts of amorphous phase in the low molecular weight samples at elevated temperatures impose greater barrier for intergranular hole transport and significantly limit the hole mobility. Similar arguments based on the molecular weights are implied or reported in several other studies as well.[14,18,33,34]

It is worth noting that, depending on the material properties (e.g. molecular weights, polydispersity (PDI) and regioregularities) and measurement conditions (e.g. temperature, etc.), the aforementioned morphological parameters, by influencing both the intra- and inter-granular hole transport to various extents, are of direct consequence for the ultimate macroscopic hole transport properties in rr-P3HT based OFET devices.
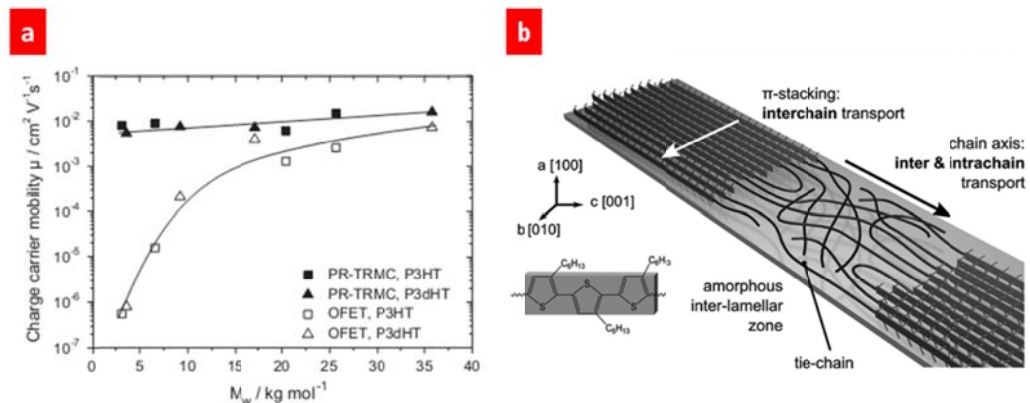
Figure 1.5: (a) Molecular weight dependence of OFET (open symbols) and PR-TRMC (filled symbols) hole mobility of rr-P3HT at room temperature.[21] (b) Schematic showing the crystalline and amorphous phases in rr-P3HT where the intrachain pathway for hole transport is along the backbones and tie-chains while the interchain pathway along the π-π stacking direction.[33]

1.4.2 Correlation based on rr-P3HT TOF devices

The TOF technique probes the hole transport in a thick rr-P3HT film with a typical thickness in the micrometer range, thus providing assessment on transport properties in the bulk of materials where the influence from the interface is likely negligible. Similar to OFET studies, the effects of molecular weight[19] and regioregularity[20] of rr-P3HT on the TOF hole mobility have been systematically investigated, where hole mobility on the order of 10^{-4} $cm^2V^{-1}s^{-1}$ is commonly reported. The smaller value of hole mobility in comparison with that measured by OFET can be attributed to the distinct natures of the two techniques as described in 1.2. Interestingly, contrary to the findings from OFET results, the TOF hole mobility of rr-P3HT was found to decrease by an order of magnitude from 10^{-4} $cm^2V^{-1}s^{-1}$ to 10^{-5} $cm^2V^{-1}s^{-1}$ with increasing molecular weight and the postulation given was that the possible twisting of the polymer backbone hinders the intra-chain transport.[19] In a study, by Mauer et al., on rr-P3HT with different regioregularities, similar values of hole mobility were reported

with the highly regioregular sample (RR>98%) showing a hole mobility of 10^{-4} cm^{2}V^{-1}s^{-1} which is an order of magnitude larger than that of a medium regioregular one (RR=94%).[20] However, it should be noted that not only do these two samples differ in regioregularity, the disparity in molecular weights is also non-negligible, thereby further complicating the data interpretation. As shown in Figure 1.6, the electric field dependence of the hole mobility in both samples is rather weak; meanwhile, although no detailed analysis on temperature dependence was given, the hole mobility clearly increases with increasing temperature for both samples in the temperature range investigated from ~203K to ~333K.

Compared to OFET studies, a clear understanding of the correlation between the bulk semi-crystalline morphology of rr-P3HT and the intrinsic hole transport characteristics measured by TOF is still lacking, especially at high temperature regions.
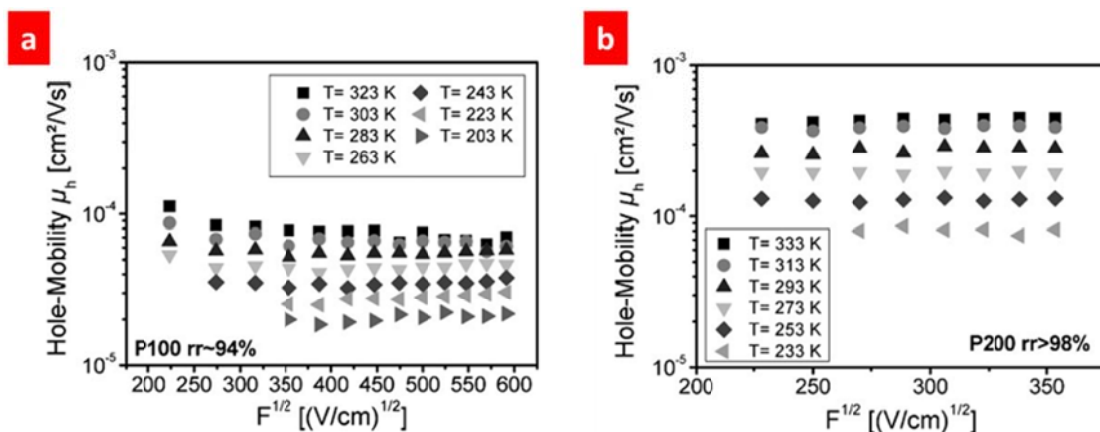
Figure 1.6: Field and temperature dependences of the hole mobility in rr-P3HT with (a) 94% regioregularity and (b) more than 98% regioregularity.[20]

1.5 References

1. Liu, F.; Gu, Y.; Jung, J. W.; Jo, W. H.; Russell, T. P. *J. Polym. Sci. Part B Polym. Phys.* **2012**, *50*, 1018–1044.

2.   Liu, F.; Gu, Y.; Shen, X.; Ferdous, S.; Wang, H.-W.; Russell, T. P. *Prog. Polym. Sci.* **2013**, *38*, 1990–2052.

3.   Thompson, B. C.; Fréchet, J. M. J. *Angew. Chem. Int. Ed. Engl.* **2008**, *47*, 58–77.

4.   DeLongchamp, D. M.; Kline, R. J.; Herzing, A. *Energy Environ. Sci.* **2012**, *5*, 5980–5993.

5.   DeLongchamp, D. M.; Kline, R. J.; Fischer, D. A; Richter, L. J.; Toney, M. F. *Adv. Mater.* **2011**, *23*, 319–337.

6.   Salleo, A.; Kline, R. J.; DeLongchamp, D. M.; Chabinyc, M. L. *Adv. Mater.* **2010**, *22*, 3812–3838.

7.   You, J.; Dou, L.; Yoshimura, K.; Kato, T.; Ohya, K.; Moriarty, T.; Emery, K.; Chen, C.-C.; Gao, J.; Li, G.; Yang, Y. *Nat. Commun.* **2013**, *4*, 1446.

8.   Shrotriya, V. *Nat. Photonics* **2009**, *3*, 447–449.

9.   Yang, H.; LeFevre, S. W.; Ryu, C. Y.; Bao, Z. *Appl. Phys. Lett.* **2007**, *90*, 172116.

10.   Chen, D.; Nakahara, A.; Wei, D.; Nordlund, D.; Russell, T. P. *Nano Lett.* **2011**, *11*, 561–567.

11.   Peet, J.; Kim, J. Y.; Coates, N. E.; Ma, W. L.; Moses, D.; Heeger, a J.; Bazan, G. C. *Nat. Mater.* **2007**, *6*, 497–500.

12.   Brinkmann, M. *J. Polym. Sci. Part B Polym. Phys.* **2011**, *49*, 1218–1233.

13.   Shen, X.; Duzhko, V. V.; Russell, T. P. *Adv. Energy Mater.* **2013**, *3*, 263–270.

14.   Lan, Y.-K.; Huang, C.-I. *J. Phys. Chem. B* **2009**, *113*, 14555–14564.

15.   Sirringhaus, H.; Brown, P.; Friend, R. *Nature* **1999**, *401*, 685–688.

16.   Zen, A.; Pflaum, J.; Hirschmann, S.; Zhuang, W.; Jaiser, F.; Asawapirom, U.; Rabe, J. P.; Scherf, U.; Neher, D. *Adv. Funct. Mater.* **2004**, *14*, 757–764.

17.   Kline, R. J.; McGehee, M. D.; Kadnikova, E. N.; Liu, J.; Fréchet, J. M. J. *Adv. Mater.* **2003**, *15*, 1519–1522.

18.   Kline, R.; McGehee, M.; Kadnikova, E. *Macromolecules* **2005**, *38*, 3312–3319.

19.   Ballantyne, A. M.; Chen, L.; Dane, J.; Hammant, T.; Braun, F. M.; Heeney, M.; Duffy, W.; McCulloch, I.; Bradley, D. D. C.; Nelson, J. *Adv. Funct. Mater.* **2008**, *18*, 2373–2380.

20. Mauer, R.; Kastler, M.; Laquai, F. *Adv. Funct. Mater.* **2010**, *20*, 2085–2092.

21. Pingel, P.; Zen, A.; Abellón, R. D.; Grozema, F. C.; Siebbeles, L. D. A.; Neher, D. *Adv. Funct. Mater.* **2010**, *20*, 2286–2295.

22. Dinelli, F.; Murgia, M.; Levy, P.; Cavallini, M.; Biscarini, F.; de Leeuw, D. *Phys. Rev. Lett.* **2004**, *92*, 116802.

23. Kline, R. J.; McGehee, M. D.; Toney, M. F. *Nat. Mater.* **2006**, *5*, 222–228.

24. Koch, F. P. V.; Rivnay, J.; Foster, S.; Müller, C.; Downing, J. M.; Buchaca-Domingo, E.; Westacott, P.; Yu, L.; Yuan, M.; Baklar, M.; Fei, Z.; Luscombe, C.; McLachlan, M. a.; Heeney, M.; Rumbles, G.; Silva, C.; Salleo, A.; Nelson, J.; Smith, P.; Stingelin, N. *Prog. Polym. Sci.* **2013**, *38*, 1978–1989.

25. Rivnay, J.; Mannsfeld, S. C. B.; Miller, C. E.; Salleo, A.; Toney, M. F. *Chem. Rev.* **2012**, *112*, 5488–5519.

26. Balko, J.; Lohwasser, R. H.; Sommer, M.; Thelakkat, M.; Thurn-Albrecht, T. *Macromolecules* **2013**, *46*, 9642–9651.

27. Brinkmann, M.; Rannou, P. *Macromolecules* **2009**, *42*, 1125–1130.

28. Zhokhavets, U.; Erb, T.; Gobsch, G.; Al-Ibrahim, M.; Ambacher, O. *Chem. Phys. Lett.* **2006**, *418*, 347–350.

29. Clark, J.; Chang, J.-F.; Spano, F. C.; Friend, R. H.; Silva, C. *Appl. Phys. Lett.* **2009**, *94*, 163306.

30. Alexander, L. E. *X-ray Diffraction Methods in Polymer Science*; New York, Wiley-Interscience, 1969.

31. Ruland, W. *Acta Crystallogr.* **1961**, *14*, 1180–1185.

32. Aryal, M.; Trivedi, K.; Hu, W. W. *ACS Nano* **2009**, *3*, 3085–3090.

33. Crossland, E. J. W.; Tremel, K.; Fischer, F.; Rahimi, K.; Reiter, G.; Steiner, U.; Ludwigs, S. *Adv. Mater.* **2012**, *24*, 839–844.

34. Jimison, L. H.; Toney, M. F.; McCulloch, I.; Heeney, M.; Salleo, A. *Adv. Mater.* **2009**, *21*, 1568–1572.

35. O'Connor, B.; Kline, R. J.; Conrad, B. R.; Richter, L. J.; Gundlach, D.; Toney, M. F.; DeLongchamp, D. M. *Adv. Funct. Mater.* **2011**, *21*, 3697–3705.

36.   Noriega, R.; Salleo, A.; Spakowitz, A. J. *Proc. Natl. Acad. Sci. U. S. A.* **2013**, *110*, 16315–16320.

CHAPTER 2

ON THE STRUCTURE – HOLE TRANSPORT CORRELATIONS IN SEMI-CRYSTALLINE P3HT

2.1 Introduction

Electronic and optoelectronic applications of polymer-based organic semiconductors, such as organic light-emitting diodes (OLED), organic field-effect transistors (OFET), and organic photovoltaic devices (OPV), are currently approaching the stage of maturing technologies.[1,2] Most of these applications would benefit from the development of new materials with improved charge carrier transport properties and enhanced mobility. Among the numerous potential polymeric semiconductors, a regioregular poly(3-hexylthiophene) has become the prototypical p-type material due to its efficient performance in devices, an ease of processing and a good stability, advancing the commercialization of OPV products (e.g. large area flexible solar panels).[3–5] The initial success has subsequently stimulated a significant amount of synthetic efforts that have led to a widespread material availability in sufficient quantities, development of various structural isomers, like materials with different regioregularities,[4,6,7] and polymers with a wide range of molecular weights.[8–10]

Like all semi-crystalline polymers, rr-P3HT consists of an ordered crystalline phase, with closely packed conjugated chains, and a disordered amorphous phase.[11–13] Due to the nature of rr-P3HT, with a polythiophene backbone and pendant alkyl side-chains, there is also a possibility that rr-P3HT may have a nematic, liquid crystalline-like form, wherein the adjacent chains are oriented with respect to each other but there is no registry between them.[14] The crystalline phase consists of a monoclinic-type unit cells

with two chains per cell (a=1.60nm, b=0.78nm, c=0.78nm and γ=86.5°) as proposed in a recent rotation-tilt electron diffraction study.[15] An amorphous phase, on the other hand, has been modeled by a regiorandom P3HT.[16]

The differences in optical properties of rra-P3HT and rr-P3HT are assigned to a delocalization of electron wave functions along the planarized backbones (intra-chain), i.e. in the (001) direction, and along the π-π stacking (inter-chain), i.e. in the (020) direction, in the latter material.[17,18] Charge transport is more efficient along these directions, as compared to the (100) direction where it is prohibited by the insulating hexyl side chain. The larger mobility in materials with higher regioregularity, as shown with OFET[5] and time-of-flight techniques,[19] emphasizes the role of a high degree of local structural order for improving macroscopic charge transport properties. The preferential alignment of the π-π stacking along the macroscopic charge transport direction imparts an anisotropy into an otherwise random orientation of domains and leads to a further increase in mobility.[20] A recent study by Pingel et al.[21] shows a thermally-activated hole transport with similar activation energies for high molecular weight rr-P3dHT (Mn~27K) on the local length scale inside the crystalline domains, and on the macroscopic length scale, throughout the semi-crystalline material, measured by the pulse-radiolysis time-resolved microwave conductivity (PR-TRMC) and OFET measurements, respectively. Unlike in the low molecular weight counterpart (7.2K), a better interconnection between the ordered domains in the high molecular weight rr-P3dHT was argued to be responsible for the enhanced charge transport at high temperatures. On the other hand, the amorphous phase has also been argued to dictate the hole transport in rr-P3HT in several studies.[9,10] In general, it is clear that the hole transport properties in rr-P3HT vary with molecular

weight, regioregularity, temperature and more importantly, the morphology.[4,9,10,21,22] Thus, it would be worthwhile to establish a detailed correlation between the micro- and macroscopic structure in the semi-crystalline rr-P3HT and its hole transport properties, so as to better understand the interplay between the crystalline and amorphous phases.

In this chapter, by using the temperature-resolved TOF and WAXD techniques, we present a detailed investigation of the bulk rr-P3HT with a relatively high molecular weight (Mn~23K) and regioregularity (>98%), and correlate its structural evolution with the macroscopic hole transport at different temperatures. The transport-related structural features in the crystalline and amorphous phases are probed individually, in the regioregular and regiorandom P3HTs, respectively.

2.2 Experimental Section

2.2.1 Time-of-Flight Mobility Measurements

For TOF measurements, samples were prepared by a drop-casting method. A ~30 mg/ml solution of rr-P3HT (number-average molecular weight Mn~23k, PDI~2.0, regioregularity >98%) in ortho-dichlorobenzne (o-DCB) was carefully dropped onto pre-cleaned indium tin oxide (ITO) coated glass substrate (Thin Film Devices Inc.) on a flat surface inside a N_2-filled glove box. The slow evaporation of o-DCB resulted in a thick film (~1.8μm) with a smooth surface and uniform thickness. It is noteworthy that the well-controlled drop-cast process with uniform evaporation is important for sample preparation, since gradient structures and surface roughness were usually observed when the evaporation was non-uniform. The sample was kept in a vacuum oven overnight at room temperature to remove the residual solvent. Finally, a semi-transparent Al electrode (25nm thickness, 6mm^2 area) was thermally deposited onto the film under high vacuum

(2×10^{-6} mbar) using an evaporator in the glove box. The slow drying of a high-boiling point o-DCB after drop-casting of rr-P3HT solution produces a smooth, thick film. Unlike the spin-coated thin film, whose morphology is far removed from its equilibrium state, the morphology of the slow-dried film is expected to be closer to the thermodynamic equilibrium. All the TOF samples were thermally annealed at 210°C for 30min (as close to the melting point as the sample fabrication procedure permits in order to maintain the geometrical film integrity).

The third harmonic of a pulsed Nd:YAG laser (Continuum Lasers, Surelite II) was used for the photo-excitation of charge carriers at a 355 nm wavelength. Illumination by 4-6 ns pulses through the Al electrode produced a gradient of excess carrier concentration along the smallest film dimension due to a non-uniform light absorption at this wavelength. In order to apply an external bias voltage (V), either a set of electrochemical batteries or a power supply (Stanford Research Systems, PS3100) were used in different voltage ranges. The sign of the applied bias determines if electrons or holes move through the sample. In this study, the transport of holes is reported. The intensity of the laser pulse was kept sufficiently low to avoid a distortion of the electric field, due to a non-uniform distribution of photo-generated charge carriers. A Tektronix TDS 3052C oscilloscope was used to record the photocurrent transients, using a 50 Ω load resistor.

2.2.2 Temperature-Resolved Wide Angle X-ray Diffraction Measurements

For temperature-resolved WAXD measurements, a polymer powder was directly melted in a hermetically-sealed differential scanning calorimeter (DSC) pan on a heating stage inside a N_2-filled glove box. Since the pan would be placed vertically in WAXD

experiment, a sufficient amount of polymer was placed in the pan so that, during the experiments, the x-ray beam penetrates through the same thickness of sample, even when molten. After cooling to room temperature in the glove box, the pan was rapidly sealed using a crimper. Subsequently, the pan was heated to $250^{o}C$ in a DSC (TA instruments, Q200-DSC) and held at that temperature for 10min to remove any thermal history, then ramped down to $150^{o}C$ at a rate of $10^{o}C/min$ and finally annealed at $150^{o}C$ for 30min to induce ordering, prior to the WAXD measurement. Temperature-resolved WAXD measurements were performed on Beamline 7.3.3 at the Advanced Light Source (ALS) at the Lawrence Berkeley National Laboratory (LBNL). A transmission geometry was used. The wavelength of the x-rays is 1.240Å and the diffracted photons were collected by a two dimensional Pilatus 1M detector. A heating stage (Linkam) with a built-in sample cell accommodating the DSC sample pan, was mounted into the beamline with a sample-to-detector distance of ~302.6 mm. The sample was heated at a rate of $10^{o}C/min$ and then kept at each temperature set-point for 5 min. Each measurement was done with 60s exposure times. During the experiment, a N_2 atmosphere was maintained by purging with N_2. Correction for geometry and polarization was carried out for the diffraction followed by subtraction of background arising from the pan and parasitic scattering.

2.3 Results and Discussion

2.3.1 Hole Transport in rr-P3HT Measured by the TOF Technique

Shown in Figure 2.1 are the typical photocurrent transients measured in rr-P3HT films at $20^{o}C$ for different applied voltages. A clear shift of the transit time (τ_{tr}) to smaller values can be seen as the applied voltage increases from 5V to 15V, indicating that the passage of holes through the entire thickness of the film is accelerated with the higher

electric fields. The hole mobility is determined from Equation 1-1, $\mu = L^2/(\tau_{tr} \times V)$, where L and V are the film thickness and applied voltage, respectively.
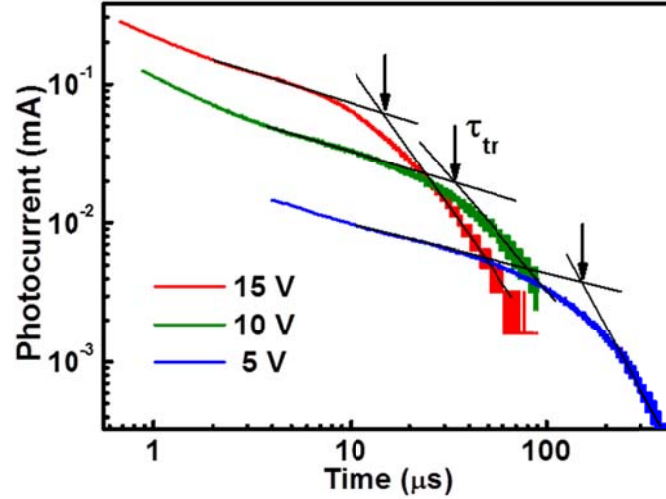
Figure 2.1: Typical photocurrent transients in rr-P3HT measured at $20^{\circ}C$ for various applied voltages. Transit times are indicated by the black arrows.

The temperature dependences of the hole mobility during the first cooling and second heating cycles are plotted in Figure 2.2. Basically, the hole mobility increases as temperature increases; however, above $\sim150^{\circ}C$, the hole mobility begins to decrease, giving rise to a maximum in both the heating and cooling ramps. Moreover, the change of hole mobility, shown on a semi-logarithmic scale in Figure 2.2 (b), is linear in $1/T^2$ below $120^{\circ}C$, as indicated by the linear fit. This behavior has been successfully reproduced on several samples. We note that the temperature-resolved TOF measurements have been previously reported for rr-P3HT,[19,23] however neither a maximum in the mobility nor a negative slope of the temperature dependence have been observed, due to the lower temperature range of those measurements.
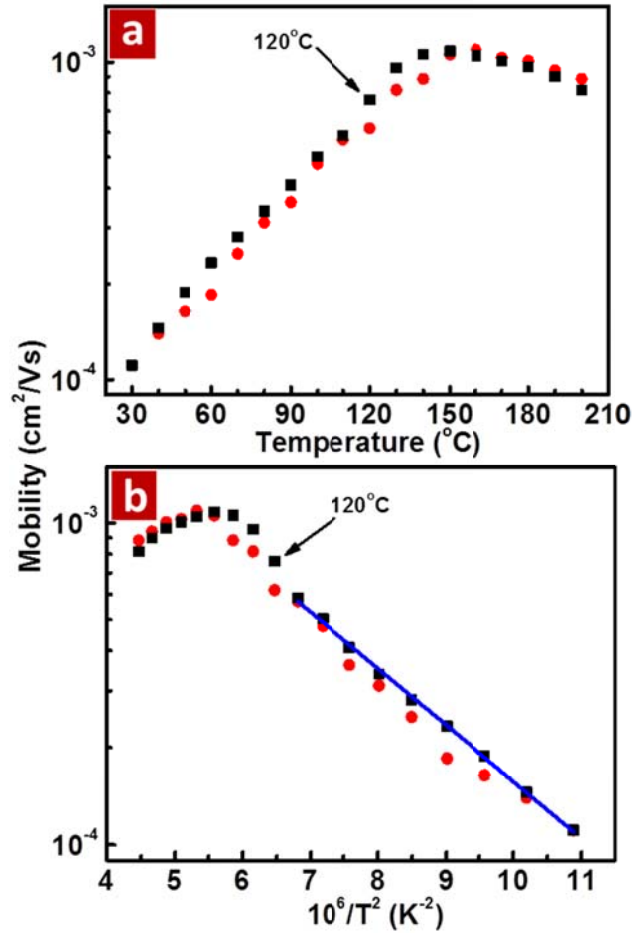
Figure 2.2: Temperature dependence of hole mobility in rr-P3HT on heating (red circles) and cooling (black squares): (a) mobility vs T; (b) mobility vs $10^6/T^2$. The blue line is the linear fit.

The Gaussian Disorder Model (GDM),[24] which, on the basis of Monte Carlo simulations, describes the charge carrier hopping in a Gaussian density of states with a Miller-Abrahams-type rate, was used to analyze the data. Within the framework of this model, an empirical expression for charge carrier mobility (μ) is given by Equation 2-1, where μ_0 is the mobility prefactor, σ/kT is the energetic disorder (width of the density of states) normalized to thermal energy, Σ is the positional disorder, E is the applied electric field, k is the Boltzmann constant and C is an empirical constant.

24

$$\mu(T,E) = \mu_0 \exp[-(\frac{2\sigma}{3kT})^2] \exp\{C[(\frac{\sigma}{kT})^2 - \Sigma^2]\sqrt{E}\} \qquad \text{Eq. 2-1}$$

According to Equation 2-1, the logarithmic hole mobility decreases linearly with increasing $1/T^2$ which is in good agreement with the data below 120$^\text{o}$C, shown in Figure 2.2 (b). This implies that the increase of hole mobility at lower temperatures is due to a thermal activation of the elementary hopping events. The linearity, however, clearly deviates in the range of high temperatures (above ~120$^\text{o}$C), suggesting a possible structural change with increasing temperature. Also, it is evident that the temperature dependence of hole mobility is reversible on heating and cooling and, therefore, not related to any irreversible structural changes. Furthermore, the electric field dependence of the hole mobility, shown in Figure 2.3, provides more insight into the correlation between hole transport and potential structural change.
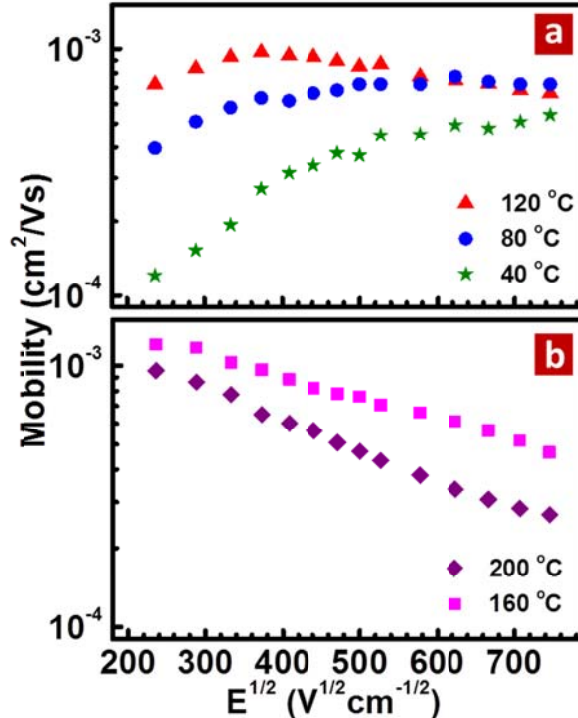
Figure 2.3: Electric field dependence of hole mobility in rr-P3HT at fixed temperatures: (a) at 40$^\text{o}$C (star), 80$^\text{o}$C (circle) and 120$^\text{o}$C (triangle); (b) at 160$^\text{o}$C (square) and 200$^\text{o}$C (diamond).

For T<120°C (40°C and 80°C in Figure 2.3 (a)), the mobility initially increases with increasing electric field, i.e. shows a positive slope in the range of small electric fields, and then levels off; while for T>120°C (160°C and 200°C in Figure 2.3 (b)), the mobility shows a continuous, linear decrease over the entire E$^{1/2}$ range, giving rise to a negative slope. Notably, the mobility measured at 200°C is smaller than that at 160°C across the same E$^{1/2}$ range, which is consistent with the decrease seen in its temperature dependence. It is interesting to note that the temperature of 120°C, at which no significant electric field dependence is seen, seems to be the point at which the change of the slope occurs, which is in good agreement with the onset of the deviation observed in the temperature dependence. The GDM was used to understand the sign reversal of the slope in the electric field dependence of mobility. According to Equation 2-1, the slope is given by the difference between $(\sigma/kT)^2$ and Σ^2 at fixed temperatures. Thus, the relative magnitude of the energetic disorder parameter, a measure of the width of density of states (DOS) normalized to the thermal energy, and the positional disorder parameter, a measure of the inter-site separation and coupling, can be evaluated and related to the difference in the hole mobility over different temperature ranges. In the recent work by Mozer et al.,[25,26] a negative field dependence was also observed, however, starting at a much lower temperature of ~250K (~-23°C), above which, a negative electric field dependence was maintained up to 310K (~37°C). This significantly differs from our electric field dependence results which show a positive dependence up to 120°C. Although there is no information provided regarding the rr-P3HT employed in their study, this difference might be explained by the differences in the rr-P3HTs studied, which, in turn, would also result in different energetic and positional disorder parameters. In short,

the functional dependences of the hole mobility on the temperature and electric field unambiguously suggest a structural change of rr-P3HT at high temperatures. Consequently, the knowledge of structural changes, namely the changes in crystalline and amorphous phases at different temperatures, is required to fully understand the charge carrier transport properties.

Considering the semi-crystalline nature of rr-P3HT, it is not possible to examine the crystalline and amorphous phases separately. To approach this problem, regiorandom P3HT (rra-P3HT, Mn~22k, PDI~3.3, regioregularity~57.7%), which is amorphous[19] and chemically identical to rr-P3HT, has been introduced to model the amorphous phase existing in rr-P3HT.[16]

2.3.2 Thermal Evolution of the Structure of rr-P3HTs Probed by WAXD

The temperature dependence of the (100) and (020) reflections in the rr-P3HT on heating is shown in Figure 2.4. The changes in the peak intensities (I_{max}) and the full widths at half maximum (FWHM) are also shown. As can be seen in Figure 2.4 (a), the (100) spacing, characteristic of the distance between the ordered rr-P3HT backbones that are separated by the alkyl side chains, shows a continuous increase with temperature over the entire range from $30^{o}C$ to $230^{o}C$. This expansion along the a direction was also reported recently in a thin-film geometry.[22,27–29] Considering a resemblance between the hexyl side chain and linear polyethylene (PE), the expansion of rr-P3HT along the a direction is somewhat unexpected, since the thermal expansion along the PE backbone is negligible.[30] According to the electron diffraction study by Brinkmann et al.,[15] the hexyl side chains of rr-P3HT are not interdigitated and are tilted with respect to the a,c plane. Based on the temperature-resolved infrared spectroscopy measurements by Tashiro et

al.,[14] the initial expansion along the *a* direction for T<120°C can be associated with the conformational changes of the side chains, the *gauche*$^{\pm}$ conformations in the place of planar *trans* conformation, at higher temperatures.[14,31] The C-C bond rotation would result in a change in the tilting angle of hexyl side chains and, therefore, in an increase in the separation distance between the backbones.
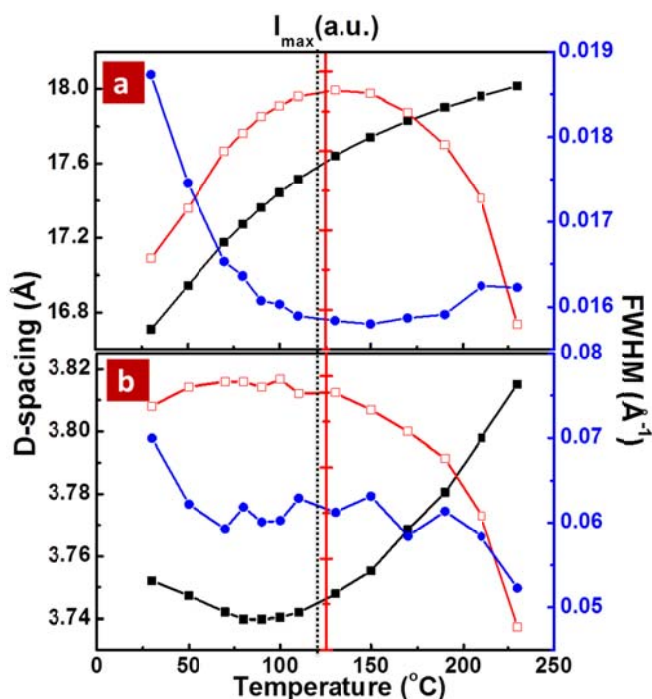
Figure 2.4: Thermal evolution of d-spacing (black square), peak full widths at half maximum (FWHM) (blue circle), peak intensity (I_{max}) (red open square) of different crystal planes in rr-P3HT during heating: (a) (100) plane; (b) (020) plane. Two distinct regions have been divided by the dotted line.

A continuous increase of the persistence length along the (100) direction is evidenced by the decreasing FWHM of this reflection from 30°C to 120°C, while the overall ordering is improving over the same temperature range, as indicated by the increase in the peak intensity. The persistence length regarding the (100) packing was calculated to be ~35nm by the Scherrer equation: L=0.9λ/($\beta\times$cosθ), where λ is the wavelength of the incident x-rays, β is the FWHM (2θ), and θ is the Bragg angle. At the

temperatures above 120°C, the persistence length levels off and decreases when approaching the melting point. Meanwhile, the peak intensity starts to plummet, indicating either a reduction in the crystal packing, while the total number of crystals per unit volume remains constant, or that the number of crystals per unit volume has decreased due to a thermal expansion.
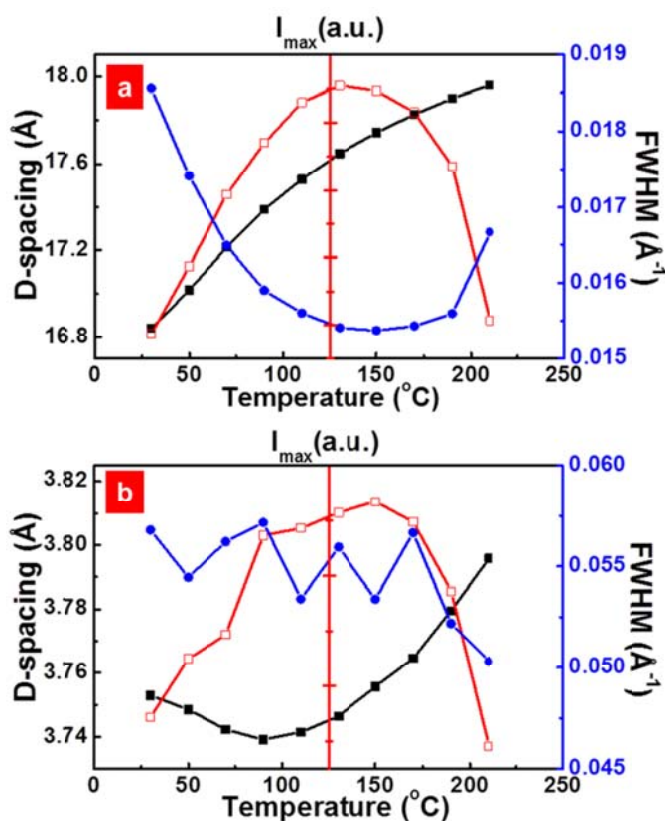
Figure 2.5: Thermal evolution of d-spacing (black square), peak full widths at half maximum (FWHM) (blue circle), peak intensity (I_{max}) (red open square) of different crystal planes in rr-P3HT during cooling: (a) (100) plane; (b) (020) plane.

The change of d-spacing, I_{max} and FWHM in the (020) reflection, characteristic of π-π stacking, is shown in Figure 2.4 (b). It is interesting to note that the (020) spacing initially decreases, then levels off from ~70°C to 110°C and increases monotonically with increasing temperature prior to melting. Similar to the initial expansion along the (100)

direction, the change of tilting angle of hexyl side chain during heating is likely responsible for the initial shrinkage along the π-π stacking direction as well. The persistence length of the crystals along the π-π stacking direction shows an initial increase, then, plateaus near ~70°C before reaching the melting point. The Scherrer analysis yields a persistence length of ~10 nm along the π-π stacking direction. Finally, the peak intensity, relevant to the ordering and crystallinity in the system, remains relatively constant up to ~130°C followed by a decrease with increasing temperature as the melting point is approached. This trend is similar to that seen in the (100) direction. On cooling, almost identical d-spacing and similar changes in the FWHM and I_{max} were found along both the (100) and (020) directions as shown in Figure 2.5, indicating a reversibility of the structural change as a function of temperature.

Thus, the structural evolution of rr-P3HT on heating and cooling can be divided into two temperature regions as shown by the dotted line in Figure 2.4. In Region I, from 30°C to ~120°C, there is an initial expansion along the (100) direction (~0.47Å) and a shrinkage along the (020) direction (~0.01Å), due to a disordering process in the side chain induced by the introduction of the *gauche*$^{\pm}$ conformation. The persistence length and ordering in both directions are increasing. Subsequently, the π-π stacking distance plateaus at ~3.74Å while the (100) spacing continues to expand (~0.34 Å). Meanwhile, the ordering and persistence of (100) crystal planes continue to increase, whereas, those of the (020) crystal planes remain relatively constant. The degree of crystallinity of the rr-P3HT at 30°C was determined to be ~59%, suggesting a comparable mass fraction of crystalline and amorphous phases. In Region II above 120°C, a loss in the ordering occurs close to the melting point along both the (100) and (020) directions, resulting in a

decrease of crystallinity. A detailed analysis of the degree of crystallinity as a function of temperature is undergoing and will be summarized elsewhere. The linear thermal expansion coefficients along the (100) and (020) directions are determined for T<120°C: $\alpha_{(100)}$ = 6.1×10^{-4} ^{o}C^{-1} and $\alpha_{(020)}$ = -6.6×10^{-5} ^{o}C^{-1} (shrinkage); and for T>120°C: $\alpha_{(100)}$ = 2.2×10^{-4} ^{o}C^{-1} and $\alpha_{(020)}$ = 1.8×10^{-4} ^{o}C^{-1}. Their similarity at higher temperatures to that of an amorphous PE (1.7~2.7×10^{-4} ^{o}C^{-1})[32] indicates a 3-dimensional thermal expansion of disordered hexyl side chain. We suggest that there is a nematic-like liquid crystal phase in Region II, based on the fact that the side chains are in the molten state while the ordered packing of polythiophene backbones is preserved. Notably, larger expansion was observed along both the (100) (~0.5Å) and (020) (~0.08Å) directions in comparison to Region I. Interestingly, at ~120°C, where the Region II in structural data begins, the turning point in TOF data is also seen. The hole transport along the polythiophene backbone, i.e. (001) direction, the fastest propagation pathway, is not expected to change significantly with increasing temperature due to the covalent bonding along the chain. The (100) direction, along the insulating hexyl side chains between the backbones, has limited influence on the hole transport as compared to the more favored π-π stacking direction. Consequently, two mechanisms can be considered to account for the rate-limiting step in the hole mobility above 120°C: (i) the microscopic π-π stacking expansion inside the crystalline phase which may decrease the hole mobility due to an increase in the hopping distance or (ii) the macroscopic decrease in the crystallinity which would require for holes to pass a greater distance in the amorphous phase. Since the transition between the two regions of distinct structural behavior is rather broad, we

took a melting point of PE as boundary between them, and relate the structural changes within each region to the respective behavior of hole mobility.

2.3.3 Thermal Evolution of the Structure of rra-P3HTs Probed by WAXD

In order to model the amorphous phase in the rr-P3HT, following a previously published approach,[16] we studied the structural properties of rra-P3HT. In contrast to the semi-crystalline rr-P3HT, only two broad halos are seen in the WAXD for rra-P3HT, as shown in Figure 2.6.
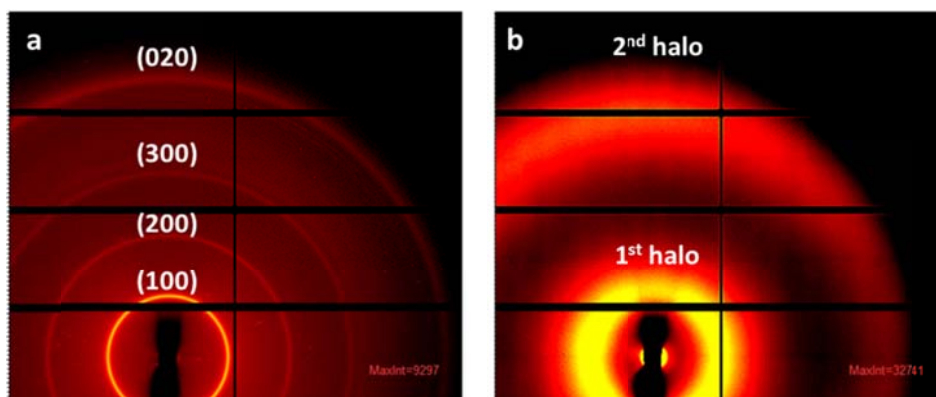
Figure 2.6: Wide angle X-ray diffraction patterns at 30°C: (a) rr-P3HT; (b) rra-P3HT.

A very interesting thermal behavior was seen in the temperature dependence of the I(q) *vs.* q profiles, shown in Figure 2.7. From these data, it can be seen that the position of the halo at q~1.45Å^{-1}, corresponding to a spacing of 4.34Å, shifts to a smaller q with increasing temperature; while the position of the halo at q~0.41Å^{-1}, corresponding to a spacing of 15.3Å, remains constant as the temperature increases from 30°C to 250°C. To understand the difference in the thermal behavior of these two halos, the origins of the halos must be understood. For this purpose, a series of regioregular poly(3-alkylthiophene)s (rr-P3AT) with different alkyl chain lengths, ranging from butyl side chain for P3BT to decyl side chain for P3DT, were brought above their respective

melting points and their diffraction patterns were measured. Two halos were observed for all the molten P3ATs, representing a common amorphous state of P3ATs above T_m. The d-spacings of the halos in each material are tabulated in Table 2.1.
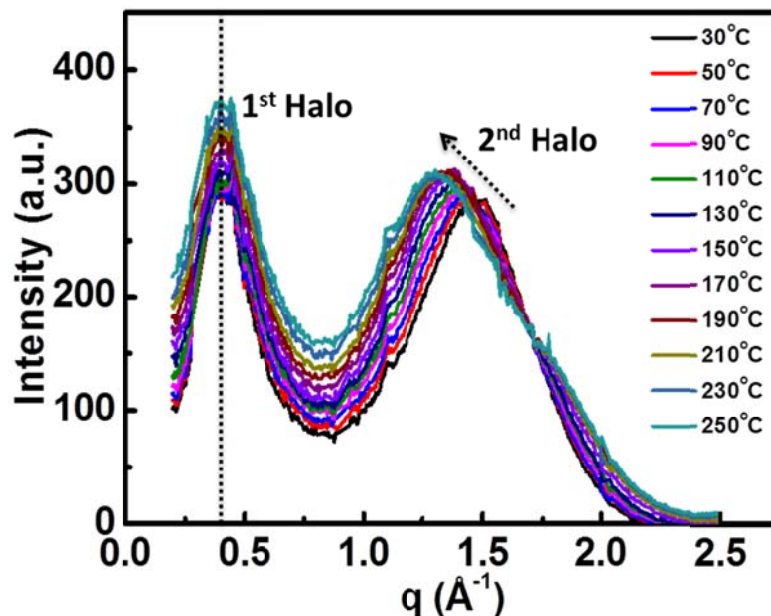
Figure 2.7: I(q) vs q profiles showing change of two amorphous halos in rra-P3HT during heating.

Table 2.1: D-spacing comparison of amorphous halos in different P3ATs.

	1st Halo d-spacing / Å	2nd Halo d-spacing / Å
rr-P3BT	12.0	4.75
rr-P3HT	15.7	4.76
rr-P3OT	18.5	4.69
rr-P3DT	20.9	4.75
rra-P3HT	15.3	4.80

Notably, the d-spacings of the second halos are very similar (~4.7 Å), while those of the first halos showed a consistent increase as the length of side chains increase from butyl to decyl. Consequently, the first and second halos have been assigned to the

averaged inter- and intra-molecular separation distances, respectively. Schematically shown in Figure 2.8, the temperature dependent WAXD results of rra-P3HT indicate that the intramolecular distance increases as a result of thermal expansion; however, although the backbones become more twisted and distorted at higher temperatures, the average intermolecular distance between the neighboring backbones remains unchanged. Taking the rra-P3HT as a model of amorphous phase in the rr-P3HT, the constant intermolecular distance in the rra-P3HT implies that the charge hopping distance between the neighboring chains in the amorphous phase of rr-P3HT is independent of temperature.
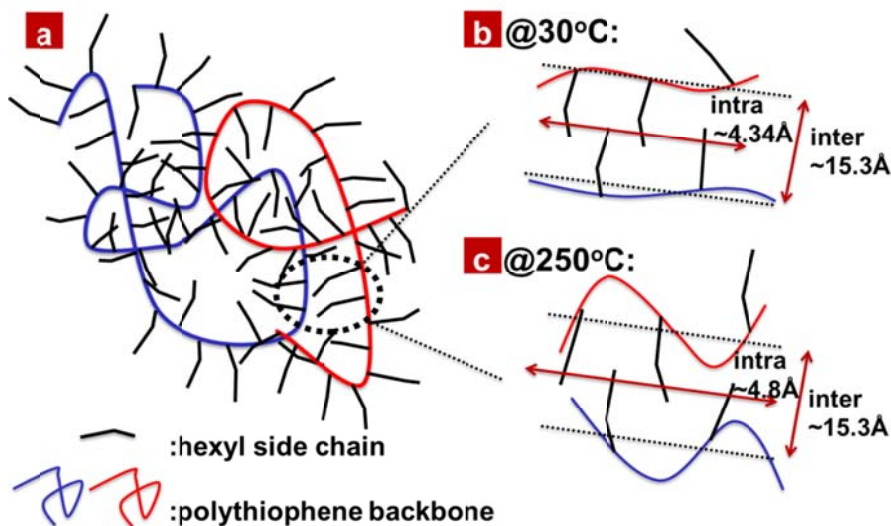
Figure 2.8: Molecular structure of rra-P3HT: (a) an overview of two chains; (b) localized view at 30°C; (c) localized view at 250°C. The dotted lines in (b) and (c) represent the averaged chain axes. The intermolecular distance is ~15.3Å, independent of temperature; intramolecular distance increases from ~4.34Å to ~4.8Å as a result of thermal expansion.

2.3.4 Discussions on the Structure – Hole Transport Correlations

The picture of hole transport in the bulk rr-P3HT over a broad temperature range can be unveiled from the TOF results, in conjunction with the temperature-resolved WAXD data. Below 120°C (Region I), the logarithmic hole mobility changes linearly

with $1/T^2$, showing a typical thermally-activated hopping which can be described by the GDM. In the corresponding WAXD data, there is no significant change in the d-spacing and crystal persistence length along π-π stacking direction, supporting the applicability of GDM with the temperature-independent energy and positional disorder parameters. From the electric field and temperature dependences of hole mobility below 120°C, the σ, Σ and C were determined to be 116 meV, 3.3 and 7.9×10^{-4} $(cm/V)^{1/2}$, respectively. An alternate approach is to extract σ from the slope of logarithmic zero field mobility $vs.$ $1/T^2$. The values of Σ and C can be calculated from the slope of electric field dependence $(dln\mu/dE^{1/2})$, assuming that σ is constant at lower temperatures. Similar values of σ=124 meV, Σ=3.6 and C=7×10^{-4} $(cm/V)^{1/2}$ were obtained. The positional disorder parameter Σ agrees well with value of 3.3 reported by Mozer et al.;[25] however, the energetic disorder parameter σ is somewhat larger than the typical values previously reported for different rr-P3HTs,[19,23,25] suggesting that the difference in the materials might be responsible for this disagreement. Indeed, σ and Σ in our calculations are very similar to the representative values reported for disordered polymers,[24] implying that the amorphous phase surrounding the crystalline phase, hence, limits the charge carrier transport in Region I. This is also supported by a comparison to the temperature dependence data for rr-P3HT obtained from PR-TRMC, which probes the charge transport on a local length scale inside a crystalline domain and, therefore, depends weakly on the molecular weight.[21] The slope derived from the hole mobility $vs.$ $1/T^2$ in PR-TRMC[21] is two orders of magnitude smaller than that from our TOF data in Region I, indicating that the energetic disorder is larger in the case of macroscopic hole transport, which is limited by the amorphous phase in between the crystalline phases.

Above 120°C (Region II), the increase in the distance between the hopping sites along the π-π stacking direction in the liquid crystal phase and the increase of the amorphous phase concentration occur simultaneously and both can contribute to the decrease in the hole mobility at high temperatures. Assuming that (i) the hole mobility inside the liquid crystal phase remains much larger than in the amorphous phase despite the thermal expansion along the π-π stacking direction and taking into account that (ii) there is no thermal inter-molecular expansion in the amorphous phase, the effect of reduced crystallinity can be further rationalized – the holes travel longer distance in the amorphous phase, resulting in a lower hole mobility. It is interesting to note that the negative slope in temperature and electric field dependences of hole mobility have been recently observed in a discotic liquid crystal mesophase of the triphenylene derivative.[33] Though those data were interpreted in terms of a reduced electron transfer integral due to the thermal activation of phonon modes, they can be described by the thermal expansion along the π-π stacking direction in the columns equally well. This might indicate that the two types of organic materials share the same charge transport mechanism in the respective temperature ranges.

Here, we would like to note that our goal was to characterize the bulk structural and charge transport properties of rr-P3HT and, therefore, the TOF and WAXD techniques with "thick-film" and powder sample geometries, respectively, were selected. Also, the sample fabrication procedures were optimized for the material morphology to be as close to the thermodynamic equilibrium as possible in both cases. A complete thermal reversibility of structural and charge transport data was used as an indication. However, though we think that our choice of experimental techniques and optimized

sample preparation conditions has led to that fact that the structural and charge carrier transport properties were compared on the same physical length-scales and in the nearly-identical experimental conditions, the sample geometries and preparation conditions were different.

2.4 Conclusions

In this Chapter, the structural changes of rr-P3HT have been shown to influence the intrinsic hole transport in the bulk rr-P3HT with changing temperature. A separate examination of the amorphous phase in the rr-P3HT is assisted by the introduction of an amorphous rra-P3HT in which a temperature-independent intermolecular distance was observed. For $T<120^{o}C$, no significant hole transport-related structural changes are found and GDM is suitable to describe the hole transport. The temperature and electric field dependences of the hole mobility yield the energetic disorder ($\sigma\sim120meV$) and the positional disorder ($\Sigma\sim3.33$) parameters, suggesting that the amorphous phase in rr-P3HT limits the hole transport. For $T>120^{o}C$, the GDM with temperature-independent parameters is no longer applicable and both the decreased crystallinity and π-π stacking expansion occur simultaneously, either of which could lead to a decrease in the hole mobility in rr-P3HT at high temperatures. The correlated, temperature-dependent studies of structural properties and charge carrier transport mechanisms facilitate in understanding the material functionality upon its incorporation into electronic and optoelectronic devices. This not only allows gaining a better understanding of the mechanisms of device operation at various temperatures but also serves as an efficient tool for a further optimization of the material properties and device performance.

2.5 References

1. Dennler, G.; Scharber, M. C.; Brabec, C. J. *Adv. Mater.* **2009**, *21*, 1323–1338.

2. Brabec, C. J.; Cravino, A.; Meissner, D.; Sariciftci, N. S.; Fromherz, T.; Rispens, M. T.; Sanchez, L.; Hummelen, J. C. *Adv. Funct. Mater.* **2001**, *11*, 374–380.

3. Dang, M. T.; Hirsch, L.; Wantz, G. *Adv. Mater.* **2011**, *23*, 3597–3602.

4. Woo, C. H.; Thompson, B. C.; Kim, B. J.; Toney, M. F.; Fréchet, J. M. J. *J. Am. Chem. Soc.* **2008**, *130*, 16324–16329.

5. Sirringhaus, H.; Tessler, N.; Friend, R. H. *Science* **1998**, *280*, 1741–1744.

6. Kim, Y.; Cook, S.; Tuladhar, S. M.; Choulis, S. A.; Nelson, J.; Durrant, J. R.; Bradley, D. D. C.; Giles, M.; McCulloch, I.; Ha, C.-S.; Ree, M. *Nat. Mater.* **2006**, *5*, 197–203.

7. McMahon, D. P.; Cheung, D. L.; Goris, L.; Dacuña, J.; Salleo, A.; Troisi, A. *J. Phys. Chem. C* **2011**, *115*, 19386–19393.

8. Kline, R. J.; McGehee, M. D.; Kadnikova, E. N.; Liu, J.; Fréchet, J. M. J. *Adv. Mater.* **2003**, *15*, 1519–1522.

9. Zen, A.; Saphiannikova, M.; Neher, D. *Macromolecules* **2006**, *39*, 2162–2171.

10. Kline, R.; McGehee, M.; Kadnikova, E. *Macromolecules* **2005**, *38*, 3312–3319.

11. Chen, D.; Liu, F.; Wang, C.; Nakahara, A.; Russell, T. *Nano Lett.* **2011**, *11*, 2071–2078.

12. Chen, D.; Nakahara, A.; Wei, D.; Nordlund, D.; Russell, T. P. *Nano Lett.* **2011**, *11*, 561–567.

13. Brinkmann, M.; Rannou, P. *Adv. Funct. Mater.* **2007**, *17*, 101–108.

14. Tashiro, K.; Ono, K.; Minagawa, Y.; Kobayashi, M.; Kawai, T.; Yoshino, K. *J. Polym. Sci. Part B Polym. Phys.* **1991**, *29*, 1223–1233.

15. Kayunkid, N.; Uttiya, S.; Brinkmann, M. *Macromolecules* **2010**, *43*, 4961–4967.

16. Vakhshouri, K.; Kozub, D. R.; Wang, C.; Salleo, A.; Gomez, E. D. *Phys. Rev. Lett.* **2012**, *108*, 026601.

17. Jiang, X. M.; Österbacka, R.; Korovyanko, O.; An, C. P.; Horovitz, B.; Janssen, R. A. J.; Vardeny, Z. V. *Adv. Funct. Mater.* **2002**, *12*, 587–597.

18. Clark, J.; Silva, C.; Friend, R.; Spano, F. *Phys. Rev. Lett.* **2007**, *98*, 206406.

19. Mauer, R.; Kastler, M.; Laquai, F. *Adv. Funct. Mater.* **2010**, *20*, 2085–2092.

20. Sirringhaus, H.; Brown, P.; Friend, R. *Nature* **1999**, *401*, 685–688.

21. Pingel, P.; Zen, A.; Abellón, R. D.; Grozema, F. C.; Siebbeles, L. D. A.; Neher, D. *Adv. Funct. Mater.* **2010**, *20*, 2286–2295.

22. Joshi, S.; Pingel, P.; Grigorian, S.; Panzner, T.; Pietsch, U.; Neher, D.; Forster, M.; Scherf, U. *Macromolecules* **2009**, *42*, 4651–4660.

23. Ballantyne, A. M.; Chen, L.; Dane, J.; Hammant, T.; Braun, F. M.; Heeney, M.; Duffy, W.; McCulloch, I.; Bradley, D. D. C.; Nelson, J. *Adv. Funct. Mater.* **2008**, *18*, 2373–2380.

24. Bassler, H. *Phys. Status Solidi* **1993**, *175*, 15–56.

25. Mozer, A. J.; Sariciftci, N. S. *Chem. Phys. Lett.* **2004**, *389*, 438–442.

26. Mozer, A.; Sariciftci, N.; Pivrikas, A.; Österbacka, R.; Juška, G.; Brassat, L.; Bässler, H. *Phys. Rev. B* **2005**, *71*, 035214.

27. Lilliu, S.; Agostinelli, T.; Pires, E.; Hampton, M.; Nelson, J.; Macdonald, J. E. *Macromolecules* **2011**, *44*, 2725–2734.

28. Verploegen, E.; Mondal, R.; Bettinger, C. J.; Sok, S.; Toney, M. F.; Bao, Z. *Adv. Funct. Mater.* **2010**, *20*, 3519–3529.

29. Agostinelli, T.; Lilliu, S.; Labram, J. G.; Campoy-Quiles, M.; Hampton, M.; Pires, E.; Rawle, J.; Bikondoa, O.; Bradley, D. D. C.; Anthopoulos, T. D.; Nelson, J.; Macdonald, J. E. *Adv. Funct. Mater.* **2011**, *21*, 1701–1708.

30. Swan, P. *J. Polym. Sci.* **1962**, *56*, 403–407.

31. Flory, P. J. *Statistical Mechanics of Chain Molecules*; Interscience Publishers: New York, 1969.

32. Stehling, F.; Mandelkern, L. *Macromolecules* **1970**, *1*, 242–252.

33. Duzhko, V.; Semyonov, A.; Twieg, R.; Singer, K. *Phys. Rev. B* **2006**, *73*, 064201.

CHAPTER 3

PROBING THE MULTI-SCALE ORDERING IN SEMI-CRYSTALLINE P3HT

3.1 Introduction

From a morphological perspective, one of the most important structural parameters for P3HT is the degree of crystallinity, which influences the UV-Vis absorption, the miscibility with n-type [6,6]-phenyl-C61-butyric-acid-methyl-ester (PCBM) in the OPV active layer, charge transport properties and, therefore, the ultimate device performance.[1,2] Although the P3HT has been intensively researched, agreement on the degree of crystallinity of P3HT simply does not exist, due to the disordered nature of the crystals,[3,4] possible order within the amorphous phase, the interpretation of the results obtained with different techniques, and batch-to-batch variations in the polymers (for example regioregularity and molecular weight distribution). For thin film samples, due to the multiple uncertainties originating from the presence of surfaces and interfaces, indirect comparisons, rather than absolute numbers, are frequently reported by techniques including grazing-incidence x-ray diffraction (GIXD) and UV-Vis absorption.[5–7] While for bulk samples, WAXD,[3] density measurements,[8] DSC[9,10] and NMR[10–13] have been the most commonly used methods to determine the degree of crystallinity in P3HT. Pascui and co-workers, by discerning different conformational states of side chains belonging to order and disordered phases in ^{13}C solid-state NMR, concluded that the typical degrees of crystallinity range from 37 to 64% for low molecular weight P3HTs (Mn 5.2K and 7.9K, respectively).[13] Along with DSC results, the maximum heat of fusion for 100% crystalline rr-P3HT was estimated to be $\Delta H_\mathrm{m}^{\infty} \sim 37$ J/g, which has come under significant scrutiny subsequently. Nieuwendaal and co-workers suggested that, when the molecular

weight of P3HT is high (Form I), the side chains in both ordered and disordered regions appear to be highly dynamic and disordered, and, therefore, solid-state NMR could not be used to assess the degree of order.[11] These authors developed a spectral editing method in an attempt to separate the ordered from disordered fractions in a T1ρ-filtered ^{13}C CP/MAS NMR experiment, and determined that the degree of crystallinity was ~55% for a slow-dried P3HT (Mn~65K), which included contributions from chain segments that were locally ordered.[11] Balko and co-workers, using a WAXD method originally developed by Goppel,[14] reported degrees of crystallinity of P3HT on the order of 70~80% for a series of P3HTs having different molecular weights (ranging from 5K to 34K), and arrived at a modified ΔH_m^∞ of 33±3 J/g.[3] The degree of crystallinity was determined by evaluating the intensity at a specific scattering angle between the (100) and (200) reflections, where the additional background arising from incoherent scattering and diffuse scattering was neglected.[3] More recently, Snyder and co-workers reported good agreement between the DSC-derived and NMR-derived crystallinities and determined ΔH_m^∞ of 49±2 J/g, calculated by extrapolating the measured heat of fusion of P3HTs with different molecular weights to an infinite chain length.[10]

The degree of ordering in P3HT can be assessed by a variety of methods, however, care must be taken to note that each method is unique and what defines order or crystallinity depends, to some extent, on assumptions made in the analysis of the data. For example, the degrees of crystallinity of linear polyethylene obtained from density measurements are always found to be greater than those obtained by DSC. Manelkern concluded that the disparity arises from the presence of quasi-ordered interfacial region, which contributes to the density but is too weak to be counted in the measured heat of

fusion.[15] Similarly, the assignment of ^{13}C NMR peaks to crystalline chain segments is based on the segmental conformations or regularity of packing, which does not require long-range order as is required by WAXD.[16] As a result, the degree of crystallinity determined by NMR is usually greater than that determined by WAXD, owing to the additional inclusion of the short-range order in the form of crystalline-amorphous interphase, local rigid packing in the amorphous phase.[17] These disparities in the degrees of crystallinity reported for P3HT arises not only from the different methods used to determine the degree of crystallinity but, also, from differences in the molecular weight and molecular weight distributions of the polymers investigated and differences in the regio-regularities of the polymers.

Consequently, we undertook a study on the evaluation of ordering of one P3HT by a range of characterization methods. With WAXD, a very large q range was measured, taking into account the incoherent scattering and scattering from the amorphous component using a regio-random P3HT (rra-P3HT).[18] With solid-state NMR, we adopted Nieuwendaal's approach[11] and used a modified spectral editing method to interpret ^{13}C solid-state NMR.

In this Chapter, we present a quantitative study on the determination of the degree of crystallinity in bulk rr-P3HT by using a combination of WAXD, density measurements and ^{13}C solid-state NMR. By comparing the results from these different methods, the presence of an ordered amorphous component is evident, which is of significant importance in determining the transport characteristics of the polymer.

3.2 Experimental Section

3.2.1 Materials and Sample Preparations

P3HT with different molecular characteristics used in this study are summarized in Table 3.1. P3HT with Mn=34K (PDI=2.0, regioregularity ~93%) was purchased from Sigma-Aldrich (catalog-698989) and Mn=23K (PDI=2.0, regioregularity ~98%) was provided by Konarka Technologies. Regioregular P3HT with Mn=13K (PDI=1.2, regioregularity ~95%) was synthesized using GRIM method according to a published procedure.[19] The molecular weight of the polymer was controlled by a ratio of thiophene monomer and catalyst. Regiorandom P3HT (Mn=22k, Mw=72k, PDI=3.3, regioregularity ~57.7%) was purchased from Sigma-Aldrich (catalog-510823).

Table 3.1: Number-Average Molecular Weight (Mn), Polydispersity (PDI) and Regioregularity of P3HTs Investigated in This Study

	Mn	PDI	regioregularity
rr-P3HT	34K	2	93%
rr-P3HT	23K	2	98%
rr-P3HT	13K	1.2	95%
rra-P3HT	72K	3.3	57.7%

All materials were used as received. The molecular weight and PDI of each material were measured by a Polymer Laboratories PL-220 high temperature size exclusion chromatography equipped with a refractive index detector using trichlorobenzene as eluent and polystyrene as standards. Based on method described previously, the regioregularity of each material was calculated from ^{1}H-NMR spectrum acquired by a Bruker DPX-300 NMR spectrometer.[20]

For WAXD, density and NMR measurements, samples were prepared in the same manner with precisely-controlled thermal history. Powders of each material were sealed in a hermetical differential scanning calorimeter (DSC) pan to ensure good thermal conductivity, which was placed on a HSC302 heating stage constantly purged with N_2 gas. Subsequently, the heating stage was programmed to hold at a temperature well above the melting point of rr-P3HT, that is $260^{\circ}C$, for 1 hour to fully remove the thermal history of the original powders, and then slowly ramp down to room temperature at a rate of $0.2^{\circ}C/min$. It is our experience that the extremely slow cooling process allows rr-P3HT to fully order and yields reproducible samples, which is particularly crucial for density measurements since any potential voids formed in the bulk during rapid cooling will be detrimental to the accuracy of the measurements. Finally, the DSC pan was carefully opened and the bulk polymer sample was taken out of the pan as a piece of chunk with size comparable to the DSC pan.

3.2.2 Wide Angle X-ray Diffraction (WAXD) Measurements

WAXD measurements were performed on Beamline 7.3.3 at the Advanced Light Source (ALS) at the Lawrence Berkeley National Laboratory (LBNL). A transmission geometry was used. The wavelength of the x-rays is 1.240Å and the diffracted photons were collected by a two dimensional Pilatus 1M detector. A home-made helium box purged with He gas was used to reduce the unwanted air scattering and ensure clean background. Extra background was further avoided by attaching the bulk samples onto annular washers so that the bulk sample, without any additional container, is in the beam path between the exit of X-rays and detector. The sample-to-detector distance was ~207 mm. Corrections for sample absorption, thickness, normalization and polarization were

carried out for the diffraction intensities as explained in Figure 3.1 and Equation 3-1, where I_1ef is the intensity of the direct beam after passing empty field (i.e. no sample in the beam path) read by a photodiode, I_1 is the intensity of the direct beam after passing the sample read by a photodiode, EF2D is the diffraction intensity collected by the 2D detector with empty field and Sa2D is the diffraction intensity of the sample collected by the 2D detector, t is the sample thickness. As shown in Figure 3.2, it is then followed by rescaling the corrected intensity to absolute scale with the assistance of measuring a pre-calibrated glassy carbon sample under the same condition and obtaining the correction factor Cf as given in Equation 3-1.[21]
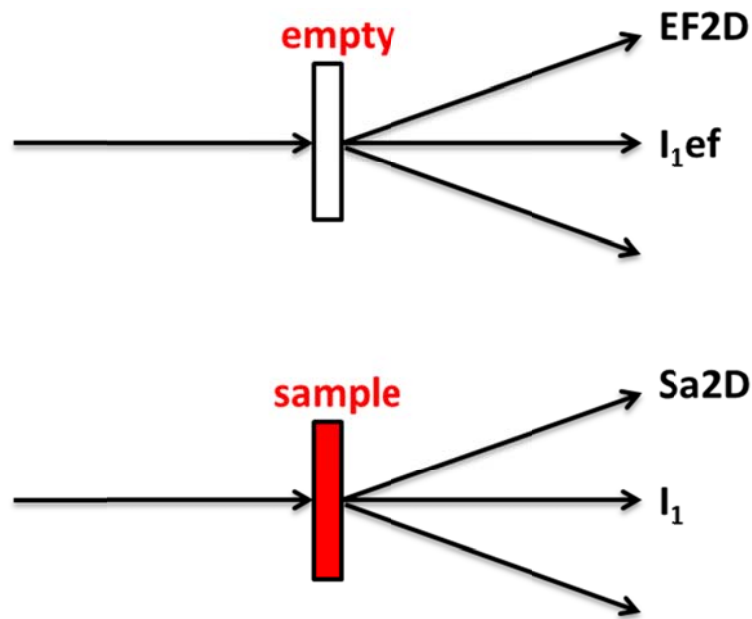
Figure 3.1: Schematic illustrating the empty field without polymer sample in the beam path (top) and sample field with polymer sample in the beam path. The empty field measurement is used to correct for the sample absorption and parasitic scattering.
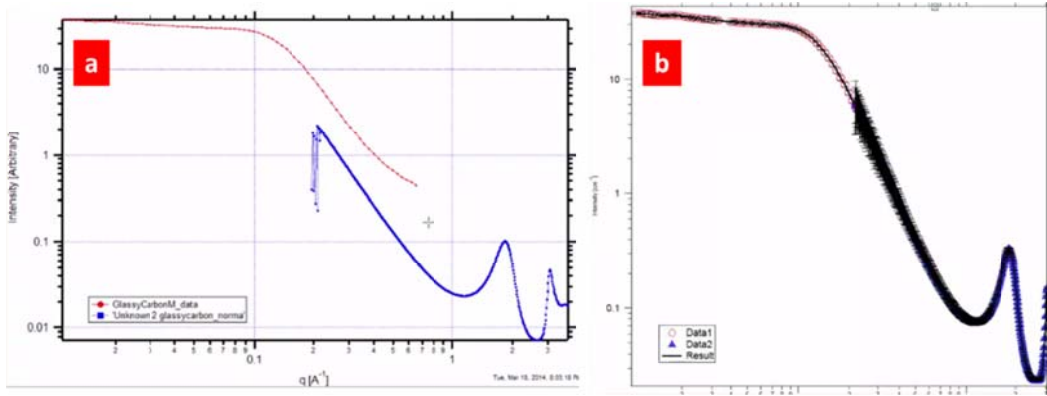
Figure 3.2: (a) Experimentally measured and background corrected scattering profile I(q) vs q for the pre-calibrated glassy carbons sample in absolute scale (red) and in arbitrary scale (blue); (b) the correction factor Cf is determined by rescaling the arbitrary intensity profile to match the absolute intensity profile.

$$I_{absolute} = Cf * \frac{1}{t} * \frac{1}{I_1} * (Sa2D - \frac{I_1}{I_1 ef} EF2D)$$

Eq. 3-1

The thickness of each sample in centimeter was determined by Equation 3-2, where I_0/I is the transmission of the sample and μ is the linear absorption coefficient. μ is given by multiplying the linear absorption coefficient μ/ρ by the density of the sample, ρ, determined from density gradient column measurements (see 3.2.3). For P3HT with known composition ($C_{10}H_{14}S$), the linear absorption coefficient in units of cm^2/g can be calculated by Equation 3-3, in which w_i and $(\mu/\rho)_i$ are the weight fraction and mass absorption coefficient, respectively, of element i. For common elements at specific x-ray wavelengths, $(\mu/\rho)_i$ are provided in the cited database.[22]

$$t = \frac{ln\frac{I_0}{I}}{\mu}$$

Eq. 3-2

$$\frac{\mu}{\rho} = \sum_i \omega_i \left(\frac{\mu}{\rho}\right)_i$$

Eq. 3-3

Subsequent to the conversion of the experimental data to absolute scale (electron units), the subtraction of background arising from incoherent scattering was performed. The incoherent scattering of P3HT in electron units was calculated by Equation 3-4, where N_i and I_i are the number and incoherent scattering intensity in electron units of atom I, respectively, and R is Breit-Dirac recoil factor given by Equation 3-5. The incoherent scattering profile of specific element is provided in the literature.[23] In Equation 3-5, h is Planck's constant, m is the mass of the electron, c is the velocity of light, λ is the wavelength of x-rays, and θ is the scattering angle.

$$I_{inc} = R \times \left(\frac{\sum N_i I_i}{\sum N_i}\right)$$

Eq. 3-4

$$R = \left(1 + \frac{2h}{mc\lambda}\sin^2\theta\right)^{-3}$$

Eq. 3-5
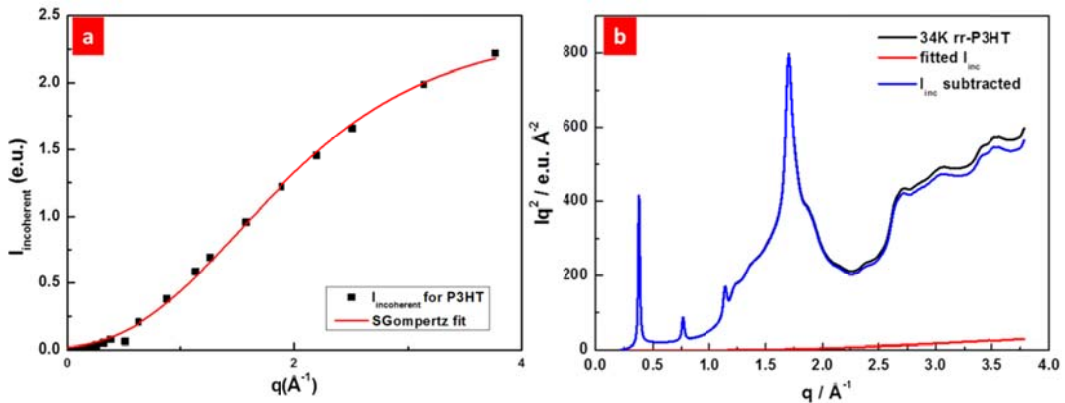
Figure 3.3: (a) The incoherent scattering profile of incoherent scattering of P3HT with chemical formula of $(C_{10}H_{14}S)_n$. The red curve is a fit to the incoherent scattering; (b) Iq^2 vs q plot for incoherent scattering intensity (red), 34K rr-P3HT without the subtraction of incoherent scattering (black), and with the subtraction of incoherent scattering. (blue).

The fitting of the incoherent scattering of P3HT and an exemplary subtraction of the incoherent scattering from the experimental data are shown in Figure 3.3(a) and (b), respectively.

3.2.3 Density Gradient Column Measurements

A saturated sodium chloride (NaCl) solution ($\rho \sim 1.2$ g/cm^3) and deionized water ($\rho \sim 1.0$ g/cm^3) were used as the two miscible liquids with higher and lower density, respectively. The linear gradient in a column (American Density Materials, Inc) was established by a sequential mixing of saturated NaCl solution into deionized water and was maintained at constant temperature of 25°C by water bath during the course of measurement. Density floats of precisely known densities (American Density Materials, Inc) were wet with water and then released into the column. As exemplarily shown in Figure 3.4, a linear calibration curve of the gradient was obtained by plotting the densities of floats against their positional readings in the column. Both rr- and rra-P3HT specimens were thermally treated with the same slow cooling recipe as in the WAXD measurements. Subsequently, a chunk of the polymer specimen was first wet with 5mM sodium dodecyl sulfate (SDS) solution and carefully introduced into the column from the top of the gradient so that no air bubbles were adhered to the sample. After the specimen was stabilized in the column, the position was read and consequently the density of the specimen was determined from the calibration curve. In general, four to five readings were recorded and averaged for each measurement.
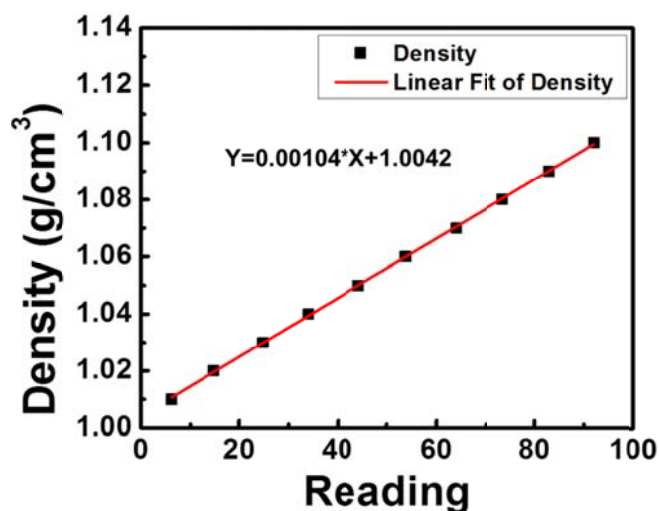
Figure 3.4: Typical linear calibration curve at 25°C used for the determination of sample densities from the positional reading in the column. The black square points are from the reading of density floats with precisely-known densities, showing good linear density gradient in the column. The red line is a linear fit with inset function.

3.2.3 ^{13}C Solid-State Nuclear Magnetic Resonance Measurements

All NMR experiments were conducted on a Bruker DSX300 spectrometer, operating at a ^{1}H frequency of 300.12 MHz and ^{13}C frequency of 75.47 MHz, in 4mm CP/MAS probes. The pulse sequence was a 90° pulse followed by an optional ^{1}H spin lock pulse before CP and high-power ^{1}H decoupled ^{13}C detection. The chemical shift was externally referenced by polydimethylsiloxane peak at 1.4 ppm. For crystallinity determination, 7 ms of spin lock with a field strength of 60 kHz was used. A RAMP-CP scheme was used for cross polarization, which has been shown to generate a more quantitative representation of non-protonated carbons.[24] The ramp size was 5 kHz and the contact time was 3 ms. The recycle delay, decoupling field, and spinning speed were 1.2 s, 65 kHz and 5 kHz, respectively.

3.3 Results and Discussion

3.3.1 Crystallinity Determined by WAXD Approach

Detailed reviews of the theoretical foundation and mathematical derivation of various WAXD-based approaches for the determination of the degree of crystallinity in polymers have been published.[3,14,18] The success of these treatments, in particular those put forth by Ruland and Goppel, rely on an accurate assessment of the contributions to the diffraction from incoherent scattering, $I_{inc}(q)$, the crystalline component, $I_{cr}(q)$, and the amorphous component, $I_{am}(q)$, to the overall diffracted intensity $I(q)$. Several important issues must be addressed. $I_{inc}(q)$, which contains no structural information must be removed from the measured data before considering the coherent scattering from the structure in the material. Since the $I_{inc}(q)$ increases as a function of q, this procedure is particularly important for high q data. The incoherent scattering for P3HT in electron units can be calculated as described in 3.2.2. To subtract the calculated $I_{inc}(q)$ from the experimentally measured data, the measured diffraction intensity is converted to an absolute scale. An effective means to describe $I_{am}(q)$ for P3HT is critical. Quenching from the melt has had little success, since P3HT crystallizes rapidly. Since the diffraction contains reflections from the inter-thiophene chain and the inter-alkyl side chain separation distances, which have different thermal expansion coefficients, extrapolation of melt data to room temperature, for example, cannot be done without making numerous assumptions. Also, a thorough subtraction of the background arising from the heating compartment (i.e. aluminum pan) is not practically straightforward.[25] Therefore, we assumed that $I_{am}(q)$ was described by the scattering from rra-P3HT. While this route assumes the chain configuration and packing density of the rra-P3HT is identical to

amorphous rr-P3HT, which may not be correct due to the local conformational differences between rra-P3HT and rr-P3HT, it is the route where the fewest number of assumptions are made and where the least amount of manipulation of the experimental data is required.

Disorder is common in polymer crystals, wherein the deviations of the lattice atoms from their equilibrium positions lead to a loss of intensity from the crystalline phase.[18] Consequently, in addition to the intensity under the sharp Bragg peaks, $I_{cr}(q)$ includes a second component, namely the diffuse scattering, which may overlap $I_{am}(q)$. This disordering within the crystalline phase is caused by thermal vibrations and lattice imperfections, and will lead to an underestimation of degree of crystallinity if not properly taken into account. The degree of crystallinity can be calculated from Equation 3-6 with the introduction of a correction factor for the disorder in the crystalline phase, K, which is defined in Equation 3-7, where q is the scattering vector, I(q) is the measured coherent scattering, f is the weighted mean square atomic form factor of the polymer, $e^{-kq2/4\pi2}$ is an isotropic Debye-Waller factor describing the effect of thermal motion and lattice imperfection.

$$X_c = K(q_1, q_2, k, \langle f^2 \rangle) \times \frac{\int_{q_1}^{q_2} q^2 I_{cr}(q) \, dq}{\int_{q_1}^{q_2} q^2 I(q) \, dq}$$

<div align="right">Eq. 3-6</div>

$$K = \frac{\int_{q_1}^{q_2} q^2 \langle f^2 \rangle \, dq}{\int_{q_1}^{q_2} q^2 \langle f^2 \rangle e^{-\frac{kq^2}{4\pi^2}} \, dq}$$

<div align="right">Eq. 3-7</div>

Three semi-crystalline rr-P3HT samples with number-average molecular weights of 13K, 23K and 34K, and a rra-P3HT sample were used in this study. The characteristics of the polymers are shown in Table 3.1.

All samples were subject to the same thermal history prior to each WAXD measurement, namely cooling from 260°C to room temperature at a rate of 0.2°C/min. This slow cooling process maximizes the degree of ordering within the semi-crystalline samples. For each measurement, the resulting diffraction intensity was normalized and corrected for polarization, absorption, sample thickness and parasitic scattering, followed by conversion to absolute units using a pre-calibrated glassy carbon sample.[21] Subsequently, the calculated incoherent scattering of P3HT was subtracted from the experimental data on an absolute unit scale. (see 3.2.2) The diffraction intensity I(q) in electron units for all the samples is plotted against q in Figure 3.5 over a scattering vector range from ~0.2 Å^{-1} to ~3.8 Å^{-1}.

Sharp reflections indicative of semi-crystalline order were evident in all regioregular samples with the smallest molecular weight sample exhibiting more small crystalline peaks.[9] It is interesting to note that an additional peak located at q~2.68 Å^{-1} is present in all the regioregular samples, which can be important for the determination of crystallinity. Most diffraction profiles reported to date do not report this reflection due to the limited q range measured. In contrast to the multiple sharp Bragg reflections seen in the semi-crystalline sample, the rra-P3HT sample yielded three broad amorphous halos corresponding to d-spacings of 15.7Å, 4.3Å and 2Å, which are attributed to the averaged separation distance between thiophene backbones, the average separation distance

between adjacent alky chains, and thiophene ring separation distance along the backbone, respectively.[25,26]
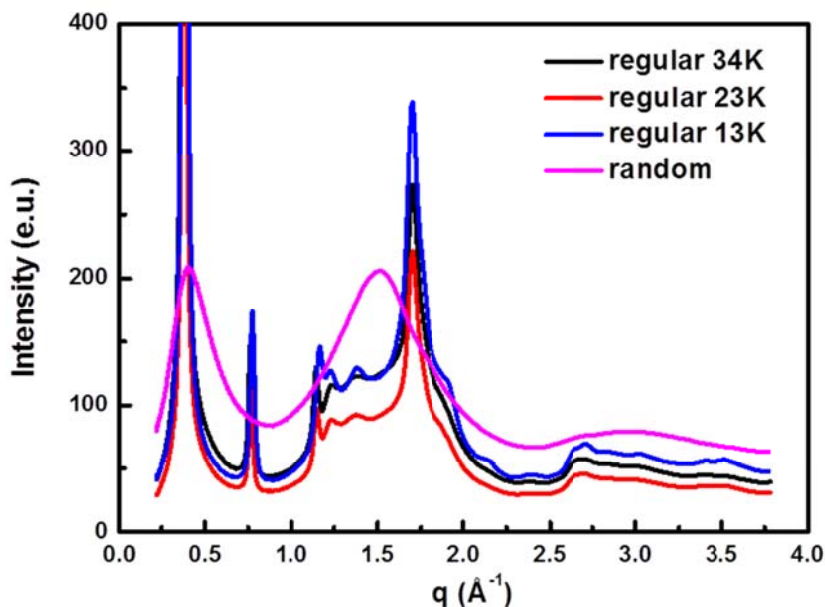
Figure 3.5: I(q) vs q plot for 34K (black), 23K (red) and 13K (blue) rr-P3HTs and rra-P3HT (pink) measured by WAXD. The diffraction intensity is normalized and corrected for polarization, absorption, sample thickness and parasitic scattering, followed by being rescaled to absolute units with the assistance of a pre-calibrated glassy carbon sample.

The overall shapes and locations of the three amorphous halos match well with the intense Bragg peaks in the semi-crystalline samples, suggesting that rra-P3HT may be a good representation of the amorphous phase in rr-P3HT. It is demonstrated in 2.3.3 that rra-P3HT, which is chemically similar to its regioregular counterpart, appeared to be amorphous in WAXD, and, hence, can be used to represent the amorphous phase in the regioregular semi-crystalline sample. Indeed, as shown in Figure 3.6, similar amorphous halo features are observed for rr-P3HT and rra-P3HT at 250°C, which is well above the melting point of rr-P3HT.
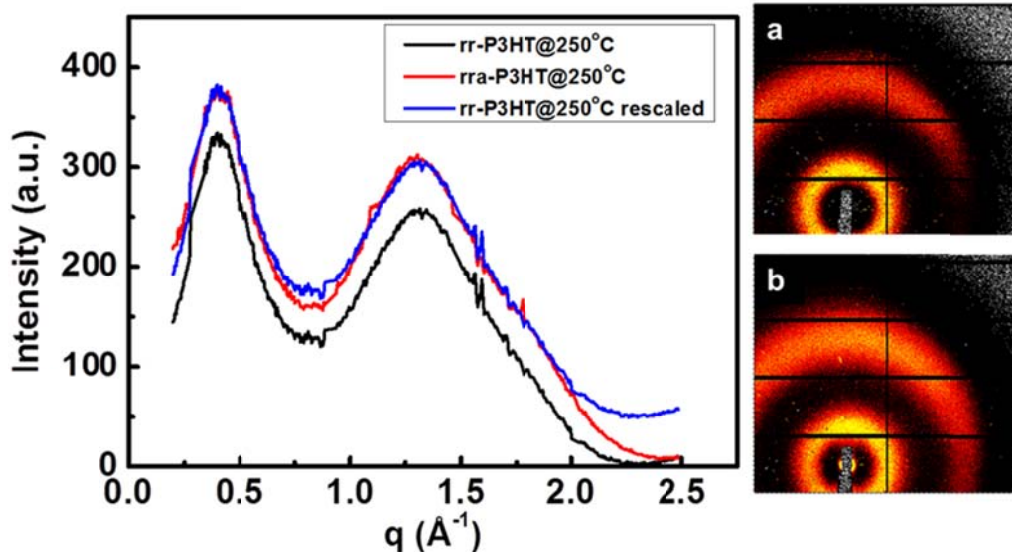
Figure 3.6: I(q) vs q profiles at $250^{\circ}C$ for rr-P3HT (black), rra-P3HT (red) and rescaled rr-P3HT (blue); and wide angle diffraction patterns of amorphous halos at $250^{\circ}C$ for: (a) rr-P3HT; (b) rra-P3HT.

After rescaling the diffraction intensity of rr-P3HT, the diffraction profile of rra-P3HT is seen to overlap with the rr-P3HT diffraction over a broad q range, indicating that rra-P3HT is, in fact, a good approximation for the amorphous rr-P3HT and that $I_{rra}(q) \sim I_{am}(q)$ at room temperature. To facilitate the assessment of respective contribution from $I_{cr}(q)$ and $I_{am}(q)$, to the overall diffraction, $I_{rra}(q)*q^2$ was rescaled to maximize the overlap with the $I(q)*q^2$ of rr-P3HT and plotted together with the rr-P3HT sample as shown in Figure 3.7. As can be seen the diffraction from rra-P3HT smoothly intersects the continuously varying curvature of the rr-P3HT sample and the three amorphous halos of rra-P3HT provide a good approximation of $I_{am}(q)$. The $I_{cr}(q)$, in Equation 3-6, is given by the difference between the rescaled $I_{rra}(q)$ and I(q), shown as the shaded area in Figure 3.7.
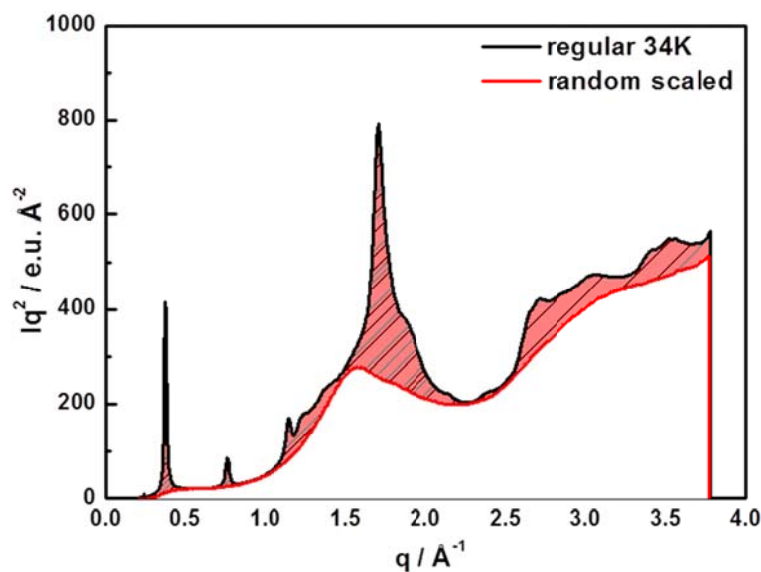
Figure 3.7: $I(q)*q^2$ vs q plot for 34K P3HT (black) and rescaled rra-P3HT (red) over a large q range.

The large experimental q range measured captures all the features of the diffraction from rr-P3HT and, therefore, the degree of crystallinity can be measured with reasonable accuracy by the integrals in Equation 3-6.

Following the Ruland's method, the degree of crystallinity was calculated by Equation 3-6 with the parameter k (in the term of disorder correction factor K) and upper-limit of the intergral, q_2, being varied, while the lower-limit q_1 being fixed. Ruland argues that the degree of crystallinity of the sample should be independent of the choice of q_2 for a given k.[18] Consequently, the best value of crystallinity and the k parameter can be determined simultaneously by choosing the data set where the variation of the crystallinity is the least as q range varies. For example, in Table 3.2 for the 34K sample, when k =6, the standard deviation of the calculated degrees of crystallinity across different q ranges is the smallest and, therefore, the mean value of 44% was determined for this sample.

Table 3.2: The Degree of Crystallinity and its Standard Deviation of the 34K Sample as the k Value is Varied From 0 to 7 and the Upper-Limit of the Intergral q^2 is Varied From 1 to 3.78Å^{-1}.

rr-P3HT 34K						
q interval /Å^{-1}	k/Å²					
	0	3	4	5	6	7
0.22-1	0.45	0.47	0.47	0.48	0.49	0.50
0.22-2	0.35	0.42	0.44	0.46	0.49	0.52
0.22-2.5	0.28	0.36	0.39	0.42	0.45	0.49
0.22-3.25	0.22	0.32	0.36	0.41	0.45	0.50
0.22-3.78	0.19	0.32	0.37	0.43	0.49	0.55
mean	0.30	0.38	0.41	0.44	0.47	0.51
Std Dev	0.092	0.057	0.043	0.029	0.018	0.022

The degrees of crystallinity for the three regioregular samples are summarized in Table 3.3 together with the respective k values, from which the average root mean square displacements of atoms, $<\mu^2>^{0.5}$, from their positions in a crystalline lattice were also calculated by the following expression: $k = 4/3 \times \pi^2 \times <\mu^2>$.[27]

Table 3.3: The Degree of Crystallinity Determined by WAXD Method, the Disorder Parameter k (Equation 3-6), the Average Root Mean Square Displacements of Atoms $<\mu^2>^{0.5}$ for Different Regioregular P3HTs.

P3HT	WAXD Xc(%)	k/Å²	$<\mu^2>^{1/2}$/Å
13K regular	56%	4	0.55
23K regular	49%	5	0.62
34K regular	47%	6	0.68

The absolute degree of crystallinity is found to decrease as molecular weight increases: 56% for the 13K sample, 49% for the 23K sample and 47% for the 34K

sample. This overall trend is consistent with previous results: the 13K sample (determined by SEC), below the chain folding onset, forms extended chain crystal featuring highly crystalline lamellae;[3,10,28] while for the 34K sample, both chain folding, broader PDI and lower regioregularity can lead to the observed reduction in the degree of crystallinity.[29] We note that the highest degree of crystallinity of 56% in the 13K sample is considerably smaller than 70~80% reported by Balko et al.,[3] suggesting that the absolute value is highly dependent on the material properties such as PDI, regioregularity and molecular weight.[3,29]

The disorder parameter k is found to be in the range of 4~6 for the three different samples, which corresponds to $<\mu^2>^{0.5}$ range of 0.55~0.68Å. In addition, the most pronounced disordering effect (k=6) or the displacements of atoms in the crystal lattice ($<\mu^2>^{0.5}$=0.68Å) was found in the 34K sample with the highest molecular weight. Given that the materials also differ in PDI and regioregularities, both the low regioregularity of 93% and high molecular weight of 34K may contribute to the disorder within crystals by having T-T regio-defects incorporated in the lattice and large kinetic constraints during crystallization, respectively.[29] It is interesting to note that an increase of the disorder in the crystalline packing has been directly observed by Brinkamann et al. in high molecular weight P3HT (Mw>18.8K) by high-resolution TEM,[4] the origin of which was attributed to the stress on chain packing induced by chain folding. This is in agreement with the increasing trend of k with molecular weight in our WAXD analysis but we do not have direct evidence of chain folding. Furthermore, the determined k value is larger in comparison with that found for polythiophene (PT, k=3Å^2),[27] but, smaller than 7~15Å^2 which was derived by Balko et al. on a series of P3HT with different molecular weights.[3]

The hexyl side chains attached to the polythiophene backbones are found to be highly dynamic by solid-state NMR, as evidenced by 13C T_1 relaxation times. This is, more than likely, responsible for the disorder difference seen between PT and P3HT. Considering the difference in the molecular characteristics between our materials and the ones used in the study of Balko et al., we assigned the low k parameters in our materials to the slow-cooling thermal history, which is expected to lead to more perfect crystals with a higher degree of crystallinity.

3.3.2 Crystallinity Determined by Density Approach

Another commonly employed physical method to determine the degree of crystallinity is mass density, which yields either volume fraction (ϕ_c) or mass fraction (x_c) of crystallinity as given by Equations 1-3 and 1-4, where ρ, ρ_c and ρ_a are the densities of semi-crystalline, completely crystalline and completely amorphous rr-P3HT, respectively.

As seen, independent knowledge of the densities of completely crystalline, ρ_c, and completely amorphous, ρ_a, are necessary to determine ϕ_c and x_c. Using the structural information from the unit cell determined by electron diffraction,[30] the density of a 100% crystalline rr-P3HT is calculated to be ~1.132 g/cm^3. Due to the rapid kinetics of crystallization of rr-P3HT, we were not able to prepare a rr-P3HT sample that is fully amorphous. Instead, rra-P3HT, was used to approximate the amorphous form of rr-P3HT. A density gradient column was used to measure the densities of rr- and rra-P3HT specimens having the same thermal history as the WAXD samples. The densities of rra- and rr-P3HTs were determined and are tabulated in Table 3.4.

As expected, the mass density of the rra-P3HT, 1.090±0.001 g/cm^3, is smaller than all three regioregular samples, due to the lack of long-range 3-D ordered packing. However, Lee and co-workers have recently reported the density of rra-P3HT, 1.111 g/cm^3, measured by gas pycnometry,[8] which is significantly larger than all of our regioregular and regiorandom samples. The origin of the discrepancy is not understood. Assuming that the density of rra-P3HT is equal to ρ_a, the degrees of crystallinity of rr-P3HT with different molecular weights were calculated using Equation 1-4 and given in Table 3.4. Note that the density-derived crystallinity results are considerably smaller than those determined by WAXD. This discrepancy, at least in part, stems from the assumption that the density of rra-P3HT is equal to that of the amorphous phase in rr-P3HT. Even though the diffraction of rra-P3HT only gives rise to diffuse halos, the high density of 1.09 g/cm^3 suggests that the packing of the chain segments may not be totally disordered. This raises the question as to whether the rra-P3HT, which shows no evidence of ordering in DSC, WAXD and UV-Vis measurements, is truly amorphous. The issue will be discussed in 3.3.3. Nevertheless, the density results show that the degree of crystallinity decreases as the molecular weight of the sample increases, which is in qualitative agreement with the WAXD results.

Table 3.4: The Mass Densities of rr-P3HTs and rra-P3HT Measured by Density Gradient Column and the Corresponding Degree of Crystallinity as Calculated from Equation 1-4.

P3HT	Density (g/cm³)	Density Xc(%)
13K regular	1.107±0.001	41%
23K regular	1.099±0.003	22%
34K regular	1.097±0.001	17%
random	1.090±0.001	0%

3.3.3 Crystallinity Determined by ^{13}C Solid-State NMR Approach

In general, WAXD is sensitive to the long-range order present in the semi-crystalline polymers, while solid-state NMR is sensitive to semi-crystalline ordering on a short-range scale. The NMR technique usually differentiates phase structures in polymers on the basis of chain conformations, local packing arrangements, and molecular dynamics, often quantitatively. Consequently, NMR can be used to determine the fraction of chain segments that are ordered within a crystalline, ordered, but surrounded by disordered segments, or fully disordered.

The degree of crystallinity of rr-P3HT can be determined by the solid-state ^{13}C NMR technique. Figure 3.8 shows the CP/MAS ^{13}C NMR spectrum of rr-P3HT in the solid state and single-pulse, ^{1}H decoupled ^{13}C spectrum of the same sample dissolved in CDCl$_3$. Carbons labeled C1 to C6 are from the hexyl side chain while those labeled C7 to C10 are from the thiophene ring.
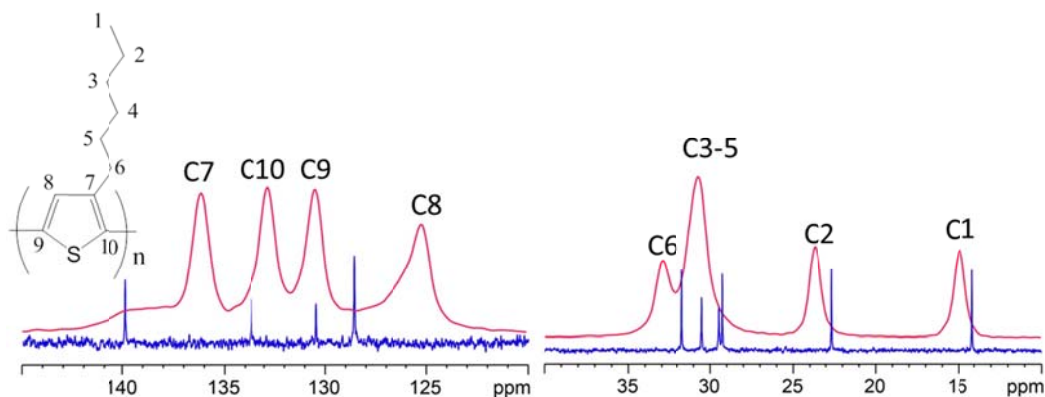
Figure 3.8: CP/MAS ^{13}C NMR spectrum of 34K rr-P3HT in the solid state (red) and single-pulse, ^{1}H decoupled ^{13}C spectrum of the same sample dissolved in CDCl$_3$(blue). The carbons are labeled on the spectrum according to the inset schematic.

In the CP/MAS spectrum, the group of peaks between 120 and 144 ppm includes four sharp peaks riding on top of a broad shoulder. The sharp peaks are assigned to the

four thiophene carbons in the crystalline state, and the broad shoulder to those in the amorphous or disordered state. Comparing the solid- and solution-state spectra, Figure 3.8 shows large up-field shifts for C7 and C8 in the crystalline state, which are due to the magnetic field generated by ring current in the neighboring thiophene rings as a result of $\pi-\pi$ stacking, termed aggregation shifts or nucleus-independent chemical shifts (NICS).[12,31,32] For the samples with higher regioregularity or crystallized with conditions favoring higher crystallinity (such as slow cooling from the melt), the four peaks are taller and the broad background is relatively lower, further confirming the assignment of the sharp peaks and the broad background to crystalline and amorphous region, respectively. We note that the resonance peaks of C9 and C10 only exhibit small aggregation shifts. While aggregation shift of the only proton on the thiophene ring has been used to calculate crystallinity and studied for the geometry of stacking,[12] [13]C aggregation shifts have received little attention.

Nieuwendaal et al. reported that the signals from ordered domains exhibit longer $T_{1\rho}$ than those from the disordered region, which allows a spectral editing method to quantify crystallinity.[11] We confirm similar findings, and employ the same 7-ms spin-lock filter that results in different extent of $T_{1\rho}$ relaxation for the crystalline and amorphous signals. We developed the following spectral editing method:

1. Accurately calibrate peak position for both the spectra with (A in Figure 3.9) and without (B in Figure 3.9) $T_{1\rho}$ filter, which would minimize the extent of dispersiveness on the difference spectrum. We found that even experiments conducted back to back can have 1-3 Hz shift, which for high-crystallinity

samples is enough to generate quite sizable dispersive signal on the difference spectrum.

2. Subtract spectrum B from spectrum A, with the former scaled such that the difference forms a pattern that is free of crystalline signals. The difference is the amorphous pattern (C in Figure 3.9).

3. Subtract C from A, with the former scaled such that its average height at the shoulder between 138 and 139.5 ppm is the same as that in the latter. The difference spectrum is the pure crystalline pattern (D in Figure 3.9).

4. The area ratio D/A yields the degree of crystallinity.

We find that this method minimizes the dispersiveness of the amorphous signal shape when subtracting two sets of tall and sharp peaks, thus involving less subjectivity compared to what was reported by Nieuwendaal et al.[11]
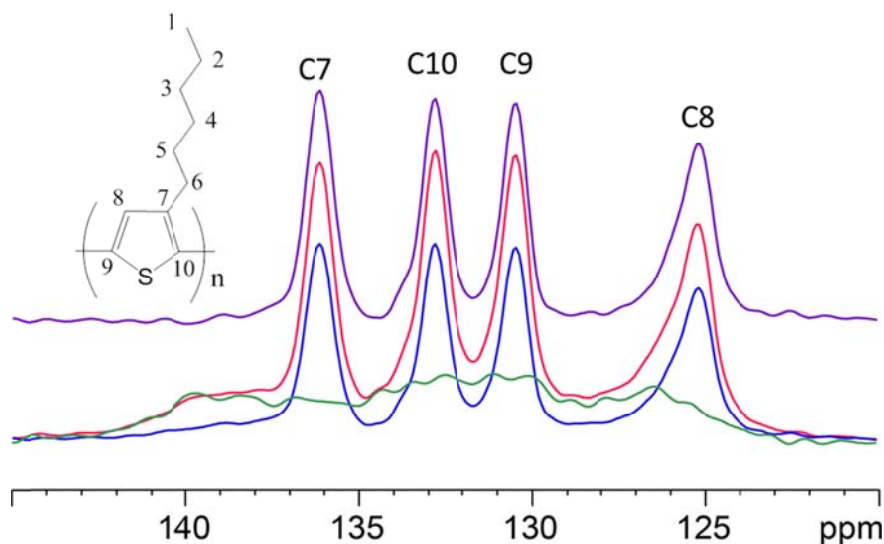
Figure 3.9: (A): CP (Red); (B): CP with 7ms spin lock (blue); (C): difference of A and B, with B scaled according to step 2 in the spectral editing procedure (green). (D): Difference of A and C, with C scaled according to step 3 in the spectral editing procedure (purple).

The results for the three semi-crystalline rr-P3HT samples with identical slow-cooling thermal history are summarized in Table 3.5, along with the WAXD and density results in the same table.

Table 3.5: The Degrees of Crystallinity Determined By Density, Wide-Angle X-ray Diffraction and Solid-State ^{13}C NMR methods.

P3HT	Density Xc(%)	WAXD Xc(%)	NMR Xc(%)
regular 13K	41%	56%	66%
regular 23K	22%	49%	60%
regular 34K	17%	47%	56%

In good qualitative agreement with WAXD and density results, the degree of crystallinity decreases with increasing molecular weight, possibly due to the broad PDI and multiple kinetic constraints (i.e. chain folding, chain entanglements) in the high molecular weight materials during crystallization.[29] It is interesting to note that the NMR degree of crystallinity is consistently ~10% greater than those determined by WAXD for all three materials, which we attribute to a local short-range ordered region within the amorphous phase.

To understand the high density of rra-P3HT, ^{13}C NMR spectra were acquired both in the solid- and solution state and the peak arising from C8 is specifically shown in Figure 3.10.
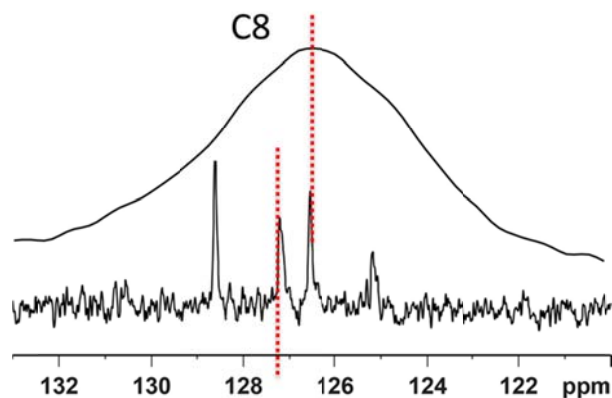
Figure 3.10: CP/MAS ^{13}C NMR spectrum of rra-P3HT in the solid state (top) and single-pulse, ^{1}H decoupled ^{13}C spectrum of the same sample dissolved in CDCl$_3$(bottom). Dotted lines are the averaged chemical shifts.

Since the chain segments in rra-P3HT may contain four possible regioisomers, each carbon on the thiophene ring experiences a variety of chemical environments, resulting in multiple chemical shifts. Therefore, a DEPT (Distortionless Enhancement by Polarization Transfer) technique was used to suppress the signals from unprotonated carbons for the solution-state P3HT and show only the four peaks associated with the protonated C8. The solid-state NMR spectrum of rra-P3HT for the thiophene ring carbons is also quite complex, so a short CP time of 60 μs was applied to suppress the non-protonated ^{13}C peaks. Figure 3.10 shows that the solid-state C8 peak (at 126.5 ppm) shifts up-field by ca. 2 ppm compared to the regioregular (HT) triad (at 128.6 ppm) and by 0.7 ppm compared to the center-of-mass average peak position in the liquid state (at 127.2 ppm). This shift most likely can be attributed to an aggregation shift due to a weak order. This would suggest that the rra-P3HT chains in the solid state are not packed in the same way as they are in a truly amorphous state in the solution. Considering the high density of the rra-P3HT, it is speculated that ordered packing at local scale exists in the rra-P3HT, which is very likely invisible and "amorphous" to WAXD measurements. Two

64

factors could contribute to this partial ordering. First, the rra-P3HT sample is not completely random, which can be seen from the solution-state NMR spectrum in Figure 3.10 in which the regioregular triad at 128.6 ppm is the tallest peak. Second, even in a regiorandom sample, there may exist longer regioregular segments that can self-assemble and give rise to short-range order. The signatures of local ordering in rra-P3HT were also found in our recent photophysical characterizations of rra-P3HT thin films. (data not shown)

It is to be noted that CP is fundamentally not a quantitative NMR technique. Fortunately, several structural aspects of P3HT make CP a reasonably quantitative method for crystallinity determination: (1) the molecular dynamics in both crystalline and amorphous phases are very similar, as evidenced by a ^{1}H wideline spectrum that can be fitted by a single-component Gaussian with high fidelity (adjusted $R^{2}= 0.999$). The spectrum has a full-width-at-half-maximum (FWHM) of 33 kHz, indicating efficient cross polarization for both phases. (2) The ^{13}C MAS side chain peak shapes are single component, and all of their ^{13}C T1 relaxation curves are single-exponential, further suggesting very similar molecular dynamics in both phases. (3) The T1ρ of both crystalline and amorphous phases are relatively long (approximately 15 ms and 5 ms, respectively). During the 3-ms contact time, most of the non-protonated signals are excited while the amorphous signals suffer minimal loss due to T1ρ relaxation (most of the excited amorphous signals are generated during the latter part of the contact time). This makes the CP experiments a semi-quantitative experiment for P3HT.

At spinning speed of 5 kHz, signals in the spinning sidebands represent ca. 20% of the total area, so the contribution of spinning sidebands must be considered. We find

that the amorphous-to-crystalline signal intensity ratio in the first-order spinning sidebands are roughly the same as that in the centerband. This means that the chemical shift anisotropy for crystalline and amorphous signals is about the same, which suggests that we can only perform spectral editing only on the centerband in the crystallinity calculation.

3.3.4 Ramifications of the Results From Different Techniques

Although the decrease in the degree of crystallinity with increasing molecular weight reported here is seen for all the WAXD, density, NMR and DSC measurements, an unambiguous explanation is not readily available since the materials differ not only in molecular weights but also in regioregularity and PDI. It is of most importance to compare the results from exactly the same material to gain insight into the morphology. In comparison with WAXD and NMR results, density method tends to underestimate the amount of ordering, which is possibly linked to the existence of short-range ordered packing in rra-P3HT resulting in a higher mass density than that of a fully amorphous P3HT; whereas the WAXD, after compensations for the disordering effect are made, yields the fraction of crystalline grains persisting 3-dimensionally in long range. For NMR, not only do the long-range ordered grains as seen ordered by WAXD contribute to the ordered resonance peak, the short-range ordering, for instance, (i) the intermediate phase between the crystalline grain and amorphous phase which is reported for polyethylene,[15,33,34] (ii) the locally ordered chain stacks in the amorphous phase which may share the same origin with the local order in rra-P3HT, or (iii) possible tie chains/grains connecting neighboring crystal grains, are all visible and considered as ordered fraction of the semi-crystalline rr-P3HT. Consequently, the quantitative

comparison of the degree of crystallinity at different length scales forces us to conclude that, instead of a classic two-phase picture depicting crystalline and amorphous phases, the amorphous phase is not completely disordered but, rather, there is a local, short-range ordering in the amorphous phase. These ordered areas cannot be considered as a distinct phase, since there is no evidence of this in the scattering and diffraction results. Consequently, these ordered areas can be several P3HT chains that assume a π-π stacking packing structure similar to that seen in the crystals. A rough schematic illustrating the semi-crystalline morphology is provided in Figure 3.11.
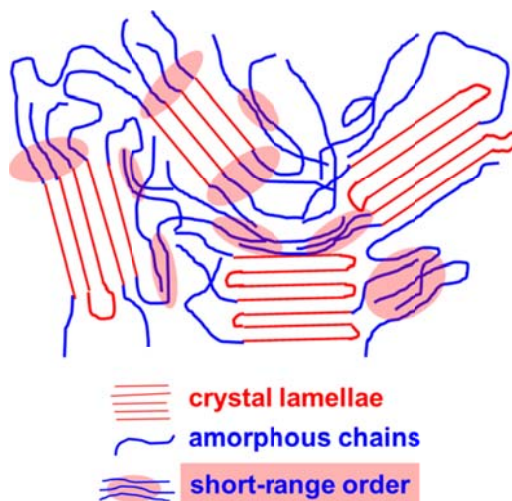
Figure 3.11: Schematics illustrating the semi-crystalline morphology in rr-P3HT comprising crystalline lamellae, amorphous phase, and a local short-range ordered phase.

Notably, Mandelkern et al. have measured and compared the degrees of crystallinity determined by density measurement and DSC for different types of polyethylene, and it has been observed that density measurement yields greater crystallinity than DSC, which is attributed to the inclusion of the crystalline-amorphous interfacial contribution to the measured density.[15] Despite that P3HT and PE are distinctly different from various molecular aspects, the interfacial region identified in PE

may also apply to the case of rr-P3HT, which, however, cannot preclude the possibilities of other types of short-range ordering as postulated above. It is also expected that the local short-range order would have a positive impact on the charge transport characteristics in P3HT at a macroscopic scale. Detailed investigation on the correlation between the hole transport and the local short-range ordering is summarized in Chapter 4.

The interfacial regions between the crystalline and amorphous phases are counted as ordered fraction in density measurements, which suggests that the density-determined crystallinity is most likely consistent with that obtained by NMR, representing an upper-bound of the ordering in the material. Thus, by equating the NMR-determined crystallinity to density-determined one, the density of a fully amorphous sample, ρ_a, was calculated by rearranging Equation 1-4 for the three P3HT samples. The results (1.061 g/cm^3 for 13K, 1.053 g/cm^3 for 23K, 1.055 g/cm^3 for 34K), again, significantly deviated from the 1.094 g/cm^3 reported by Lee et al.[8] by extrapolating density data to zero heat of fusion. As discussed above, the density measurements include the short-range order that is not typically captured by the DSC measurements,[15] due likely to the fact that those short-range ordered phases melt at a much lower temperature than the melting point and are gradually destroyed during the heating ramp with negligible heat of fusion. Therefore, the correlation between the density results and the heat of fusion is questionable. Additionally, according to Lee's results, the overall trend of measured mass density with respect to measured heat of fusion is largely smeared by the large error bars in the density results, and consequently, the extrapolation is also severely affected. Another possible reason is that, as suggested by Snyder et al., a proper crystal size correction may be necessary for determining the heat of fusion in their DSC measurements.[10]

Finally, it is interesting to note that in the recently reported high-performance p-type semiconducting polymers exhibiting state-of-the-art hole mobility, long-range order is usually absent and instead, only weak reflections, if any, were shown, suggesting that the local short-range ordering may be a general feature for high-performance semiconducting polymers having rigid conjugated backbones.[35–38] Moreover, it is proposed by Noriega et al. that, provided good interconnectivity between aggregates, short-range intermolecular aggregations are sufficient for efficient long-range charge transport.[38] Therefore, developing a quantitative understanding of the short-range ordering by using a combination of characterization techniques covering different length scales as demonstrated above would be highly desirable to designing and modifying new classes of semiconducting polymers.

3.4 Conclusions

In summary, we have used a combination of scattering (WAXD), physical (density measurement), and spectroscopic (solid-state NMR) methods to determine the absolute degree of crystallinity in three different P3HT bulk samples with identical pre-determined thermal history, and shown that the results for the three samples differing in molecular characteristics, obtained from three different characterization techniques, are in qualitative agreement. Quantitatively, owing to the greater sensitivity to the intermolecular ordering at short-range length scale, the NMR-determined crystallinity, for all three samples under investigation, is consistently ~10% greater than those determined by WAXD, suggesting the existence of a short-range ordered phase located in the amorphous region of rr-P3HT. Interestingly, it is shown that the local short-range

ordering also exists in regiorandom P3HT, which obviously lacks long-range order and is

regarded as amorphous in WAXD, UV-Vis and DSC measurements.

3.5 References

1. Ro, H. W.; Akgun, B.; O'Connor, B. T.; Hammond, M.; Kline, R. J.; Snyder, C. R.; Satija, S. K.; Ayzner, A. L.; Toney, M. F.; Soles, C. L.; DeLongchamp, D. M. *Macromolecules* **2012**, *45*, 6587–6599.

2. Collins, B.; Tumbleston, J.; Ade, H. *J. Phys. Chem. Lett.* **2011**, *2*, 3135–3145.

3. Balko, J.; Lohwasser, R. H.; Sommer, M.; Thelakkat, M.; Thurn-Albrecht, T. *Macromolecules* **2013**, *46*, 9642–9651.

4. Brinkmann, M.; Rannou, P. *Macromolecules* **2009**, *42*, 1125–1130.

5. Clark, J.; Chang, J.-F.; Spano, F. C.; Friend, R. H.; Silva, C. *Appl. Phys. Lett.* **2009**, *94*, 163306.

6. Rivnay, J.; Mannsfeld, S. C. B.; Miller, C. E.; Salleo, A.; Toney, M. F. *Chem. Rev.* **2012**, *112*, 5488–5519.

7. Jimison, L. H.; Himmelberger, S.; Duong, D. T.; Rivnay, J.; Toney, M. F.; Salleo, A. *J. Polym. Sci. Part B Polym. Phys.* **2013**, *51*, 611–620.

8. Lee, C. S.; Dadmun, M. D. *Polymer* **2014**, *55*, 4–7.

9. Wu, Z.; Petzold, A.; Henze, T.; Thurn-Albrecht, T.; Lohwasser, R. H.; Sommer, M.; Thelakkat, M. *Macromolecules* **2010**, *43*, 4646–4653.

10. Snyder, C. R.; Nieuwendaal, R. C.; DeLongchamp, D. M.; Luscombe, C. K.; Sista, P.; Boyd, S. D. *Macromolecules* **2014**, *47*, 3942–3950.

11. Nieuwendaal, R.; Snyder, C. R.; DeLongchamp, D. M. *ACS Macro Lett.* **2014**, *3*, 130–135.

12. Dudenko, D.; Kiersnowski, A.; Shu, J.; Pisula, W.; Sebastiani, D.; Spiess, H. W.; Hansen, M. R. *Angew. Chem. Int. Ed. Engl.* **2012**, *51*, 11068–11072.

13. Pascui, O. F.; Lohwasser, R.; Sommer, M.; Thelakkat, M.; Thurn-Albrecht, T.; Saalwächter, K. *Macromolecules* **2010**, *43*, 9401–9410.

14. Weidinger, A.; Hermans, P. *Makromol. Chemie* **1961**, *50*, 98–115.

15. Mandelkern, L. *Polym. J.* **1985**, *17*, 337–350.

16. Hu, W.; Sirota, E. B. *Macromolecules* **2003**, *36*, 5144–5149.

17. Kitamaru, R.; Horii, F.; Murayama, K. *Macromolecules* **1986**, *19*, 636–643.

18. Ruland, W. *Acta Crystallogr.* **1961**, *14*, 1180–1185.

19. Loewe, R. S.; Khersonsky, S. M.; McCullough, R. D. *Adv. Mater.* **1999**, *11*, 250–253.

20. Chen, T.; Wu, X.; Rieke, R. *J. Am. Chem. Soc.* **1995**, 233–244.

21. Zhang, F.; Ilavsky, J.; Long, G. G.; Quintana, J. P. G.; Allen, A. J.; Jemian, P. R. *Metall. Mater. Trans. A* **2009**, *41*, 1151–1158.

22. http://henke.lbl.gov/optical_constants.

23. Hubbell, J.; Veigele, W.; Briggs, E. A.; Brown, R. T.; Cromer, D. T.; Howerton, R. J. *J. Phys. Chem. Ref. Data* **1975**, *4*, 471–538.

24. Metz, G.; Ziliox, M.; Smith, S. O. *Solid State Nucl. Magn. Reson.* **1996**, *7*, 155–160.

25. Shen, X.; Duzhko, V. V.; Russell, T. P. *Adv. Energy Mater.* **2013**, *3*, 263–270.

26. Colle, R.; Grosso, G.; Ronzani, A.; Zicovich-Wilson, C. M. *Phys. status solidi* **2011**, *248*, 1360–1368.

27. Mo, Z.; Lee, K. B.; Moon, Y. B.; Kobayashi, M.; Heeger, A. J.; Wudl, F. *Macromolecules* **1985**, *18*, 1972–1977.

28. Brinkmann, M.; Rannou, P. *Adv. Funct. Mater.* **2007**, *17*, 101–108.

29. Kohn, P.; Huettner, S.; Komber, H.; Senkovskyy, V.; Tkachov, R.; Kiriy, A.; Friend, R. H.; Steiner, U.; Huck, W. T. S.; Sommer, J.-U.; Sommer, M. *J. Am. Chem. Soc.* **2012**, *134*, 4790–4805.

30. Kayunkid, N.; Uttiya, S.; Brinkmann, M. *Macromolecules* **2010**, *43*, 4961–4967.

31. Lazzeretti, P. *Prog. Nucl. Magn. Reson. Spectrosc.* **2000**, *36*, 1–88.

32. Van Rossum, B. J.; Steensgaard, D. B.; Mulder, F. M.; Boender, G. J.; Schaffner, K.; Holzwarth, a R.; DeGroot, H. J. *Biochemistry* **2001**, *40*, 1587–1595.

33. Mowery, D. M.; Harris, D. J.; Schmidt-Rohr, K. *Macromolecules* **2006**, *39*, 2856–2865.

34. Litvinov, V. M.; Kurelec, L. *Polymer* **2014**, *55*, 620–625.

35. Street, R. A. *Science* **2013**, *341*, 1072–1073.

36. Zhang, X.; Bronstein, H.; Kronemeijer, A. J.; Smith, J.; Kim, Y.; Kline, R. J.; Richter, L. J.; Anthopoulos, T. D.; Sirringhaus, H.; Song, K.; Heeney, M.; Zhang, W.; McCulloch, I.; DeLongchamp, D. M. *Nat. Commun.* **2013**, *4*, 2238–2246.

37. Tsao, H. N.; Cho, D. M.; Park, I.; Hansen, M. R.; Mavrinskiy, A.; Yoon, D. Y.; Graf, R.; Pisula, W.; Spiess, H. W.; Müllen, K. *J. Am. Chem. Soc.* **2011**, *133*, 2605–2612.

38. Noriega, R.; Rivnay, J.; Vandewal, K.; Koch, F. P. V; Stingelin, N.; Smith, P.; Toney, M. F.; Salleo, A. *Nat. Mater.* **2013**, *12*, 1038–1044.

CHAPTER 4

REVEALING THE SIGNIFICANT EFFECT OF SUBTLE STRUCTURAL CHANGES ON THE HOLE TRANSPORT PROPERTIES OF P3HT USING SOLID-STATE NMR

4.1 Introduction

rr-P3HT represents a prototype of side-chain substituted semi-crystalline polymers and is undoubtedly one of the most studied p-type semiconducting polymers. It has found wide use as hole conductor in organic electronic devices such as thin film field-effect transistors (FET)[1] and bulk heterojunction solar cells.[2] It is well documented in a great number of literatures that the electronic properties of P3HT in devices are strongly dependent on the semi-crystalline morphology and stacking structures, which can be effectively tuned by varying the molecular parameters (i.e. molecular weight, regioregularity) and processing conditions (i.e. thermal and solvent annealing, chain alignment).[3–9] Taking FET devices for instance, structural factors such as macroscopic degree of crystallinity,[6,10] grain boundaries[8] and microscopic molecular order and orientation with respect to the substrate and the transport channel,[11,12] have been identified as keys to improving the hole mobility, suggesting that the charge carrier transport in semi-crystalline P3HT may have a hierarchical nature.[13] Indeed, as suggested in Chapter 2, at a macroscopic length scale, the coexistence of ordered phase favoring hole transport and disordered phase impeding holes carriers would largely complicate the transport paths along which the holes must travel; while at a microscopic length scale, similar to the heterogeneity present in the molecular packing and dynamics of P3HT,[14] the hole transport within the P3HT crystalline region is also found to be highly

anisotropic as suggested by quite a few experimental and theoretical studies.[11,15,16] Interestingly, the important issues of molecular and microstructures at multi-length scales has been further discussed in a recent work by Noriega et al., where, by compiling mobility data obtained for a broad range of semiconducting polymers available in the literatures, it is generalized that, the macroscopic connectivity between the ordered grains and the microscopic π-π stacking paracrystalline disorder are the limiting factors in the low and high molecular weight regimes, respectively.[16] These studies clearly indicate that the macroscopic charge transport behaviors are strongly correlated with a wide array of structural properties scaling from segmental level up to inter-grain level. Yet, a thorough and quantitative understanding of the highlighted features, for instance, the macroscopic connectivity, the microscopic lattice disorder, is still limited even for the "golden standard" rr-P3HT.

^{13}C solid-state NMR methods have been reported to be useful in revealing the local structural changes in poly (3-alkylthiophene) (P3ATs) based on its sensitivity to molecular conformation and dynamics.[14,17–20] By using ^{13}C Magic Angle Spinning (MAS) NMR, Pascui and co-workers have studied a crystal-crystal transition at ~60°C featuring low molecular weight P3HT of Form II,[21] and concluded that, during the transition, the initially ordered hexyl side chains undergo disordering processes with the introduction of more disordered gauche content, while the average conformation and mobility of main chains remain unaffected.[14] In addition, a quantitative determination of the degree of crystallinity was enabled by a differentiation of distinct side chain conformations in ordered and disordered phases. In a recent ^{13}C CPMAS NMR study employing high molecular weight P3HT of Form I, Nieuwendaal et al. have observed

dynamic motions in both the side chain and main chain in rr-P3HT crystals in temperature-dependent measurements and suggested that rr-P3HT crystals contain dynamic disorder even at room temperature.[20] Another interesting ^{13}C CPMAS NMR work by Yazawa et al. have highlighted a solid phase structural transition in regioregular poly(3-butylthiophene) (rr-P3BT) at around 67°C and, based on FTIR and ^{13}C NMR results, attributed it to a twist-glass transition involving a quasiordered phase with thiophene twist in the crystals.[18]

In this Chapter, we present intrinsic hole transport properties of rr-P3HT measured by TOF as a function of physical aging as well as temperature, which demonstrate significant aging effects at low temperatures and a structural transition at high temperature. The corresponding structural changes in the bulk have been primarily characterized by ^{13}C CP/MAS NMR, which helps to establish a correlation between the hierarchical transport behaviors and the multi-scale structures in rr-P3HT. Our NMR results indicate that the local short-range ordered phase located in the noncrystalline region, as we describe in Chapter 3, grows during physical aging at room temperature and, thus, coarsens the efficient pathways connecting crystalline grains, leading to the improved hole transport properties and providing experimental evidence for the connectivity argument described above. On the other hand, we show that the resonance peak of the protonated carbon on the thiophene ring can be used as a sensitive indicator of molecular packing structures within the P3HT crystals, and that the crystalline phase undergoes a stress relaxation process above certain temperature range, which is thought to be responsible for the observed jump in TOF hole mobility.

4.2 Experimental Section

4.2.1 Time-of-Flight Mobility Measurements

The molecular characteristics of rr-P3HTs measured in the TOF measurements are provided in Table 4.1. The materials have different molecular weights, but similar polydispersity and regioregularity. For TOF measurements, samples were prepared by a drop-casting method described in 2.2.1. Notably, we have used a modified thermal treatment recipe for all the TOF samples, that is melt the rr-P3HT film above the melting point to remove the residual o-dichlorobenzene and the unknown thermal history and then slowly ramp down to room temperature at 0.2^oC/min to let the materials fully order. Both the complete removal of thermal history above the melting point and the slow cooling process are found to be important to yield best device performance and consistent features.

The experimental details of the TOF measurements have been discussed 2.2.1. With the knowledge of the film thickness of each sample, the electric field was kept the same for each measurement so that a direct comparison can be made for different samples measured at the same temperature.

Table 4.1: The Number-Average Molecular Weight (Mn), Polydispersity (PDI) and Regioregularity of rr-P3HTs Used in the Current TOF Measurements.

	Mn	PDI	regioregularity
rr-P3HT	10K	1.3	95%
rr-P3HT	24K	1.2	96%
rr-P3HT	32K	1.3	96%

4.2.2 Temperature-resolved Wide Angle X-ray Diffraction Measurements

For temperature-resolved WAXD measurements, the 32K rr-P3HT listed in Table 4.1 was used as a representation. The samples were prepared in a similar manner. Polymer powders were sealed in a hermetical differential scanning calorimeter (DSC) pan to ensure good thermal conductivity, which was placed on a heating stage constantly purged with N_2 gas and subject to the same slow cooling thermal treatment as described above. Finally, the sample enclosed in the DSC pan was physically aged at room temperature for ~9 days prior to the WAXD measurements.

Temperature-resolved WAXD measurements were performed on Beamline 7.3.3 at the Advanced Light Source (ALS) at the Lawrence Berkeley National Laboratory (LBNL). A transmission geometry was used. The wavelength of the x-rays is 1.240Å and the diffracted photons were collected by a two dimensional Pilatus 1M detector. A home-made helium box purged with He gas was used to reduce the unwanted air scattering and ensure clean background. A heating stage (Linkam) with a built-in sample cell accommodating the DSC sample pan, was mounted into the beamline with a sample-to-detector distance of ~205 mm. The aged sample was heated to 250°C stepwise at a rate of 10°C/min and then kept at each temperature set-point for 10 min before the measurement. After cooling from 250°C in ambient condition, measurement was repeated for a second heating cycle as well. Each measurement was done with 60s exposure time. Correction for geometry and polarization was carried out for the diffraction followed by subtraction of background arising from the pan as well as parasitic scattering.

77

4.2.3 ^{13}C Solid-State Nuclear Magnetic Resonance Measurements

For NMR measurements, due to the lack of previously studied materials, a 34K rr-P3HT was used instead (PDI~2, regioregularity~93%). The NMR samples were prepared in the same way as the WAXD samples except that the rr-P3HT bulk sample was taken out of the DSC pan after the thermal treatment. The thermal treatment procedures for investigating the low temperature aging effects and high temperature structural transition are described in 4.3.2. Although the important features resolved in TOF at low and high temperatures seem to be relatively independent of the molecular parameters as shown in Figure 4.1, we note that the introduction of the new material to the structural investigation may not lead to a strict one-to-one comparison with the TOF results in an absolute sense.

All NMR experiments were conducted on a Bruker DSX300 spectrometer, operating at a ^{1}H frequency of 300.12 MHz and ^{13}C frequency of 75.47 MHz, in 4mm CP/MAS probes. The pulse sequence was a 90° pulse followed by an optional ^{1}H spin lock pulse before CP and high-power ^{1}H decoupled ^{13}C detection. The chemical shift was externally referenced by polydimethylsiloxane peak at 1.4 ppm. For crystallinity determination, 7 ms of spin lock with a field strength of 60 kHz was used. A RAMP-CP scheme was used for cross polarization, which has been shown to generate a more quantitative representation of non-protonated carbons.[22] The ramp size was 5 kHz and the contact time was 3 ms. The recycle delay, decoupling field, and spinning speed were 1.2 s, 65 kHz and 5 kHz, respectively.

4.3 Results and Discussion

4.3.1 Hole Mobility Measured by Time-of-Flight Technique

Three rr-P3HT materials having similar polydispersity and regioregularity, but with increasing number-average molecular weights (Mn), 10K, 24K and 32K, were chosen for the TOF measurements. The hole mobility was measured by the Time-of-Flight technique, which, as described previously in 2.3.1, probes the intrinsic transport characteristics of the charge carriers in the bulk of materials. All the thick films used for TOF measurements were thermally treated in the same way. Specifically, the P3HT thick films were molten on a hot plate and then ramped down to room temperature at a rate of $0.2^{o}C$/min. This process, termed slow-cooling in the following text, is intended to remove the previous unknown thermal history, and impart maximum degree of ordering in P3HT by allowing the chains to fully order during the extremely slow cooling process. After Al electrode deposition, the samples were measured either immediately or re-heated up to $210\ ^{o}C$/min and cooled down to room temperature at a constant rate of $1^{o}C$/min prior to measurements. During the hole mobility measurements on heating, the temperature was increased in step-like increments of $10^{o}C$ and stabilization time of 10 minutes, and on cooling - with a ramp of $1^{o}C$/min and stabilization time of 5 minutes. This procedure produced a relatively good reversibility of hole mobility during the heating and cooling cycles in such "non-aged" samples. The hole mobility for the "non-aged" rr-P3HT of different molecular weights is shown in Figure 4.1 (blue squares). To investigate the effect of physical aging on the hole transport properties of rr-P3HT, same samples were stored in a N_2-filled glove box for ~14 months and, subsequently, measured by TOF as a function of temperature under identical change of temperature and electric field (Figure

4.1, red circles). Subsequent cooling of aged samples produced the hole mobilities that were close to the values of non-aged material.
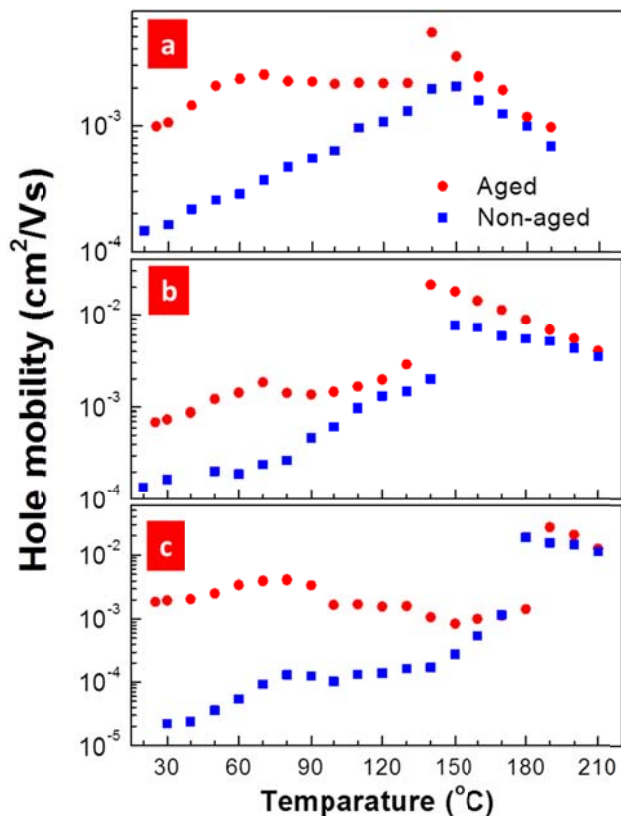
Figure 4.1: Hole mobility measured by the Time-of-Flight technique during heating for non-aged (blue square) and physically aged (red circle) rr-P3HT with different molecular weights (a)10K; (b) 24K; (c) 32K.

Strikingly, even with the seemingly mild physical aging at room temperature, significant improvements in the hole mobility were obviously seen in all three samples. Notably, the most pronounced change induced by aging happened at the very initial stage at room temperature, with 10K and 24K sample exhibiting almost an order of magnitude increase from 10^{-4} cm^2/Vs to 10^{-3} cm^2/Vs, and 32K exhibiting more than two orders of magnitude increase from 10^{-5} to above 10^{-3} cm^2/Vs. It is also obvious that the hole mobility difference between aged and non-aged samples is gradually reduced as

temperature is elevated, indicating that the aging–induced changes are gradually erased by increasing temperature. In the non-aged samples, the hole mobility at room temperature showed a negative dependence on the molecular weight, which is consistent with previous TOF investigations on P3HT with different molecular weights.[23] We note that the decrease of TOF hole mobility with increasing molecular weight contradicts the general increasing trend found in FET devices, which may be attributed to the marked difference in the sampling geometries and transport length scales. Nevertheless, the drastic improvements of hole mobility in the physically-aged samples across the molecular weights from 10K, forming extended-chain crystals, to 32K, forming chain-folded crystals, strongly suggest that physical aging at room temperature has introduced significant transport-relevant structural changes, most likely in the amorphous phase in the materials.[24,25] In qualitative agreement with the results shown in Figure 2.2 (a), the hole mobility of non-aged samples initially increased with elevating temperature, reached maximum at a high temperature of ~140°C for 10K and 24K samples and at ~180°C for 32K sample, and then decrease with further heating. Similar trend is also observed for the aged samples at low and high temperatures except that the mobility at intermediate range from 70°C to 140°C (80°C to 180°C for 32K) was leveled off and weakly dependent on temperature. Additionally, another striking feature is that, regardless of the aging history, a vertical jump in the hole mobility was found at high temperatures, although the changes in the aged samples seem to be more significant than those in non-aged ones. The abrupt nature of the increase, coupled with the fact that both the magnitude and temperature at which the jump in mobility occurs increased with the P3HT molecular weight, suggest the occurrence of a sudden structural change at high temperature and that the origin of the

corresponding structural change may be related to kinetic factors. In comparison to results presented in section 2.3, it is evident that finer features, for instance, the abrupt jump at high temperature, are more prominent in the current temperature-dependent measurement. We attribute this primarily to the fact that the unknown thermal history in the current samples were removed by melting the films prior to cooling, whereas the samples in previous measurements were annealed at 210°C without being molten. Also, the broad polydispersity (PDI~2) of our previous sample may smear out the fine features resolved here on narrow-dispersed materials (PDI: 1.2~1.3). It should be noted that, although we report the effect of physical aging after 14 months, the most drastic changes in the temperature dependence of mobility occur over the period of the first 10 days (not shown). Due to positive electric field dependence of hole mobility in the low temperature range and a negative one in the high temperature range (See 2.3.1), the largest contrast in the temperature dependence of hole mobility was achieved for the lowest values of electric fields that the measurements were feasible, 20 kV/cm.

4.3.2 Low Temperature Structural Changes Revealed by ^{13}C Solid-State NMR

Given the fact that room temperature is well below the transition temperatures reported for rr-P3HT,[18,26,27] it is reasonable to assume that physically aging P3HT at room temperature is not expected to result in large-scale molecular rearrangements in the rr-P3HT crystals. Thus, the enhancement of the hole mobility with aging at low temperatures is more likely related to structural changes in the amorphous region at a local scale. This is supported by a combination of WAXD, DSC and infrared spectroscopy (IR) measurements where no obvious changes were discernible for the samples with and without physical aging.(Data not shown) Therefore, we have chosen

^{13}C solid-state NMR as a primary tool, which is more sensitive to local structural changes at short-range scale. Due to the subtlety associated with physical aging, the samples for NMR were first molten to remove thermal history and then quenched in liquid nitrogen from melt as schematically illustrated in Figure 4.2 (b). The rapid quench from melt is intended to maximize the driving force and, hence, the structural changes induced by physical aging. ^{13}C solid-state NMR was used to monitor the structural changes for the same quenched sample during a total period of 9 days.

On the other hand, the abrupt jump in hole mobility observed at high temperatures (140~180°C) in Figure 4.1 most likely has a structural origin, and appears to be independent of the aging history. To approach this structural origin, molten samples were first quenched in liquid nitrogen, subsequently annealed below and above the observed transition temperature in the hole mobility data, respectively, and finally quenched in liquid nitrogen again to freeze the structures. The schematics illustrating the detailed thermal treatments including the aforementioned slow-cooling process are provided in Figure 4.2.

In order to better understand and compare the spectral features, a slow-cooled rr-P3HT sample, representing a well ordered state with high degree of crystallinity, and a rr-P3HT sample dissolved in deuterated chloroform, representing a truly amorphous state, were also measured by ^{13}C NMR and included and shown in Figure 4.3, together with the sample measured an hour after quench (termed "as-quenched" in the following) and the sample physically aged at room temperature for 9 days.
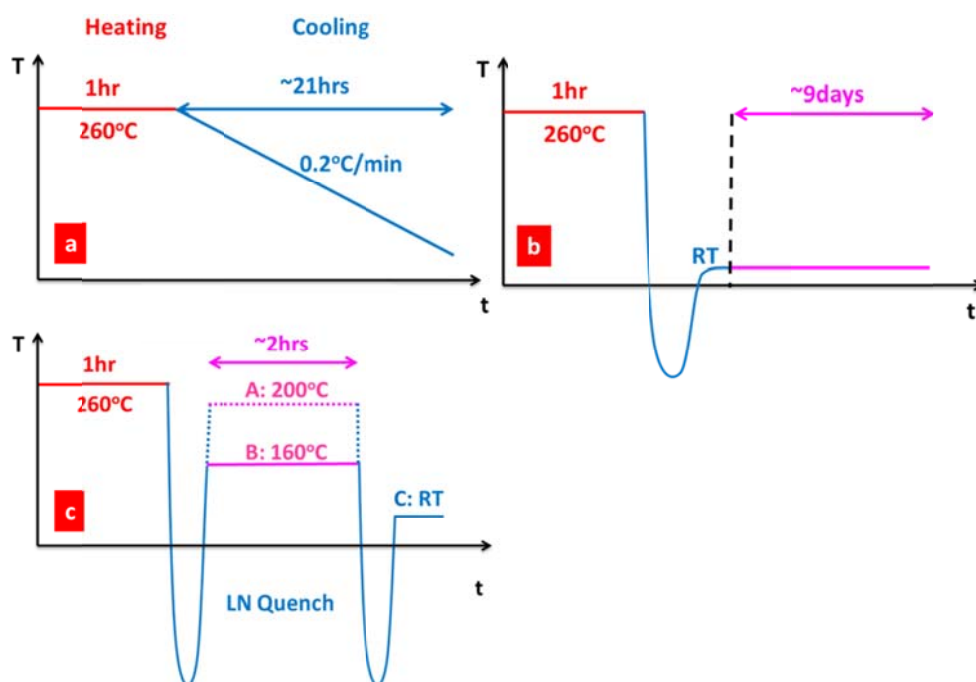
Figure 4.2: Schematics illustrating the temperature profiles for (a) slow-cooling from melt; (b) quench from melt and age at room temperature; (c) quench from melt, thermally anneal below and above transition temperatures observed in TOF, and quench again to freeze the structures.
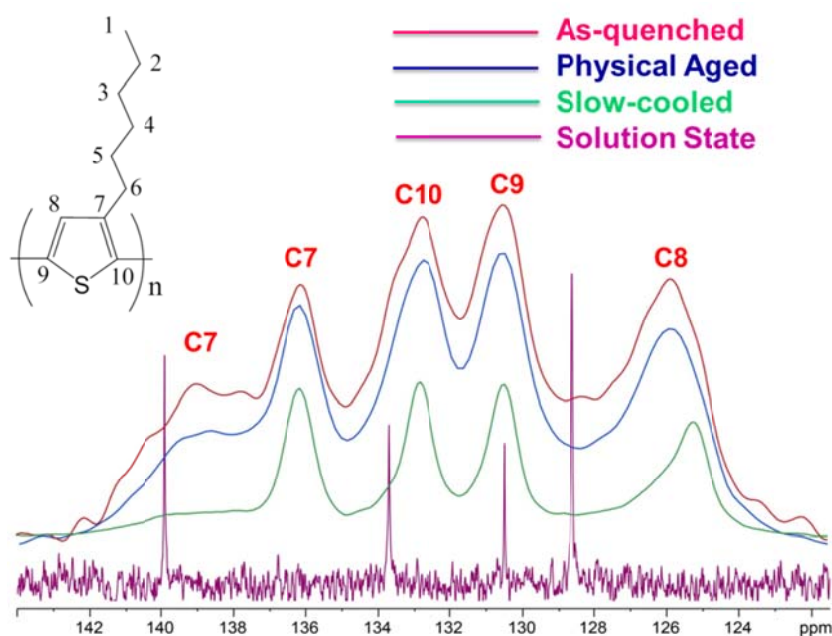
Figure 4.3: CP/MAS ^{13}C NMR spectra of rr-P3HT comparing as-quenched from melt (1 hour after quench; red), aged for 9 days following the quench from melt (blue), slow-cooled from melt (green) and dissolved in CDCl$_3$ (purple).

The highly disordered state in the as-quenched sample is most evident when compared with the solution sample in which P3HT chains are fully solubilized in a good solvent, chloroform, and therefore can be regarded as an amorphous state. Aggregation shifts of 3.5~4 ppm for C7 and C8 and ca. 1 ppm for C10 due to $\pi-\pi$ stacking are readily seen in the spectrum of as-quenched sample, suggesting that the crystallization kinetics of P3HT is remarkably rapid and that a truly amorphous rr-P3HT is nearly impossible to obtain even by rapid quenching from melt. In addition to the shoulder located at ~139 ppm, which has been assigned to the amorphous fraction of C7,[20] two additional small shoulders located at ~134 ppm and 128.5 ppm were consistently observed for the freshly quenched rr-P3HT samples in several quench attempts, which were absent in slow-cooled samples. It is interesting to note that the locations of the two small shoulders coincide with the corresponding carbon resonance peaks in the solution state, indicating that the completely disordered fraction is quite large. The disorder in the quenched sample is further supported by the much more pronounced C7 shoulder at ~139 ppm as compared with that in the slow-cooled sample. Indeed, the as-quenched sample represents the most disordered state of rr-P3HT, which, in turn, is expected to provide the largest thermodynamic driving force for physical aging.[28–30] Another intriguing feature arises from the C8 resonance peak, which has been identified to be particularly sensitive to the packing structures of P3HT among other main chain carbons[18,31]: comparing the ^{13}C NMR spectrum of the as-quenched sample with that of slow-cooled sample, the resonance peaks originating from main chain carbons are positioned at similar positions except for C8, the chemical shift of which clearly shows a ~0.8 ppm shift towards up-field for the slow-cooled rr-P3HT. This shift, given the marked difference between these

two samples in terms of preparation condition, is attributed to the different amount of aggregation shift caused by different molecular packing within the crystalline phase. Therefore, the C8 peak can be a useful indicator evaluating the internal packing of rr-P3HT. As the as-quenched sample physically ages at room temperature for 9 days, the spectrum was acquired at various intervals and compared to the original spectrum in as-quenched state. Qualitatively, after physical aging, the amorphous shoulder of C7 decreases in intensity, which is accompanied by a concurrent increase in the C7 crystalline peak. The change of relative shoulder to peak intensity is a clear sign of increasing order in the materials during the course of physical aging. A more quantitative analysis is performed to calculate the degree of crystallinity as a function of aging time from the ^{13}C NMR spectra. Following is a summary of the procedure for quantifying the degree of crystallinity using ^{13}C NMR:

1. Crystallinity of the as-quenched sample was determined by spectral editing of two CP spectra (with and without a 7-ms spin-lock period before CP). A detailed description of the procedure has been described in 3.3.3.

2. To minimize uncertainty due to the inevitable subjectivity during spectral editing, crystallinity at other time intervals were determined from Equation 4-1:

$$X_c = \frac{1}{1 + \dfrac{H_a}{H_c}\dfrac{H_c^0}{H_a^0}\left(\dfrac{1}{X_c^0} - 1\right)}$$

Eq. 4-1

where Ha is the signal height for the C8 shoulder between 138 ppm and 139.5 ppm, and Hc is the signal height between the foot of the C8 amorphous shoulder and the top of the 136 ppm peak. Since both the crystalline and amorphous peak shapes do not change

during the aging process, it is reasonable to assume that Ha/Hc is proportional to the ratio of amorphous vs. crystalline population. The terms with a superscript "0" refer to the values for the as-quenched sample. The error bars were determined by the level of noise on the spectra. The first two data points had larger error bars due to fewer numbers of scans. Since there are rapid structural changes at the beginning of the aging process, shorter experiments (40~80 min) were acquired as opposed to longer experiments at longer aging times.
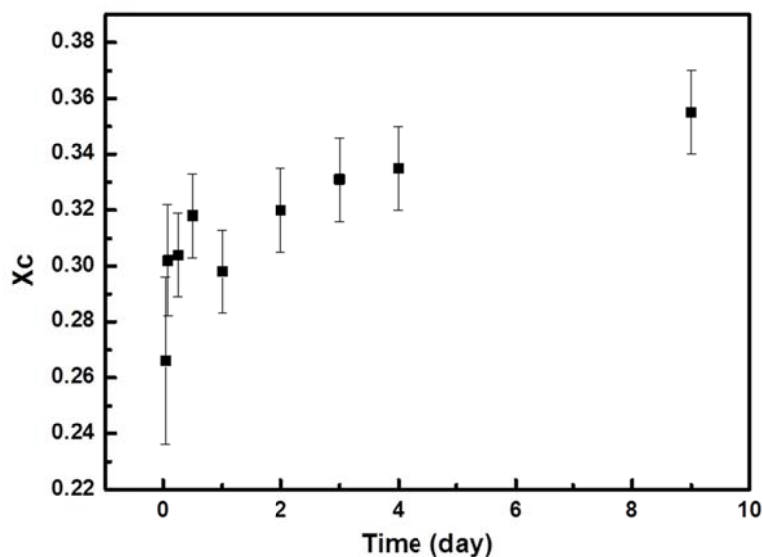
Figure 4.4: The degree of crystallinity of the as-quenched rr-P3HT determined by ^{13}C NMR as a function of aging time up to 9 days.

As shown in Figure 4.4, the degree of crystallinity of the as-quenched sample was only ~27% and increased rapidly to ~32% after one day of aging owing to the large driving force in the initial as-quenched state. Through the remainder of the aging period up to 9 days, the growth of order slows down, yielding a total increase of ~9% in the measured degree of crystallinity using NMR. Despite the fact that the T_g of rr-P3HT is widely scattered from -14°C to 34°C due in large part to the varying molecular parameters and preparation conditions,[32–34] it is evident from Figure 4.4 that, at room

87

temperature, the structural change caused by physical aging, even for the extreme case of as-quenched sample, is slow and likely confined to local environments in the amorphous phase because of the limited chain mobility at this temperature. Moreover, neither the shape nor the position of C8 resonance peak was changed after physical aging, suggesting that there was no apparent change associated the molecular packing within the original crystalline phase and that the ~9% grown ordered fraction has a relatively disordered molecular packing similar to that seen in the as-quenched state. Therefore, it is concluded that, for the as-quenched P3HT sample, physical aging has led to an increasing degree of local short-range ordering in the amorphous phase, which amounts to about ~9% after a total aging period of 9 days. The growth of the short-range order at local scale during physical aging was monitored in the slow-cooled sample as well, however, the magnitude turned out to be much reduced compared with quenched sample and thus disallowed a quantitative investigation. Since the amorphous phase has been identified as a potential barrier for the hole transport in P3HT at low temperature,[6] the growth of the local short-range order in the noncrystalline region as a result of physical aging is expected to, at least, lower the barrier by establishing efficient pathways in the amorphous phase, and may provide good connections between the ordered nanocrystal grains.

4.3.3 High Temperature Structural Changes Revealed by ^{13}C Solid-State NMR

To address the high temperature jump in TOF hole mobility, high molecular weight rr-P3HT (Mn~34K) was employed for the structural investigation using ^{13}C NMR. According to Figure 4.1, the transition temperature where the jump in hole mobility occurred for the 32K sample is ~180°C. Thus, the high molecular weight rr-P3HT (Mn~34K) was first quenched in liquid nitrogen from melt, immediately followed

by being annealed for 2 hours at 160°C, below the transition temperature, and 200°C, above the transition temperature, respectively. Finally, the annealed samples were quenched in liquid nitrogen again to lock in the structures and the ^{13}C NMR spectra are shown in Figure 4.5.
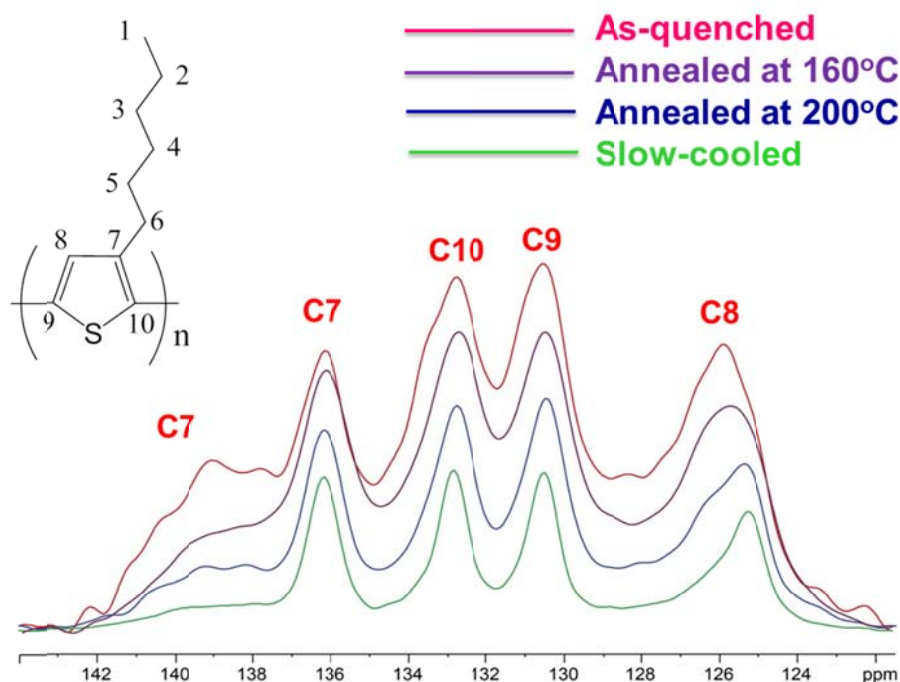
Figure 4.5: CP/MAS ^{13}C NMR spectra of rr-P3HT comparing as-quenched from melt (red), quenched from melt and annealed at 160°C for 2 hours (purple), quenched from melt and annealed at 200°C for 2 hours (blue) and slow-cooled (green).

In contrast to the physically aged sample in Figure 4.3, annealing rr-P3HT at high temperatures has led to a significant increase of ordering as the C7 amorphous shoulder located at 139 ppm is largely diminished for both samples annealed at 160°C and 200°C. Quite surprisingly, however, the C8 resonance peak, which has good sensitivity to the packing structure (i.e. π-π stacking) within the crystalline phase as described above, is distinctly different for the two samples annealed at 160 and 200°C. Specifically, the

chemical shift of the C8 resonance peak in the as-quenched sample shows no change even after annealing at 160°C, suggesting that the molecular packing structure was not altered after the extended annealing; while for the 200°C annealed sample, C8 peak shifted ~0.6 ppm towards up-field to the position of that of a slow-cooled sample, indicating an appreciable improvement of the molecular packing (i.e. π-π stacking) within the crystalline phase. It is noteworthy that, compared to the single C8 peak of slow-cooled sample, an additional hump located at 126~126.5 ppm can be seen for the C8 peak the sample annealed at 200°C, resulting in a two-component feature. This feature suggests that annealing the highly disordered as-quenched sample at 200°C for two hours has improved the majority of the molecular packing as evidenced by the up-field shift; however, certain part of the sample has remained the disordered molecular packing even after annealing, leading to the broad hump attached to the main peak. A modification in the π-π stacking as a result of structural transition has been reported by Yuan et al. in a temperature-dependent FTIR study, whereby a solid-state transition occurring at 54°C in slowly evaporated rr-P3HT crystals was assigned to a transition from Form I', a new crystal modification of rr-P3HT characteristic of a modified π-π stacking mode, to the most commonly observed Form I crystal.[24,26] Therefore, the improvement of molecular packing structure that we observed may be regarded as a crystal modification.[26] Most importantly, as suggested by Dag et al., this can have a profound impact on the electronic structures and, hence, the transport characteristics of rr-P3HT.[35] Furthermore, since the annealing time of two hours are quite long, the different chain packing structures from 160°C and 200°C treatments is likely due to the annealing temperature: a critical temperature that is higher than 160°C may exist for the packing modification process to

take place. Although the concomitant variations of other structural factors during heating from 160°C (below the transition temperature) to 200°C (above the transition temperature) should be taken into the consideration, the improvement of the π-π stacking structure within the crystalline phase is clearly crucial for enhancing the inter-molecular hole transport and can positively contribute to the hole mobility jump as seen in all the materials.

4.3.4 Structure – Hole Transport Correlations at Low Temperature

In Chapter 3, it has been emphasized that, in addition to the classic two-phase picture depicting crystalline and amorphous phases, the local short-range ordering in the amorphous phase should be introduced to properly describe the semi-crystalline morphology. Indeed, the significant hole mobility enhancement observed at low temperature is closely related to the growth of the local short-range ordering during physical aging, which stems from the amorphous phase of rr-P3HT that has a T_g lower than room temperature. This is supported by the low T_g of ~6°C found in regio-random P3HT as shown in Figure 4.6, which is chemically identical to its regio-regular counterpart and can be taken as a reasonable representative of the amorphous fraction of the rr-P3HT as regio-defects are partially excluded during crystallization and concentrated in the amorphous regions. Consequently, the physical aging process can be thought as a low temperature annealing process whereby the neighboring P3HT chains in the amorphous phase having truncated sequences of regioregularity can pack together, forming short-range ordered packing.[36]
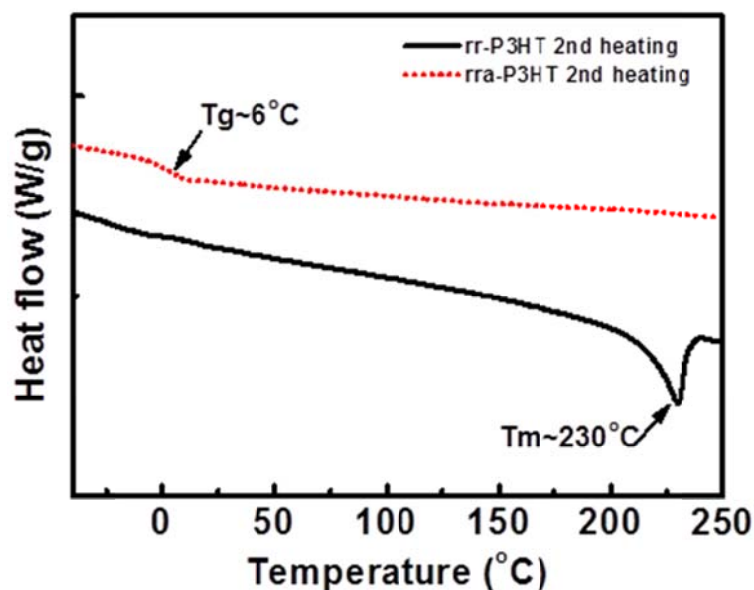
Figure 4.6: DSC traces during 2nd heating for rr-P3HT (black solid line) and rra-P3HT (red dotted line) showing a melting point of 230°C in rr-P3HT and a glass transition temperature of 6°C in rra-P3HT.

Interestingly, similar phenomenon has been reported by VanderHart and co-workers, who monitored the structural changes of isotactic polypropylene during room temperature aging by using proton NMR and found that at least 2~3 wt% of the materials were converted from mobile to rigid components over 4 days of aging period. Subsequently, the observed structural change has been attributed to a secondary crystallization process taking place in boundary regions distant from primary crystals, and it was suggested that the spatial dispersion of the secondary crystals was widespread throughout the noncrystalline regions.[36] Compared with a ~9% increase in NMR-determined crystallinity found in the quenched sample, the magnitude of change caused by physical aging in the slow-cooled TOF sample is considerably reduced due to the highly ordered initial state. In fact, no obvious changes were resolved from WAXD, IR and DSC measurements, supporting that the growth of the local short-range ordering

92

occurs at very small length scales and indicating that the subtle structural changes can indeed have remarkably great influence on the hole transport properties in rr-P3HT at low temperatures by overcoming the limiting factor --- the amorphous phase. It has been proposed in recent literatures that the hole mobility is limited by the amorphous phase and can be improved by having better connectivity between the crystalline grains.[16,37] Therefore, as schematically shown in Figure 3.11, it is reasonable to consider the short-range ordering as an intermediate phase located in the amorphous phases with widespread distribution, thereby functioning as efficient transport highways connecting crystalline grains. We suggest, but cannot unambiguously prove, that the grown short-range ordered phase during aging may exist in multiple forms, such as small tie-crystals comprising a few π-stacked P3HT chains,[38] interfacial components between crystalline and amorphous phases[39,40] or simply locally packed chains. We also note that, according to the C8 chemical shift difference between the aged sample and slow-cooled sample in Figure 4.3, the packing quality of the grown local short-range order is still poorer than that in the slow-cooled crystals. This implies that the holes may prefer to propagate along the intra-molecular direction when transport in those connecting domains. As discussed above, the contribution of the growth of local ordering to hole mobility is gradually diminished at intermediate temperature regions (i.e. 60$^{\mathrm{o}}$C~140$^{\mathrm{o}}$C for 10K and 80$^{\mathrm{o}}$C~180$^{\mathrm{o}}$C for 32K). Consequently, the change of slope in the TOF hole mobility before the abrupt jump can be assigned to the gradual disintegration of the pre-formed local short-range ordering arising from physical aging.

4.3.5 Structure – Hole Transport Correlations at High Temperature

At high temperatures, an interesting jump in hole mobility is observed for all the samples across different molecular weights. It is important to note that the macroscopic charge transport in the semi-crystalline rr-P3HT is not dictated by single structural factor but rather, an entangled combination of variants, including the degree of crystallinity, π-π stacking d-spacing, coherence length, crystal thickness, crystal packing, planarity/conjugation length as well as thermal activation.[6,41,42] In practice, a quantitative separation of the contribution from each factor is difficult. As shown in Figure 4.7, temperature-resolved wide angle X-ray diffraction (WAXD) measurements on the physically aged sample revealed that the d-spacings of π-π stacking direction (020) thermally expanded, while the number of (020) planes along each coherence length remained almost constant when the temperature was elevated from 160°C to 200°C. Moreover, it was qualitatively concluded from comparing the diffraction area at 160°C and 200°C that the degree of crystallinity also decreased during heating. Therefore, all these factors are not expected to contribute to the hole mobility increase. According to Gibbs-Thomson equation, the crystal thickness is expected to increase in a continuous manner. Considering the rather abrupt nature of the mobility increase, we attribute the jump in mobility at high temperature to the improvements of molecular packing structures inside the crystalline grains as evidenced by the C8 resonance peak shift in ^{13}C NMR as discussed in 4.3.3. In contrast to the aging effects, which take effect in the amorphous phase, the structural transition within the crystalline phase seems to be more important for hole transport at high temperatures.
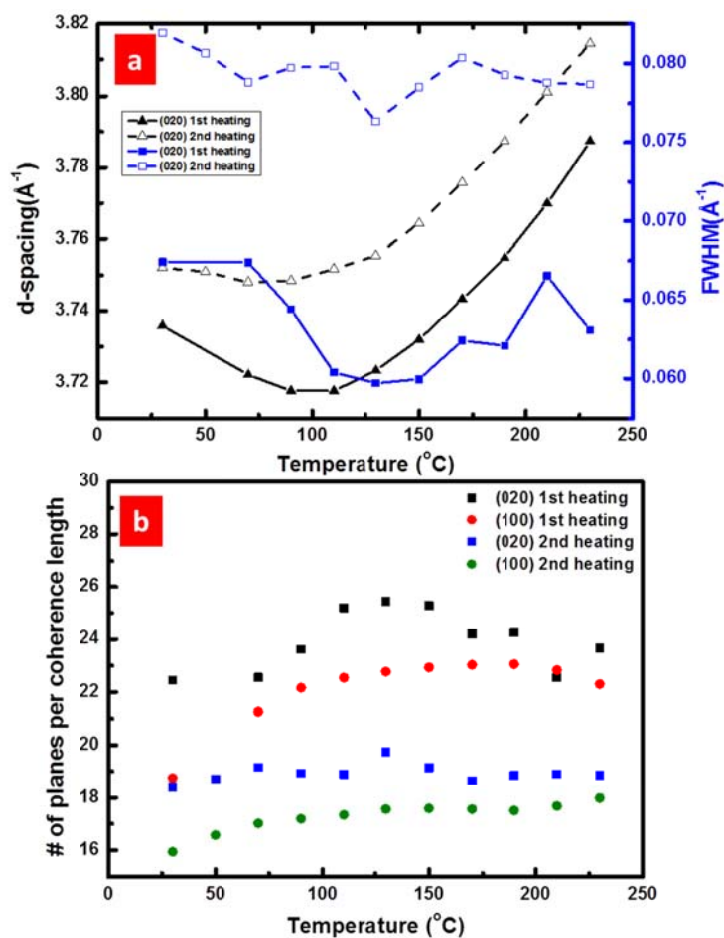
Figure 4.7: (a) Thermal evolution of d-spacing (black) and peak full widths at half maximum (FWHM) (blue) for 32K rr-P3HT during first heating (aged state, solid symbols) and second heating (non-aged state, open symbols) cycles; (b) number of crystal planes calculated by dividing the coherence length (calculated using Scherrer equation and FWHM in (a)) by the d-spacing of (100) plane and (020) plane (from (a)) during first and second heating cycles.

The origin of initial disorder inside the crystalline phase may be related to the local stresses accumulated within the crystals during crystallization, likely due to the twisting of backbones, incorporation of regiodefects (i.e. tail-to-tail), thereby forming local defects locked within the crystalline lattice and causing the disordering along the π-π stacking. Another possible origin of local stress, as proposed by Brinkmann and co-workers by using high-resolution TEM, is the tilting of chain axes in the lamellar domain

caused by the chain folding.[38] It should be noted that the transition temperature observed in our TOF hole mobility results is much higher than the solid-state transition temperatures of rr-P3HT reported by Yazawa et al. and Yuan et al.[18,26] In fact, at such high temperature, the side chains of rr-P3HT are molten and the P3HT crystal is expected to resemble the structure of a liquid crystal whereby the liquid-like inter-layer composed of side chains may, to some degree, lubricate and facilitate the motion of the main chains.[27,43,44] As a consequence, a structurally possible interpretation for the high temperature transition is that thermal annealing above the transition temperature imparts sufficient energy to unlock the polythiophene backbones and, hence, relax the local stresses inside the crystalline lattice by rotational and/or translational motions of backbones, thereby enhancing the inter-molecular transport within the crystalline phase. Although the conjugation length may decrease with increasing temperature,[42] it is also possible that the elimination of the defects along the backbone (e.g. twist) would improve the intra-molecular transport, which is the most efficient propagation pathway for the holes. Meanwhile, the observation that the transition temperature, at which the hole mobility jumps, is higher for higher molecular weight sample seems to suggest that local stress developed during crystallization may be engendered by multiple kinetic constraints (i.e. chain folding, entanglement, etc.) involved in the organization of long chains into crystalline lattices. This kinetically driven stress build-up in the crystals is consistent with Brinkamann's molecular weight dependent study where disordered crystalline packing in high molecular weight P3HT was directly visualized by high-resolution TEM.[38] We would like to note that no detailed structural models are available at this point to fully explain the spectroscopic findings presented here. To that end, further quantitative

computational efforts would be highly desirable and would be the direction for future studies. Nevertheless, it is evidently suggested by our results that, in terms of charge transport, the optimum temperature for thermal annealing treatment, which has been widely performed on organic electronic devices, should be chosen according to the molecular weights so that both the macroscopic crystallinity and the microscopic packing within the crystals can be optimized from the initial disordered kinetically trapped states (i.e. quenched, as-spun). As the temperature further crosses over the transition points, the hole mobility showed a universal decrease in all samples, which has been described in 2.3.3 and ascribed to the microscopic expansion along the π-π stacking direction and the macroscopic loss of crystallinity.

4.4 Conclusions

In this chapter, by combining TOF hole mobility results and ^{13}C solid-state NMR results, the correlation between the hole transport properties and semi-crystalline morphology of rr-P3HT was elucidated. It is found that physical aging rr-P3HT, even at room temperature, has led to the growth of the short-range ordering in the amorphous phase, thereby establishing good bridging between the crystalline grains and facilitating hole transport in the amorphous regions. Consequently, significant increases of hole mobility at low temperatures were observed in all the rr-P3HT samples. Interestingly, an abrupt jump in hole mobility at high temperatures above 140°C was also found virtually for all the samples regardless of aging history. Corresponding NMR investigations revealed that, different from the aging effects that occur inside the amorphous phase, the structural origin of the high temperature jump in mobility is likely associated with a change in molecular packing within the crystalline phase, which can promote both intra-

and inter-molecular transport. It is expected that, both the short-range ordering in the amorphous phase and molecular stacking structures in the crystalline phase would be critical factors to consider in optimizing the processing of rr-P3HT in particular and, design of new class of high-performance semiconducting polymers in general.

4.5 References

1.   Sirringhaus, H.; Brown, P.; Friend, R. *Nature* **1999**, *401*, 685–688.

2.   Chen, D.; Nakahara, A.; Wei, D.; Nordlund, D.; Russell, T. P. *Nano Lett.* **2011**, *11*, 561–567.

3.   Luo, C.; Kyaw, A. K. K.; Perez, L. a; Patel, S.; Wang, M.; Grimm, B.; Bazan, G. C.; Kramer, E. J.; Heeger, A. J. *Nano Lett.* **2014**, *14*, 2764–2771.

4.   Kim, Y.; Cook, S.; Tuladhar, S. M.; Choulis, S. a.; Nelson, J.; Durrant, J. R.; Bradley, D. D. C.; Giles, M.; McCulloch, I.; Ha, C.-S.; Ree, M. *Nat. Mater.* **2006**, *5*, 197–203.

5.   Woo, C. H.; Thompson, B. C.; Kim, B. J.; Toney, M. F.; Fréchet, J. M. J. *J. Am. Chem. Soc.* **2008**, *130*, 16324–16329.

6.   Shen, X.; Duzhko, V. V.; Russell, T. P. *Adv. Energy Mater.* **2013**, *3*, 263–270.

7.   Zen, A.; Pflaum, J.; Hirschmann, S.; Zhuang, W.; Jaiser, F.; Asawapirom, U.; Rabe, J. P.; Scherf, U.; Neher, D. *Adv. Funct. Mater.* **2004**, *14*, 757–764.

8.   Kline, R.; McGehee, M.; Kadnikova, E. *Macromolecules* **2005**, *38*, 3312–3319.

9.   Snyder, C. R.; Henry, J. S.; DeLongchamp, D. M. *Macromolecules* **2011**, *44*, 7088–7091.

10.   Zen, A.; Saphiannikova, M.; Neher, D. *Macromolecules* **2006**, *39*, 2162–2171.

11.   Crossland, E. J. W.; Tremel, K.; Fischer, F.; Rahimi, K.; Reiter, G.; Steiner, U.; Ludwigs, S. *Adv. Mater.* **2012**, *24*, 839–844.

12.   Kline, R. J.; McGehee, M. D.; Toney, M. F. *Nat. Mater.* **2006**, *5*, 222–228.

13.   Devižis, a.; Meerholz, K.; Hertel, D.; Gulbinas, V. *Chem. Phys. Lett.* **2010**, *498*, 302–306.

14. Pascui, O. F.; Lohwasser, R.; Sommer, M.; Thelakkat, M.; Thurn-Albrecht, T.; Saalwächter, K. *Macromolecules* **2010**, *43*, 9401–9410.

15. Lan, Y.-K.; Huang, C.-I. *J. Phys. Chem. B* **2009**, *113*, 14555–14564.

16. Noriega, R.; Rivnay, J.; Vandewal, K.; Koch, F. P. V; Stingelin, N.; Smith, P.; Toney, M. F.; Salleo, A. *Nat. Mater.* **2013**, *12*, 1038–1044.

17. Bolognesi, A.; Porzio, W.; Provasoli, A.; Botta, C.; Comotti, A.; Sozzani, P.; Simonutti, R. *Macromol. Chem. Phys.* **2001**, *202*, 2586–2591.

18. Yazawa, K.; Inoue, Y.; Yamamoto, T.; Asakawa, N. *Phys. Rev. B* **2006**, *74*, 094204.

19. Snyder, C. R.; Nieuwendaal, R. C.; DeLongchamp, D. M.; Luscombe, C. K.; Sista, P.; Boyd, S. D. *Macromolecules* **2014**, *47*, 3942–3950.

20. Nieuwendaal, R.; Snyder, C. R.; DeLongchamp, D. M. *ACS Macro Lett.* **2014**, *3*, 130–135.

21. Koch, F. P. V.; Heeney, M.; Smith, P. *J. Am. Chem. Soc.* **2013**, *135*, 13699–13709.

22. Metz, G.; Ziliox, M.; Smith, S. O. *Solid State Nucl. Magn. Reson.* **1996**, *7*, 155–160.

23. Ballantyne, A. M.; Chen, L.; Dane, J.; Hammant, T.; Braun, F. M.; Heeney, M.; Duffy, W.; McCulloch, I.; Bradley, D. D. C.; Nelson, J. *Adv. Funct. Mater.* **2008**, *18*, 2373–2380.

24. Koch, F. P. V.; Rivnay, J.; Foster, S.; Müller, C.; Downing, J. M.; Buchaca-Domingo, E.; Westacott, P.; Yu, L.; Yuan, M.; Baklar, M.; Fei, Z.; Luscombe, C.; McLachlan, M. a.; Heeney, M.; Rumbles, G.; Silva, C.; Salleo, A.; Nelson, J.; Smith, P.; Stingelin, N. *Prog. Polym. Sci.* **2013**, *38*, 1978–1989.

25. Brinkmann, M. *J. Polym. Sci. Part B Polym. Phys.* **2011**, *49*, 1218–1233.

26. Yuan, Y.; Zhang, J.; Sun, J.; Hu, J.; Zhang, T.; Duan, Y. *Macromolecules* **2011**, *44*, 9341–9350.

27. Wu, Z.; Petzold, A.; Henze, T.; Thurn-Albrecht, T.; Lohwasser, R. H.; Sommer, M.; Thelakkat, M. *Macromolecules* **2010**, *43*, 4646–4653.

28. Hutchinson, J. *Prog. Polym. Sci.* **1995**, *20*, 703–760.

29. Cangialosi, D.; Boucher, V. M.; Alegría, A.; Colmenero, J. *Soft Matter* **2013**, *9*, 8619-8630.

30.   Struik, L. C. E. *Physical Aging in Amorphous Glassy Polymers and Other Materials*; Elsevier Science: Amsterdam, The Netherlands, 1978.

31.   Dudenko, D.; Kiersnowski, A.; Shu, J.; Pisula, W.; Sebastiani, D.; Spiess, H. W.; Hansen, M. R. *Angew. Chem. Int. Ed.* **2012**, *51*, 11068–11072.

32.   Kim, J. Y.; Frisbie, C. D. *J. Phys. Chem. C* **2008**, *112*, 17726–17736.

33.   Staniec, P. a.; Parnell, A. J.; Dunbar, A. D. F.; Yi, H.; Pearson, A. J.; Wang, T.; Hopkinson, P. E.; Kinane, C.; Dalgliesh, R. M.; Donald, A. M.; Ryan, A. J.; Iraqi, A.; Jones, R. a. L.; Lidzey, D. G. *Adv. Energy Mater.* **2011**, *1*, 499–504.

34.   Kuila, B. K.; Nandi, A. K. *J. Phys. Chem. B* **2006**, *110*, 1621–1631.

35.   Dag, S.; Wang, L.-W. *J. Phys. Chem. B* **2010**, *114*, 5997–6000.

36.   VanderHart, D. L.; Snyder, C. R. *Macromolecules* **2003**, *36*, 4813–4826.

37.   Nelson, J.; Kwiatkowski, J. J.; Kirkpatrick, J.; Frost, J. M. *Acc. Chem. Res.* **2009**, *42*, 1768–1778.

38.   Brinkmann, M.; Rannou, P. *Macromolecules* **2009**, *42*, 1125–1130.

39.   Mandelkern, L. *Polym. J.* **1985**, *17*, 337–350.

40.   Kitamaru, R.; Horii, F.; Murayama, K. *Macromolecules* **1986**, *19*, 636–643.

41.   Müller, C.; Zhigadlo, N. D.; Kumar, A.; Baklar, M. a.; Karpinski, J.; Smith, P.; Kreouzis, T.; Stingelin, N. *Macromolecules* **2011**, *44*, 1221–1225.

42.   Pingel, P.; Zen, A.; Abellón, R. D.; Grozema, F. C.; Siebbeles, L. D. a.; Neher, D. *Adv. Funct. Mater.* **2010**, *20*, 2286–2295.

43.   Tashiro, K.; Ono, K.; Minagawa, Y.; Kobayashi, M.; Kawai, T.; Yoshino, K. *J. Polym. Sci. Part B Polym. Phys.* **1991**, *29*, 1223–1233.

44.   Prosa, T.; Winokur, M.; Moulton, J.; Smith, P.; Heeger, A. J. *Macromolecules* **1992**, *25*, 4364–4372.

CHAPTER 5

OUTLOOK AND FUTURE WORK

5.1 On the Microstructure–Hole Transport Correlations in Semi-Crystalline P3HT

Two temperature regions with distinct transport mechanisms have been identified in rr-P3HT, as shown in Chapter 2: at temperatures below 120°C, the hole transport exhibits thermal activation behavior and is limited by the trapping amorphous regions in between the crystalline grains; when the temperature exceeds 120°C, significant structural changes, namely an expansion along the π-π stacking direction and a deterioration of the degree of crystallinity, occur simultaneously at micro- and macroscopic scales, respectively, resulting in the decrease of hole mobility.[1] The demonstrated strategy combining both structural investigations and transport characterizations is suggested to be fundamentally indispensible to understanding the intrinsic correlation between semi-crystalline morphology-transport properties not only in rr-P3HT but also in other classes of conjugated polymers of semi-crystalline nature, which may have vastly different structural characters from those of P3HT. Not systematically investigated in detail in our study, however, is the effect of the built-in molecular characteristics of the rr-P3HT on the morphology and hole transport behavior. Molecular weight, PDI and regioregularity are undoubtedly the most important parameters inherent to each batch of rr-P3HT among countless other conjugated polymers. Despite the fact numerous manuscripts have been published to address the individual effect of molecular weights,[2–7] PDI[8] and regioregularity,[8,9] it is not uncommon that materials with similar molecular weights would behave differently in two separate studies from two research groups, due primarily to the inevitable variation in the PDI and

regioregularity, and vice versa. Not until recently has the synthetic efforts led to rr-P3HT with single or no region-defects and well-defined molecular weights as exemplified in Table 5.1,[8] allowing a thorough investigation of the respective role of regioregularity and PDI on the physical properties of rr-P3HT.

Table 5.1: Physical Properties of Well-Defined Regioregular P3HT with Similar Molecular Weights, Single or no Regiodefect and Comparable Narrow PDI.[8]

	1TT-P3HT-43	0TT-P3HT-45	0TT-P3HT-65	1TT-P3HT-76
reference to Supporting Information	2c	4i	4f	2e
TT defect	1	0	0	1
M_n (GPC) [kg/mol]	11.8	13.4	17.2	21.2
PDI (GPC)	1.13	1.11	1.26	1.28
$M_{n,MALDI}$ [kg/mol]	6.9	7.5	10.5	$-^b$
PDI (MALDI)	1.022	1.020	1.028	$-^b$
DP (MALDI)	41	45	63	$-^b$
DP (NMR)	43	45	65	76
d_{100} [nm] (190 °C)	1.82	1.81	1.82	1.83
$d_{002/020}$ [nm] (190 °C)	0.38	0.38	0.38	0.38

Therefore, as a next step, using rr-P3HT as a model for conjugated semiconducting polymers, it is highly desirable to apply the same approach as presented in Chapter 2 to a range of rr-P3HTs with well-defined molecular parameters, in an effort to unambiguously address the respective roles of the molecular weight, PDI and regioregularity on the semi-crystalline morphology at different temperatures and length scales, and its correlation with the intrinsic hole transport properties in the materials. The results from this comprehensive study are anticipated to further deepen the understanding of the otherwise elusive molecular parameter - semi-crystalline microstructure - hole transport properties relationships in rr-P3HT, for instance, by elucidating the driving force for the accumulation of stresses inside rr-P3HT crystals and pinpointing the

structural origin of the microscopic packing modification at high temperature discussed in Chapter 4.

5.2 Probing the Multi-Scale Ordering in Semi-Crystalline P3HT

It should be noted that thin films of semiconducting polymers widely used in optoelectronic devices such as OPV cells and OFET devices typically have thicknesses that are less than 200nm. Consequently, the molecular orientation and ordering of the semiconducting polymer in such a thin film geometry will be largely affected by the presence of the substrate and air interfaces,[10] the confinement effect,[11,12] the solvent evaporation processes,[13] resulting in a significant deviation from the melt-crystallized bulk samples used in our study. Due to the aforementioned factors, quantitatively determining the degree of crystallinity of rr-P3HT in a thin film turned out to be much more complex in comparison to the bulk characterizations (WAXD, density, NMR, etc.). It is suggested in a recent review by Rivnay et al. that by using grazing-incidence X-ray diffraction, the relative degree of crystallinity in thin polymer film can be evaluated by constructing a pole figure, which describes the orientation distribution of specifically chosen diffraction peaks as a function of all possibly existed crystal orientations.[12,14] However, the construction of the pole figure requires the access to synchrotron radiation sources where high resolution rock-curve can be acquired, and is limited by the complexity involved in the procedures. Alternatively, a relatively simple approach based on the linear absorption spectrum of rr-P3HT thin films has been proposed by Clark and co-workers, wherein the thin film aggregated structures can be related to absorption of rr-P3HT by using a model developed by Spano.[13,15–18] Specifically, the vibronic features usually appearing as shoulders at lower energies (longer wavelength) in the rr-P3HT

absorption spectrum are attributed to the absorption of planarized chains within the aggregates; while the absorption at higher energy (lower wavelength) arises from the chains in the disordered states, in reminiscent of the absorption of a dilute solution. This contrast, coupled with Spano's model in the limit of a weakly interacting H-aggregates consisting of parallel-aligned and co-facially stacked P3HT chains,[19] allows one to decompose the absorption spectrum into contributions from ordered aggregates and disordered chains, thus providing a quantitative measure of the fractional aggregated structures of the film. Figure 5.1(a) shows an exemplary fitting of the P3HT aggregation component from the P3HT:PCBM absorption spectrum by Turner et al, where the amorphous absorbance component is taken as the difference between the total measured absorbance and the fitted aggregation absorbance.[15] Subsequently, with the knowledge of the molar extinction coefficient ratio between aggregates and amorphous chains,[13] the degree of aggregates (or crystallinity) can be calculated and an example by Turner et al. is shown in Figure 5.1(b),[15] which was claimed to be consistent with the crystallinity obtained from electron tomography measurements.[20] Although little correlation was observed in line with GIXD measurements,[21] the degree of aggregates of the most ordered pristine P3HT film cast from dichlorobenzene (~53%) measured by linear absorption spectroscopy seems to be comparable to the degree of crystallinity of 34K sample determined by NMR in our study. Presumably, the degree of aggregates quantified by the linear absorption spectroscopy would include the short-range order phase in the rr-P3HT and, thus, would have some correlations with the NMR-determined crystallinity. Another figure of merit is that the absorption approach is suitable not only for the thin film samples but also for the solution samples with fibril-type aggregates.

Therefore, as a next step, it would be interesting to elucidate the structural correlation between the aggregated structures in the thin films/solutions determined by linear absorption spectroscopy and the degree of crystallinity determined by the other physical methods. The results are expected to (i) allow the development of facile and reliable methods to evaluating the degree of ordering in rr-P3HT and other photoactive polymers in thin film geometries that are more relevant to optoelectronic devices; and (ii) shed light on the rr-P3HT packing structures in self-assembled nanoscale architectures.
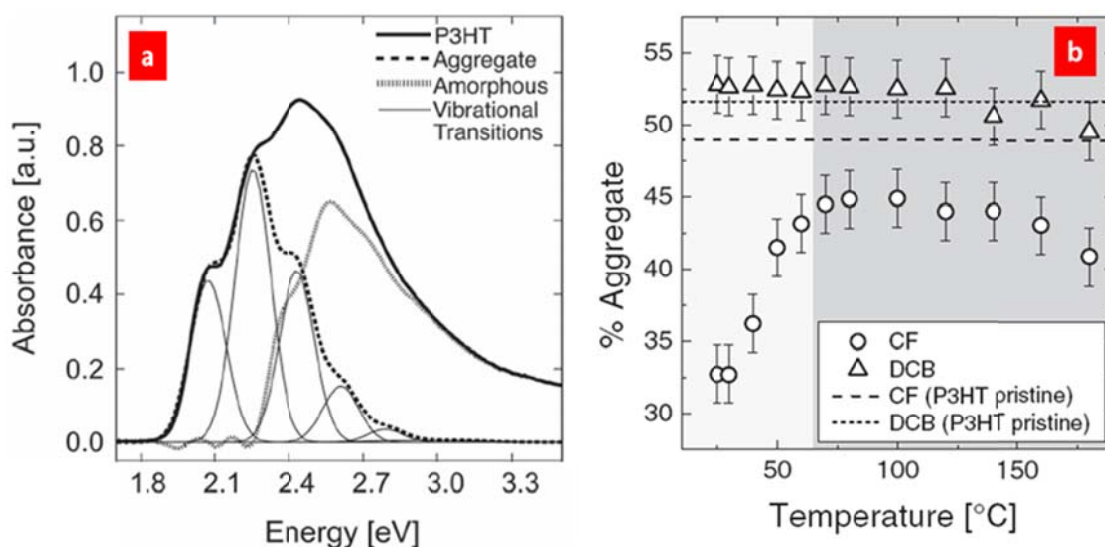
Figure 5.1: (a) An exemplary fitting of P3HT absorbance resulting in the aggregation component (dashed line) and amorphous component (dotted line). The individual vibrational transitions in the aggregate absorption are also shown; (b) Percentage of aggregates within the P3HT phase of P3HT:PCBM and pristine P3HT films cast from chloroform or dichlorobenzene and annealed at different temperatures.[15]

5.3 Revealing the Significant Effect of Subtle Structural Changes on the Hole Transport of P3HT Using Solid-state NMR

The aging effects on the hole mobility in rr-P3HT at low temperatures has concluded the increasingly important role of the local short-range order in the amorphous

phase plays in optimizing the semi-crystalline morphology for hole transport. Given the qualitative agreement observed in the transport behaviors of various semiconducting polymers from a comprehensive analysis by Noriega et al.,[22] it seems to strongly suggest that the presence of such short-range ordering is not uniquely seen in rr-P3HT but may also be present in other classes of semiconducting polymers, especially those found to be weakly ordered by scattering methods.[23] One of the possible driving factors leading to the locally short-range order is the rigidity and conformation of the backbone: as the rigidity of the backbone increases, the chains residing in the amorphous phase would remain relatively planar, thus promoting the inter-molecular packing via π-π interactions; or alternatively, the increasing rigidity may lead to more efficient intra-molecular transport at short length scales as predicted by Noriega et al.[24] The pivotal roles of the short-range order in semiconducting polymers necessitates an extension of current quantitative study of rr-P3HT to other high-mobility conjugated semiconducting polymers. Among the high-performance semiconducting polymers, the class of diketopyrrolopyrrole (DPP) based polymers as shown in Figure 5.2 could be a good candidate to initiate the investigation owing to the good indication of ordering from scattering, UV-Vis absorption and DSC measurements.[25] Thus, as a next step, a combination of WAXD, density, solid-state NMR, DSC and linear absorption spectroscopy measurements can be applied to systematically and quantitatively investigate and compare the semi-crystalline ordering in the DPP based polymers. The results are expected to further uncover the structural origin of the high mobility exhibited by DPP-based conjugated polymers.
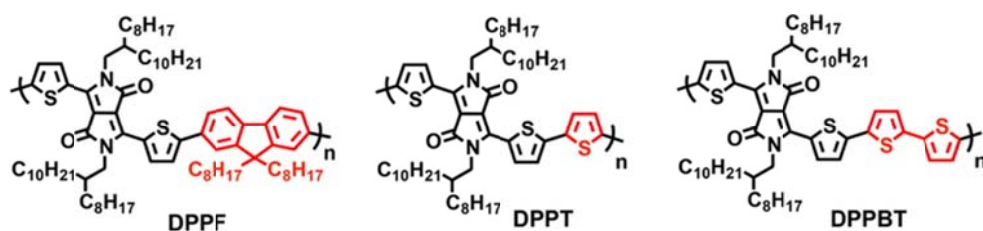
Figure 5.2: The chemical structures of three semi-crystalline diketopyrrolopyrrole-based conjugated polymers: poly(diketopyrrolopyrrole-thiophene-fluorene-thiophene) (DPPF), poly(diketopyrrolopyrrole-terthiophene) (DPPT), and poly(diketopyrrolopyrrole-quaterthiophene) (DPPBT).[25]

As demonstrated in Chapter 4, ^{13}C solid-state NMR has revealed an interesting modification of the molecular packing inside the rr-P3HT crystals, which has led to an abrupt jump in the hole mobility measured by TOF. However, a quantitative packing model highlighting the modification processes is still missing and would be essentially important to be considered if a better molecular packing is aimed at when designing new conjugated polymers. To that end, it is suggested by Dudenko and co-workers that quantum-chemical calculations of chemical shifts in solid-state NMR with the assistance of nucleus-independent chemical shift (NICS) maps would be particularly useful.[26,27] By using diffraction method to evaluate long-range order and high resolution ^{1}H and ^{13}C solid-state NMR methods to assess molecular constraints, Dudenko et al. has proposed a strategy for determining the crystalline structures of bulk rr-P3HT and calculating the suitable packing models, which are shown in Figure 5.3.[26] Both unit-cell parameters derived from diffraction and molecular constraints deduced from NMR are considered in the resulting calculated models, therefore providing a comprehensive insight into the quantitative packing structures in P3HT. As a next step, it would be worthwhile to follow the procedures developed by Dudenko and co-workers and further quantify the shift in the molecular packing during stress relaxation at high temperature. Furthermore, pin-

pointing the narrow temperature window (between 160°C and 200°C) at which the stress relaxation processes occur for rr-P3HT of different molecular weights will also be interesting.
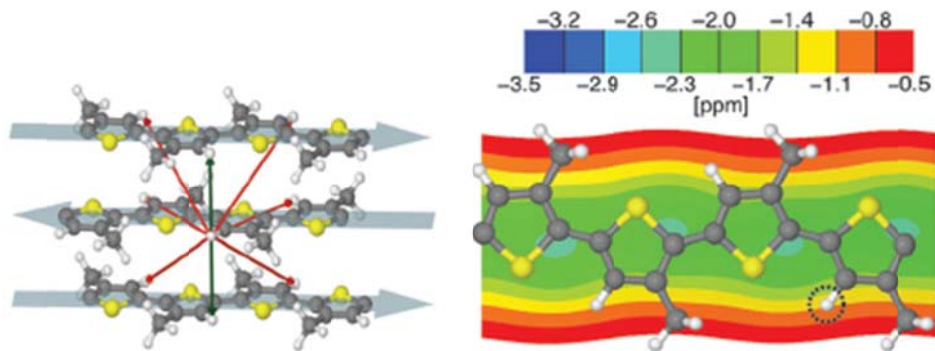
Figure 5.3: Packing model for P3HT considered in Ref 26 and the corresponding NICS maps. The NICS color bar quantifies the NMR chemical shift offset of the nuclei in a polymer chain induced by the electronic ring currents of all neighboring chains. Red and green arrows illustrate ^{1}H-^{1}H distances above and below 4 Å, respectively.[26]

5.4 References

1. Shen, X.; Duzhko, V. V.; Russell, T. P. *Adv. Energy Mater.* **2013**, *3*, 263–270.

2. Zen, A.; Saphiannikova, M.; Neher, D. *Macromolecules* **2006**, *39*, 2162–2171.

3. Zen, A.; Pflaum, J.; Hirschmann, S.; Zhuang, W.; Jaiser, F.; Asawapirom, U.; Rabe, J. P.; Scherf, U.; Neher, D. *Adv. Funct. Mater.* **2004**, *14*, 757–764.

4. Koch, F. P. V.; Rivnay, J.; Foster, S.; Müller, C.; Downing, J. M.; Buchaca-Domingo, E.; Westacott, P.; Yu, L.; Yuan, M.; Baklar, M.; Fei, Z.; Luscombe, C.; McLachlan, M. a.; Heeney, M.; Rumbles, G.; Silva, C.; Salleo, A.; Nelson, J.; Smith, P.; Stingelin, N. *Prog. Polym. Sci.* **2013**, *38*, 1978–1989.

5. Kline, R. J.; McGehee, M. D.; Kadnikova, E. N.; Liu, J.; Fréchet, J. M. J. *Adv. Mater.* **2003**, *15*, 1519–1522.

6. Kline, R.; McGehee, M.; Kadnikova, E. *Macromolecules* **2005**, *38*, 3312–3319.

7. Brinkmann, M.; Rannou, P. *Macromolecules* **2009**, *42*, 1125–1130.

8. Kohn, P.; Huettner, S.; Komber, H.; Senkovskyy, V.; Tkachov, R.; Kiriy, A.; Friend, R. H.; Steiner, U.; Huck, W. T. S.; Sommer, J.-U.; Sommer, M. *J. Am. Chem. Soc.* **2012**, *134*, 4790–4805.

9. Snyder, C. R.; Henry, J. S.; DeLongchamp, D. M. *Macromolecules* **2011**, *44*, 7088–7091.

10. Joseph Kline, R.; McGehee, M. D.; Toney, M. F. *Nat. Mater.* **2006**, *5*, 222–228.

11. Joshi, S.; Grigorian, S.; Pietsch, U.; Pingel, P.; Zen, A.; Neher, D.; Scherf, U. *Macromolecules* **2008**, *41*, 6800–6808.

12. Jimison, L. H.; Himmelberger, S.; Duong, D. T.; Rivnay, J.; Toney, M. F.; Salleo, A. *J. Polym. Sci. Part B Polym. Phys.* **2013**, *51*, 611–620.

13. Clark, J.; Chang, J.-F.; Spano, F. C.; Friend, R. H.; Silva, C. *Appl. Phys. Lett.* **2009**, *94*, 163306.

14. Rivnay, J.; Mannsfeld, S. C. B.; Miller, C. E.; Salleo, A.; Toney, M. F. *Chem. Rev.* **2012**, *112*, 5488–5519.

15. Turner, S. T.; Pingel, P.; Steyrleuthner, R.; Crossland, E. J. W.; Ludwigs, S.; Neher, D. *Adv. Funct. Mater.* **2011**, *21*, 4640–4652.

16. Spano, F. C. *J. Chem. Phys.* **2005**, *122*, 234701.

17. Spano, F. C. *Chem. Phys.* **2006**, *325*, 22–35.

18. Pingel, P.; Zen, A.; Abellón, R. D.; Grozema, F. C.; Siebbeles, L. D. a.; Neher, D. *Adv. Funct. Mater.* **2010**, *20*, 2286–2295.

19. Clark, J.; Silva, C.; Friend, R.; Spano, F. *Phys. Rev. Lett.* **2007**, *98*, 206406.

20. Van Bavel, S.; Sourty, E.; de With, G.; Frolic, K.; Loos, J. *Macromolecules* **2009**, *42*, 7396–7403.

21. Shin, N.; Richter, L. J.; Herzing, A. a.; Kline, R. J.; DeLongchamp, D. M. *Adv. Energy Mater.* **2013**, *3*, 938–948.

22. Noriega, R.; Rivnay, J.; Vandewal, K.; Koch, F. P. V; Stingelin, N.; Smith, P.; Toney, M. F.; Salleo, A. *Nat. Mater.* **2013**, *12*, 1038–1044.

23. Zhang, X.; Bronstein, H.; Kronemeijer, A. J.; Smith, J.; Kim, Y.; Kline, R. J.; Richter, L. J.; Anthopoulos, T. D.; Sirringhaus, H.; Song, K.; Heeney, M.; Zhang, W.; McCulloch, I.; DeLongchamp, D. M. *Nat. Commun.* **2013**, *4*, 2238-2246.

24.   Noriega, R.; Salleo, A.; Spakowitz, A. J. *Proc. Natl. Acad. Sci.* **2013**, *110,* 16315–16320.

25.   Liu, F.; Wang, C.; Baral, J. K.; Zhang, L.; Watkins, J. J.; Briseno, A. L.; Russell, T. P. *J. Am. Chem. Soc.* **2013**, *135*, 19248–19259.

26.   Dudenko, D.; Kiersnowski, A.; Shu, J.; Pisula, W.; Sebastiani, D.; Spiess, H. W.; Hansen, M. R. *Angew. Chem. Int. Ed.* **2012**, *51*, 11068–11072.

27.   Schleyer, P.; Maerker, C. *J. Am. Chem. Soc.* **1996**, *7863*, 6317–6318.

BIBLIOGRAPHY

Agostinelli, T.; Lilliu, S.; Labram, J. G.; Campoy-Quiles, M.; Hampton, M.; Pires, E.; Rawle, J.; Bikondoa, O.; Bradley, D. D. C.; Anthopoulos, T. D.; Nelson, J.; Macdonald, J. E. *Adv. Funct. Mater.* **2011**, *21*, 1701–1708.

Alexander, L. E. *X-ray Diffraction Methods in Polymer Science*; New York, Wiley-Interscience, 1969.

Aryal, M.; Trivedi, K.; Hu, W. W. *ACS Nano* **2009**, *3*, 3085–3090.

Balko, J.; Lohwasser, R. H.; Sommer, M.; Thelakkat, M.; Thurn-Albrecht, T. *Macromolecules* **2013**, *46*, 9642–9651.

Ballantyne, A. M.; Chen, L.; Dane, J.; Hammant, T.; Braun, F. M.; Heeney, M.; Duffy, W.; McCulloch, I.; Bradley, D. D. C.; Nelson, J. *Adv. Funct. Mater.* **2008**, *18*, 2373–2380.

Bassler, H. *Phys. Status Solidi* **1993**, *175*, 15–56.

Bolognesi, A.; Porzio, W.; Provasoli, A.; Botta, C.; Comotti, A.; Sozzani, P.; Simonutti, R. *Macromol. Chem. Phys.* **2001**, *202*, 2586–2591.

Brabec, C. J.; Cravino, A.; Meissner, D.; Sariciftci, N. S.; Fromherz, T.; Rispens, M. T.; Sanchez, L.; Hummelen, J. C. *Adv. Funct. Mater.* **2001**, *11*, 374–380.

Brinkmann, M.; Rannou, P. *Adv. Funct. Mater.* **2007**, *17*, 101–108.

Brinkmann, M. *J. Polym. Sci. Part B Polym. Phys.* **2011**, *49*, 1218–1233.

Brinkmann, M.; Rannou, P. *Macromolecules* **2009**, *42*, 1125–1130.

Cangialosi, D.; Boucher, V. M.; Alegría, A.; Colmenero, J. *Soft Matter* **2013**, *9*, 8619–8630.

Chen, D.; Liu, F.; Wang, C.; Nakahara, A.; Russell, T. *Nano Lett.* **2011**, *11*, 2071–2078.

Chen, D.; Nakahara, A.; Wei, D.; Nordlund, D.; Russell, T. P. *Nano Lett.* **2011**, *11*, 561–567.

Chen, T.; Wu, X.; Rieke, R. *J. Am. Chem. Soc.* **1995**, 233–244.

Clark, J.; Chang, J.-F.; Spano, F. C.; Friend, R. H.; Silva, C. *Appl. Phys. Lett.* **2009**, *94*, 163306.

Clark, J.; Silva, C.; Friend, R.; Spano, F. *Phys. Rev. Lett.* **2007**, *98*, 206406.

Colle, R.; Grosso, G.; Ronzani, A.; Zicovich-Wilson, C. M. *Phys. status solidi* **2011**, *248*, 1360–1368.

Collins, B.; Tumbleston, J.; Ade, H. *J. Phys. Chem. Lett.* **2011**, *2*, 3135–3145.

Crossland, E. J. W.; Tremel, K.; Fischer, F.; Rahimi, K.; Reiter, G.; Steiner, U.; Ludwigs, S. *Adv. Mater.* **2012**, *24*, 839–844.

Dag, S.; Wang, L.-W. *J. Phys. Chem. B* **2010**, *114*, 5997–6000.

Dang, M. T.; Hirsch, L.; Wantz, G. *Adv. Mater.* **2011**, *23*, 3597–3602.

DeLongchamp, D. M.; Kline, R. J.; Herzing, A. *Energy Environ. Sci.* **2012**, *5*, 5980–5993.

DeLongchamp, D. M.; Kline, R. J.; Fischer, D. a; Richter, L. J.; Toney, M. F. *Adv. Mater.* **2011**, *23*, 319–337.

Dennler, G.; Scharber, M. C.; Brabec, C. J. *Adv. Mater.* **2009**, *21*, 1323–1338.

Devižis, A.; Meerholz, K.; Hertel, D.; Gulbinas, V. *Chem. Phys. Lett.* **2010**, *498*, 302–306.

Dinelli, F.; Murgia, M.; Levy, P.; Cavallini, M.; Biscarini, F.; de Leeuw, D. *Phys. Rev. Lett.* **2004**, *92*, 116802.

Dudenko, D.; Kiersnowski, A.; Shu, J.; Pisula, W.; Sebastiani, D.; Spiess, H. W.; Hansen, M. R. *Angew. Chem. Int. Ed.* **2012**, *51*, 11068–11072.

Duzhko, V.; Semyonov, A.; Twieg, R.; Singer, K. *Phys. Rev. B* **2006**, *73*, 064201.

Flory, P. J. *Statistical Mechanics of Chain Molecules*; Interscience Publishers: New York, 1969.

Goppel, J. M.; Arlman, J. *J. Appl. Sci. Res.* **1949**, *A1*, 462–474.

Hu, W.; Sirota, E. B. *Macromolecules* **2003**, *36*, 5144–5149.

Hubbell, J.; Veigele, W.; Briggs, E. A.; Brown, R. T.; Cromer, D. T.; Howerton, R. J. *J. Phys. Chem. Ref. Data* **1975**, *4*, 471–538.

Hutchinson, J. *Prog. Polym. Sci.* **1995**, *20*, 703–760.

Jiang, X. M.; Österbacka, R.; Korovyanko, O.; An, C. P.; Horovitz, B.; Janssen, R. A. J.; Vardeny, Z. V. *Adv. Funct. Mater.* **2002**, *12*, 587–597.

Jimison, L. H.; Himmelberger, S.; Duong, D. T.; Rivnay, J.; Toney, M. F.; Salleo, A. *J. Polym. Sci. Part B Polym. Phys.* **2013**, *51*, 611–620.

Jimison, L. H.; Toney, M. F.; McCulloch, I.; Heeney, M.; Salleo, A. *Adv. Mater.* **2009**, *21*, 1568–1572.

Joshi, S.; Grigorian, S.; Pietsch, U.; Pingel, P.; Zen, A.; Neher, D.; Scherf, U. *Macromolecules* **2008**, *41*, 6800–6808.

Joshi, S.; Pingel, P.; Grigorian, S.; Panzner, T.; Pietsch, U.; Neher, D.; Forster, M.; Scherf, U. *Macromolecules* **2009**, *42*, 4651–4660.

Kayunkid, N.; Uttiya, S.; Brinkmann, M. *Macromolecules* **2010**, *43*, 4961–4967.

Kim, J. Y.; Frisbie, C. D. *J. Phys. Chem. C* **2008**, *112*, 17726–17736.

Kim, Y.; Cook, S.; Tuladhar, S. M.; Choulis, S. a.; Nelson, J.; Durrant, J. R.; Bradley, D. D. C.; Giles, M.; McCulloch, I.; Ha, C.-S.; Ree, M. *Nat. Mater.* **2006**, *5*, 197–203.

Kitamaru, R.; Horii, F.; Murayama, K. *Macromolecules* **1986**, *19*, 636–643.

Kline, R. J.; DeLongchamp, D. M.; Fischer, D. A.; Lin, E. K.; Richter, L. J.; Chabinyc, M. L.; Toney, M. F.; Heeney, M.; McCulloch, I. *Macromolecules* **2007**, *40*, 7960–7965.

Kline, R. J.; McGehee, M. D.; Toney, M. F. *Nat. Mater.* **2006**, *5*, 222–228.

Kline, R. J.; McGehee, M. D.; Kadnikova, E. N.; Liu, J.; Fréchet, J. M. J. *Adv. Mater.* **2003**, *15*, 1519–1522.

Kline, R.; McGehee, M.; Kadnikova, E. *Macromolecules* **2005**, *38*, 3312–3319.

Koch, F. P. V.; Heeney, M.; Smith, P. *J. Am. Chem. Soc.* **2013**, *135*, 13699–13709.

Koch, F. P. V.; Rivnay, J.; Foster, S.; Müller, C.; Downing, J. M.; Buchaca-Domingo, E.; Westacott, P.; Yu, L.; Yuan, M.; Baklar, M.; Fei, Z.; Luscombe, C.; McLachlan, M. a.; Heeney, M.; Rumbles, G.; Silva, C.; Salleo, A.; Nelson, J.; Smith, P.; Stingelin, N. *Prog. Polym. Sci.* **2013**, *38*, 1978–1989.

Kohn, P.; Huettner, S.; Komber, H.; Senkovskyy, V.; Tkachov, R.; Kiriy, A.; Friend, R. H.; Steiner, U.; Huck, W. T. S.; Sommer, J.-U.; Sommer, M. *J. Am. Chem. Soc.* **2012**, *134*, 4790–4805.

Kuila, B. K.; Nandi, A. K. *J. Phys. Chem. B* **2006**, *110*, 1621–1631.

Lan, Y.-K.; Huang, C.-I. *J. Phys. Chem. B* **2009**, *113*, 14555–14564.

Lazzeretti, P. *Prog. Nucl. Magn. Reson. Spectrosc.* **2000**, *36*, 1–88.

Lee, C. S.; Dadmun, M. D. *Polymer* **2014**, *55*, 4–7.

Lilliu, S.; Agostinelli, T.; Pires, E.; Hampton, M.; Nelson, J.; Macdonald, J. E. *Macromolecules* **2011**, *44*, 2725–2734.

Litvinov, V. M.; Kurelec, L. *Polymer* **2014**, *55*, 620–625.

Liu, F.; Gu, Y.; Jung, J. W.; Jo, W. H.; Russell, T. P. *J. Polym. Sci. Part B Polym. Phys.* **2012**, *50*, 1018–1044.

Liu, F.; Gu, Y.; Shen, X.; Ferdous, S.; Wang, H.-W.; Russell, T. P. *Prog. Polym. Sci.* **2013**, *38*, 1990–2052.

Liu, F.; Wang, C.; Baral, J. K.; Zhang, L.; Watkins, J. J.; Briseno, A. L.; Russell, T. P. *J. Am. Chem. Soc.* **2013**, *135*, 19248–19259.

Loewe, R. S.; Khersonsky, S. M.; McCullough, R. D. *Adv. Mater.* **1999**, *11*, 250–253.

Luo, C.; Kyaw, A. K. K.; Perez, L. a; Patel, S.; Wang, M.; Grimm, B.; Bazan, G. C.; Kramer, E. J.; Heeger, A. J. *Nano Lett.* **2014**, *14*, 2764–2771.

Mandelkern, L. *Polym. J.* **1985**, *17*, 337–350.

Mauer, R.; Kastler, M.; Laquai, F. *Adv. Funct. Mater.* **2010**, *20*, 2085–2092.

McMahon, D. P.; Cheung, D. L.; Goris, L.; Dacuña, J.; Salleo, A.; Troisi, A. *J. Phys. Chem. C* **2011**, *115*, 19386–19393.

Metz, G.; Ziliox, M.; Smith, S. O. *Solid State Nucl. Magn. Reson.* **1996**, *7*, 155–160.

Mo, Z.; Lee, K. B.; Moon, Y. B.; Kobayashi, M.; Heeger, A. J.; Wudl, F. *Macromolecules* **1985**, *18*, 1972–1977.

Mowery, D. M.; Harris, D. J.; Schmidt-Rohr, K. *Macromolecules* **2006**, *39*, 2856–2865.

Mozer, A. J.; Sariciftci, N. S. *Chem. Phys. Lett.* **2004**, *389*, 438–442.

Mozer, A.; Sariciftci, N.; Pivrikas, A.; Österbacka, R.; Juška, G.; Brassat, L.; Bässler, H. *Phys. Rev. B* **2005**, *71*, 035214.

Müller, C.; Zhigadlo, N. D.; Kumar, A.; Baklar, M. a; Karpinski, J.; Smith, P.; Kreouzis, T.; Stingelin, N. *Macromolecules* **2011**, *44*, 1221–1225.

Nelson, J.; Kwiatkowski, J. J.; Kirkpatrick, J.; Frost, J. M. *Acc. Chem. Res.* **2009**, *42*, 1768–1778.

Nieuwendaal, R.; Snyder, C. R.; DeLongchamp, D. M. *ACS Macro Lett.* **2014**, *3*, 130–135.

Noriega, R.; Rivnay, J.; Vandewal, K.; Koch, F. P. V; Stingelin, N.; Smith, P.; Toney, M. F.; Salleo, A. *Nat. Mater.* **2013**, *12*, 1038–1044.

Noriega, R.; Salleo, A.; Spakowitz, A. J. *Proc. Natl. Acad. Sci. U. S. A.* **2013**, *110*, 16315–16320.

O'Connor, B.; Kline, R. J.; Conrad, B. R.; Richter, L. J.; Gundlach, D.; Toney, M. F.; DeLongchamp, D. M. *Adv. Funct. Mater.* **2011**, *21*, 3697–3705.

Pascui, O. F.; Lohwasser, R.; Sommer, M.; Thelakkat, M.; Thurn-Albrecht, T.; Saalwächter, K. *Macromolecules* **2010**, *43*, 9401–9410.

Peet, J.; Kim, J. Y.; Coates, N. E.; Ma, W. L.; Moses, D.; Heeger, A. J.; Bazan, G. C. *Nat. Mater.* **2007**, *6*, 497–500.

Pingel, P.; Zen, A.; Abellón, R. D.; Grozema, F. C.; Siebbeles, L. D. A.; Neher, D. *Adv. Funct. Mater.* **2010**, *20*, 2286–2295.

Prosa, T.; Winokur, M.; Moulton, J.; Smith, P.; Heeger, A. J. *Macromolecules* **1992**, *25*, 4364–4372.

Rivnay, J.; Mannsfeld, S. C. B.; Miller, C. E.; Salleo, A.; Toney, M. F. *Chem. Rev.* **2012**, *112*, 5488–5519.

Ro, H. W.; Akgun, B.; O'Connor, B. T.; Hammond, M.; Kline, R. J.; Snyder, C. R.; Satija, S. K.; Ayzner, A. L.; Toney, M. F.; Soles, C. L.; DeLongchamp, D. M. *Macromolecules* **2012**, *45*, 6587–6599.

Ruland, W. *Acta Crystallogr.* **1961**, *14*, 1180–1185.

Salleo, A.; Kline, R. J.; DeLongchamp, D. M.; Chabinyc, M. L. *Adv. Mater.* **2010**, *22*, 3812–3838.

Schleyer, P.; Maerker, C. *J. Am. Chem. Soc.* **1996**, *7863*, 6317–6318.

Shen, X.; Duzhko, V. V.; Russell, T. P. *Adv. Energy Mater.* **2013**, *3*, 263–270.

Shin, N.; Richter, L. J.; Herzing, A. A.; Kline, R. J.; DeLongchamp, D. M. *Adv. Energy Mater.* **2013**, *3*, 938–948.

Shrotriya, V. *Nat. Photonics* **2009**, *3*, 447–449.

Sirringhaus, H.; Tessler, N.; Friend, R. H. *Science* **1998**, *280*, 1741–1744.

Sirringhaus, H.; Brown, P.; Friend, R. *Nature* **1999**, *401*, 685–688.

Snyder, C. R.; Henry, J. S.; DeLongchamp, D. M. *Macromolecules* **2011**, *44*, 7088–7091.

Snyder, C. R.; Nieuwendaal, R. C.; DeLongchamp, D. M.; Luscombe, C. K.; Sista, P.; Boyd, S. D. *Macromolecules* **2014**, *47*, 3942–3950.

Spano, F. C. *J. Chem. Phys.* **2005**, *122*, 234701.

Spano, F. C. *Chem. Phys.* **2006**, *325*, 22–35.

Stehling, F.; Mandelkern, L. *Macromolecules* **1970**, *1*, 242–252.

Street, R. A. *Science* **2013**, *341*, 1072–1073.

Struik, L. C. E. *Physical Aging in Amorphous Glassy Polymers and Other Materials*; Elsevier Science: Amsterdam, The Netherlands, 1978.

Swan, P. *J. Polym. Sci.* **1962**, *56*, 403–407.

Tashiro, K.; Ono, K.; Minagawa, Y.; Kobayashi, M.; Kawai, T.; Yoshino, K. *J. Polym. Sci. Part B Polym. Phys.* **1991**, *29*, 1223–1233.

Thompson, B. C.; Fréchet, J. M. J. *Angew. Chem. Int. Ed.* **2008**, *47*, 58–77.

Tsao, H. N.; Cho, D. M.; Park, I.; Hansen, M. R.; Mavrinskiy, A.; Yoon, D. Y.; Graf, R.; Pisula, W.; Spiess, H. W.; Müllen, K. *J. Am. Chem. Soc.* **2011**, *133*, 2605–2612.

Turner, S. T.; Pingel, P.; Steyrleuthner, R.; Crossland, E. J. W.; Ludwigs, S.; Neher, D. *Adv. Funct. Mater.* **2011**, *21*, 4640–4652.

Vakhshouri, K.; Kozub, D. R.; Wang, C.; Salleo, A.; Gomez, E. D. *Phys. Rev. Lett.* **2012**, *108*, 026601.

Van Bavel, S.; Sourty, E.; de With, G.; Frolic, K.; Loos, J. *Macromolecules* **2009**, *42*, 7396–7403.

Van Rossum, B. J.; Steensgaard, D. B.; Mulder, F. M.; Boender, G. J.; Schaffner, K.; Holzwarth, a R.; DeGroot, H. J. *Biochemistry* **2001**, *40*, 1587–1595.

van-Bavel, S.; Sourty, E.; Loos, J. *Nano Lett.* **2009**, *9*, 507–513.

VanderHart, D. L.; Snyder, C. R. *Macromolecules* **2003**, *36*, 4813–4826.

Verploegen, E.; Mondal, R.; Bettinger, C. J.; Sok, S.; Toney, M. F.; Bao, Z. *Adv. Funct. Mater.* **2010**, *20*, 3519–3529.

Wang, T.; Dunbar, A. D. F.; Staniec, P. A.; Pearson, A. J.; Hopkinson, P. E.; MacDonald, J. E.; Lilliu, S.; Pizzey, C.; Terrill, N. J.; Donald, A. M.; Ryan, A. J.; Jones, R. A. L.; Lidzey, D. G. *Soft Matter* **2010**, *6*, 4128.

Weidinger, A.; Hermans, P. *Makromol. Chemie* **1961**, *50*, 98–115.

Woo, C. H.; Thompson, B. C.; Kim, B. J.; Toney, M. F.; Fréchet, J. M. J. *J. Am. Chem. Soc.* **2008**, *130*, 16324–16329.

Wu, Z.; Petzold, A.; Henze, T.; Thurn-Albrecht, T.; Lohwasser, R. H.; Sommer, M.; Thelakkat, M. *Macromolecules* **2010**, *43*, 4646–4653.

Yang, H.; LeFevre, S. W.; Ryu, C. Y.; Bao, Z. *Appl. Phys. Lett.* **2007**, *90*, 172116.

Yazawa, K.; Inoue, Y.; Yamamoto, T.; Asakawa, N. *Phys. Rev. B* **2006**, *74*, 094204.

You, J.; Dou, L.; Yoshimura, K.; Kato, T.; Ohya, K.; Moriarty, T.; Emery, K.; Chen, C.-C.; Gao, J.; Li, G.; Yang, Y. *Nat. Commun.* **2013**, *4*, 1446.

Yuan, Y.; Zhang, J.; Sun, J.; Hu, J.; Zhang, T.; Duan, Y. *Macromolecules* **2011**, *44*, 9341–9350.

Zen, A.; Pflaum, J.; Hirschmann, S.; Zhuang, W.; Jaiser, F.; Asawapirom, U.; Rabe, J. P.; Scherf, U.; Neher, D. *Adv. Funct. Mater.* **2004**, *14*, 757–764.

Zen, A.; Saphiannikova, M.; Neher, D. *Macromolecules* **2006**, *39*, 2162–2171.

Zhang, F.; Ilavsky, J.; Long, G. G.; Quintana, J. P. G.; Allen, A. J.; Jemian, P. R. *Metall. Mater. Trans. A* **2009**, *41*, 1151–1158.

Zhang, X.; Bronstein, H.; Kronemeijer, A. J.; Smith, J.; Kim, Y.; Kline, R. J.; Richter, L. J.; Anthopoulos, T. D.; Sirringhaus, H.; Song, K.; Heeney, M.; Zhang, W.; McCulloch, I.; DeLongchamp, D. M. *Nat. Commun.* **2013**, *4*, 2238–2246.

Zhokhavets, U.; Erb, T.; Gobsch, G.; Al-Ibrahim, M.; Ambacher, O. *Chem. Phys. Lett.* **2006**, *418*, 347–350.

http://henke.lbl.gov/optical_constants http://henke.lbl.gov/optical_constants.